UNIVERSITY OF CALIFORNIA, SAN DIEGO

Near-Field Microscopy in Liquid for Accurate High-Resolution Optical Characterization

A dissertation submitted in partial satisfaction of the
requirements for the degree
Doctor of Philosophy

in

Electrical Engineering (Photonics)

by

Maurice R. Ayache

Committee in charge:

Professor Yeshaiahu Fainman, Chair
Professor Leonid Butov
Professor Zhaowei Liu
Professor Vitaliy Lomakin
Professor Geert Schmid-Schönbein

2012

The dissertation of Maurice R. Ayache is approved, and it is acceptable in quality and form for publication on microfilm and electronically:

_____

_____

_____

_____

_____

Chair

University of California, San Diego

2012

TABLE OF CONTENTS

LIST OF FIGURES

LIST OF ABBREVIATIONS

AFM Atomic Force Microscopy

BOE Buffered Oxide Etch

ESR electrosatic repulsion

H-NSOM Heterodyne Near-Field Scanning Optical Microscope

HSQ hydrogen silesquioxane

LRSP Long Range Surface Plasmon

NSOM Near-Field Scanning Optical Microscope/Microscopy

PECVD Plasma-Enhanced Chemical Vapor Deposition

PID proportional-integral-derivative

PSD position-sensitive detector

PSTM Photon Scanning Tunneling Microscopy

SNR Signal-to-Noise Ratio

SPM Scanning Probe Microscopy

SPP surface plasmon polariton

STM Scanning Tunneling Microscopy

ACKNOWLEDGEMENTS

A PhD is a lengthy and sometimes arduous journey that, without exception, requires the help of many others. Many people have accompanied me on this journey, showing me the way towards the finish and lifting me up when I fell

I would first like to acknowledge my advisor, Professor Shaya Fainman, for his many years of support and guidance. The resources he provided me allowed me to do the experiments presented in this work, and his ideas gave me new directions in which to take my research.

I thank my committee, Professors Zhaowei Liu, Vitaly Lomakin, Geert Schmid-Schönbein, and Leonid Butov, for their time and their generous sharing of their expertise.

I am greatly indebted to my numerous co-authors and collaborators, who performed much of the work detailed here that allowed this research to be carried out. In addition to those I worked with formally, I would be remiss not to thank my colleagues in the Ultrafast and Nanoscale Optics group here at UCSD. Anybody who has been through graduate school knows how much of the real learning takes place in discussions with fellow students and postdocs, and my experience has been no exception.

Furthermore, I would like to thank the friends I have made here in San Diego, and from previous chapters of my life. I could not have made it without them.

My wonderful girlfriend Gina has been a constant source of support and companionship the last few years. Sharing my frustrations and celebrating my victories, she has brightened every day we have been together.

Finally, I thank my family: my brother Gabriel, who despite being younger always has a thing or two to teach me about life; my father, who inculcated in me a love of science and a passion for finding things out; and my mother, who has always taught me to only accept the best from myself. I thank them for raising me to be the man I am today.

The text of Chapter 3, in part or in full, is a reprint of the material as it appears in the following journal publication:

Liang Feng, Maurice Ayache, Jingqing Huang, Ye-Long Xu, Ming-Hui Lu, Yan-Feng Chen, Yeshaiahu Fainman, and Axel Scherer. Nonreciprocal light propagation in a silicon photonic circuit. *Science (New York, N.Y.)*, 333(6043):729–33, August 2011

The dissertation author was a primary co-investigator and co-author of this paper. The other authors assisted and supervised the research.

The text of Chapter 4, in part or in full, is a reprint of the material as it appears in the following journal publication:
Maurice Ayache, Maziar P. Nezhad, Steve Zamek, Maxim Abashin, and Yeshaiahu Fainman. Near-field measurement of amplitude and phase in silicon waveguides with liquid cladding. *Optics Letters*, 36(10):1869, May 2011

The dissertation author was the primary investigator and author of this paper. The other authors assisted and supervised the research.

VITA

2005	B. S. in Engineering Physics, Cornell University
2006	M. S. in Photonics, Boston University
2012	Ph. D. in Electrical Engineering (Photonics), University of California, San Diego

PUBLICATIONS

Maurice Ayache, Maziar P. Nezhad, Steve Zamek, Maxim Abashin, and Yeshaiahu Fainman. Near-field measurement of amplitude and phase in silicon waveguides with liquid cladding. *Optics Letters*, 36(10):1869, May 2011

Liang Feng, Maurice Ayache, Jingqing Huang, Ye-Long Xu, Ming-Hui Lu, Yan-Feng Chen, Yeshaiahu Fainman, and Axel Scherer. Nonreciprocal light propagation in a silicon photonic circuit. *Science (New York, N.Y.)*, 333(6043):729–33, August 2011

Steve Zamek, Liang Feng, Mercedeh Khajavikhan, Dawn T H Tan, Maurice Ayache, and Yeshaiahu Fainman. Micro-resonator with metallic mirrors coupled to a bus waveguide. *Optics Express*, 19(3):623–627, 2011

Steve Zamek, Dawn T H Tan, Mercedeh Khajavikhan, Maurice Ayache, Maziar P Nezhad, and Yeshaiahu Fainman. Compact chip-scale filter based on curved waveguide Bragg gratings. *Optics letters*, 35(20):3477–9, October 2010

ABSTRACT OF THE DISSERTATION

Near-Field Microscopy in Liquid for Accurate High-Resolution Optical Characterization

by

Maurice R. Ayache

Doctor of Philosophy in Electrical Engineering (Photonics)

University of California, San Diego, 2012

Professor Yeshaiahu Fainman, Chair

Near-field scanning optical microscopy (NSOM) is a powerful technique which allows deeply subwavelength imaging by placing a nanoscale aperture in close proximity to a sample where it can collect evanescent fields which contain information about subwavelength features. Additionally, by coupling out these evanescent fields, it has the ability to image light propagation within light-confining guided-wave structures. NSOM can be enhanced by integration into the signal arm of a heterodyne interferometer (H-NSOM), which allows imaging of both amplitude and phase at subwavelength resolution. In this dissertation we apply H-NSOM to characterize novel structures, and introduce a new technique for using H-NSOM in a liquid environment.

First, we use the H-NSOM to characterize an asymetric mode converter, which uses a one-way wavevector created by a metallic grating. The asymmetric propagation is visualized directly, then verified by using Fourier analysis to examine the mode content of the waveguide fields. Next, we propose and implement a scheme for H-NSOM measurement of silicon integrated waveguides with liquid cladding. Fourier analysis is used to determine an effective index shift of .08 in the quasi-TM mode between air and water overcladdings. This technique is then succesfully applied to directly image long range surface plasmons for the first time. The liquid cladding enables preservation of the symmetric cladding environment required for long range plasmon propagation. We directly observe the field distribution of the single mode, and show that it matches well to simulations.

Chapter 1

Introduction

In recent years the field of nanophotonics has grown to be an important area of science and engineering. Nanophotonics concerns the behavior of light at small scales, typically below the wavelength. Light at these dimensions may take on unexpected properties, due to the fundamental limits imposed by diffraction, and therefore it is a significant engineering challenge to design structures and tools capable of handling it, in addition to the fabrication challenges associated with these structures and tools in the first place. In this thesis I discuss several techniques for imaging and measuring nanophotonic devices with a heterodyne near-field scanning optical microscope (NSOM), the tool perhaps most associated with nanophotonic imaging. In order to provide some context for these experiments, we will briefly examine the history, physics, and technical importance of NSOM and integrated photonics.

1.1 Near-Field Microscopy

1.1.1 History

Although the earliest known lenses date back to ancient Assyria [5], where polished lenses were known for their ability to magnify, no known mathematical theories of optics were created until Euclid postulated his theory of geometrical optics in approximately 300 BCE. While this theory does not explain reflection or

refraction, it does lay out the basic principles of ray optics, with some similarity to modern understanding. Euclid's theory was extended by Hero of Alexandria to include mirrors, a fundamental component of many imaging systems. Snell's law of refraction was first understood by Persian philosopher Ibn Sahl around 984. In general, it was understood that a curved piece of glass could magnify an object, allowing the invention of spectacles in Medieval Italy. Still, until the Renaissance, optics lacked a formal engineering approach required to produce images of a desired size and magnification in a desired place.

This breakthrough occurred with the development of telescopes and microscopes in 17th-Century Europe. Although the early microscopes were simply single lenses, equivalent to a magnifying glass, the compound microscope with its separate optics for light collection and focusing into the eye was a sophisticated and powerful system. Likely invented by Galileo in 1609, its utility for biological studies was soon realized by Hooke and van Leeuwenhoek, who famously used it to observe the "thousands of living creatures in one small drop of water." Although magnification was increasing with the improving manufacturability of refractive lenses, the limited abilities of optical systems due to diffractive effects were not yet understood.

Francesco Grimaldi observed diffraction patterns and recorded his observations, which were published posthumously in 1665, noting that it was impossible for light to travel in rays and yet seem to "spread out" in the fashion it did. Soon Huuygens advanced a theory that rather than light being a ray or particle, it was a wave, an idea not widely accepted until in the 1800's Thomas Young performed the famous double-slit experiment which demonstrated interference, further demonstrated by Fresnel soon after. The wave theory of light allowed Ernst Abbe to derive his diffraction limit [6], which gives the minimum spot size d for an optical system:

$$d = \frac{\lambda}{2NA}, \tag{1.1}$$

where λ is the wavelength and NA gives the system numerical aperture. NA typically does not exceed 1.5, so, the diffraction limit indicates that any optical system cannot resolve any features smaller than roughly half to one-third the wavelength

of the system. The diffraction limit was further refined by Lord Rayleigh, who derived the resolution based on the ability of two separate points to be independently resolved [6]:

$$d = \frac{.61\lambda}{NA}. \tag{1.2}$$

The .61 factor derives from the radial position of the first null of an Airy disk, the diffraction pattern of a circular aperture, and (1.2) is known as the *Rayleigh Criterion*. The diffraction limit was a fundamental restriction to conventional optical imaging and numerous 20th century efforts in microscopy were devoted to circumventing it.

Some of these innovations included electron microscopy[7], which uses electrons rather than light, but has to be operated in vacuum with conductive samples; numerical aperture-increasing techniques, such as solid immersion lenses [8], 4Pi microscopy [9], and structured illumination microscopy [10]; and more modern nonlinear techniques such as stimulated emission depletion (STED) microscopy [11]. One technique that must be mentioned is confocal microscopy [12, 13], in which an illumination pinhole is imaged onto the sample rather than flooding the sample in light. This provides a slight increase in resolution and more importantly, prevents light from other parts of the sample entering the collection optics. In typical implementations, the sample (or in some cases the optical system) is scanned and the intensity is recorded at each point.

The basic idea behind NSOM was first realized by Irish physicist E.H. Synge, who wrote in a letter to Einstein in 1928 [14] that it should be possible to image subwavelength features by placing a subwavelength aperture in close proximity to a sample surface. Despite skepticism from Einstein, Synge later published his idea [15]. The difficulty of implementing such a scheme was explained in 1956 by mathematician John O'Keefe, who proposed something similar [16]: "The realization of this proposal is rather remote, because of the difficulty of providing for relative motion between the pinhole and the object, when the object must be brought so close to the pinhole." In 1972, Ash and Nicholls [17] implemented this concept at microwave frequencies; the high wavelengths involved did not require small apertures or sensitive probe-sample distance control. This was the

first demonstration of near-field imaging of electromagnetic waves. However, on its own, the concept was not scalable to the optical domain, which would require both apertures and probe-sample distances much smaller than the wavelength, on the order of 100s of nm or less.

The true breakthrough in the possibility of near-field imaging at optical wavelengths came in the early 1980s with the invention of scanning probe microscopy (SPM), which relies on a sensitive tip held close to a sample surface by negative feedback on a tip-sample interaction. The early SPMs were the scanning tunneling microscope (STM) and the atomic force microscope (AFM). STM, first devised by Binnig and Rohrer of IBM in 1981 [18], uses electron tunneling from conductive samples to measure the tip-sample height. AFM [19] works by feeding back against the mechanical interaction between the tip and sample to maintain a constant tip-sample distance. Since that time there have been a number of new SPM modalities, including magnetic force microscopy and kelvin probe force microscopy.

Optical near-field imaging was then independently developed by two teams, one at Cornell [20, 21], and one at IBM-Zurich [22], producing the first optical images at siginficantly subwavelength resolution. Since then, a number of new applications and techniques in NSOM have been created. NSOM has been successfully used for many purposes, including imaging of biological samples [21, 23, 24], testing of photonic and plasmonic structures, materials characterization, and photolithography [25].

1.1.2 Physical Principles and Engineering Design

The basic idea of confocal miroscopy, locally illuminating a sample one point at a time, then scanning, is an important concept which also serves as the insight behind NSOM. If one could focus a point of light to a spot smaller than that given by the diffraction limit (or equivalently, collect light from such a spot), it would seem possible to image with a resolution of that spot. However, diffraction specifically dictates that no such spot can be formed in the far-field. To further understand what happens when light strikes an object with subwavelength features,

it is instructive to examine the *angular spectrum representation* [26] of optical fields:

$$\vec{E}(x,y,z) = \iint_{-\infty}^{\infty} \vec{\tilde{E}}(k_x,k_y;0)e^{i(k_x x+k_y y+k_z z)}dk_x dk_y \tag{1.3}$$

(1.3) means that a planar field distribution with a set of spatial frequencies (k_x, k_y) will propagate to the z-plane with frequency k_z. This propagator is subject to the condition that:

$$k_x^2 + k_y^2 + k_z^2 = k^2 = \left(\frac{2\pi n}{\lambda}\right)^2, \tag{1.4}$$

for medium refractive index n, which can also be written:

$$k_z = \sqrt{\left(\frac{2\pi n}{\lambda}\right)^2 - (k_x^2 + k_y^2)}. \tag{1.5}$$

Under normal imaging conditions, $(k_x^2 + k_y^2) < k$, and the object propagates to arbitrary z-planes. However, when the object plane contains sufficiently high spatial frequencies (i.e. features smaller than the wavelength), the number under the square root in (1.5) becomes negative, making k_z imaginary. When inserted in (1.3), it causes the spectrum to decay in the z-direction rather than propagate. This piece of information is at the center of the near-field imaging, as it means that information about subwavelength features *still exists, in evanescent waves close to the object surface*. If one can place a sufficiently small aperture at a sufficiently close distance (in order to minimize the effect of evanescent decay) to the object plane, subwavelength imaging is feasible.

In short, the operation of an NSOM may be described in the following way. A subwavelength optical probe scans over a surface at a close, typically constant distance ($h \ll \lambda$), where it interacts with the near-field of the surface fields, causing light to be coupled from the near-field into the far-field, where it is collected by a detection system. When the NSOM is being operated in *collection mode*, the sample is being excited while the probe couples light to the detection system. In *illumination mode* the light is injected through the probe aperture to create a nanoscale spot on the sample, and the detection system detects the light that is

reflected or transmitted (which can further be divided into *reflection mode* and *transmission mode* respectively. In some cases, for example the probe blocking incoming or emitted light, the NSOM may be operated in *illumination-collection* mode, where both the parts of the optical system run through the tip. It should be noted that in principle, the illumination and collection modes are equivalent, due to electromagnetic reciprocity. In practice, there may be functional reasons for choosing one or the other. For instance, if high optical powers are required, there is a risk of burning the probe due to high concentrations of field at the metal-dielectric interface. In this work all experiments are done using collection mode.

NSOM probes may generally be divided into *apertureless* [27] and *aperture* designs. The apertureless design consists of a subwavelength particle, or an AFM-type tetrahedral probe with a subwavelength tip, that radiates into free space, where it may be collected by a lens. This style can exhibit very high resolution, but the meanings of the images it produces may be unclear due to multiple-scattering effects, and because of the wide-field collection necessary it is subject to siginficant noise. The more common design, discussed in this thesis, is the aperture probe, which is a subwavelength aperture in a metal film. The metal film must be thicker than the skin depth of the metal at the wavelength of operation, so that the only measured signal comes from light transferred through the aperture. Typically, the aperture is formed at the end of a tapered metal-coated fiber (although some designs use an aperture in free space), which may be fabricated by heating and pulling [28, 29] or chemical etching [30]. After the taper is formed, metal is evaporated to form the aperture. Apertures down to 20 nm may be fabricated by these methods. When a field is coupled through the aperture, it conveniently enters the fiber where it is accessible for NSOM analysis.

When the aperture is placed in an evanescent field, light is coupled through it into the fiber or free space (or vice versa in the case of illumination mode). It is well-known that an evanescent field carries no energy in the direction of decay, so there must be some means to convert the near-field signal into a far-field signal. The presence of the probe acts as a perturbation, with the sample near-field directly

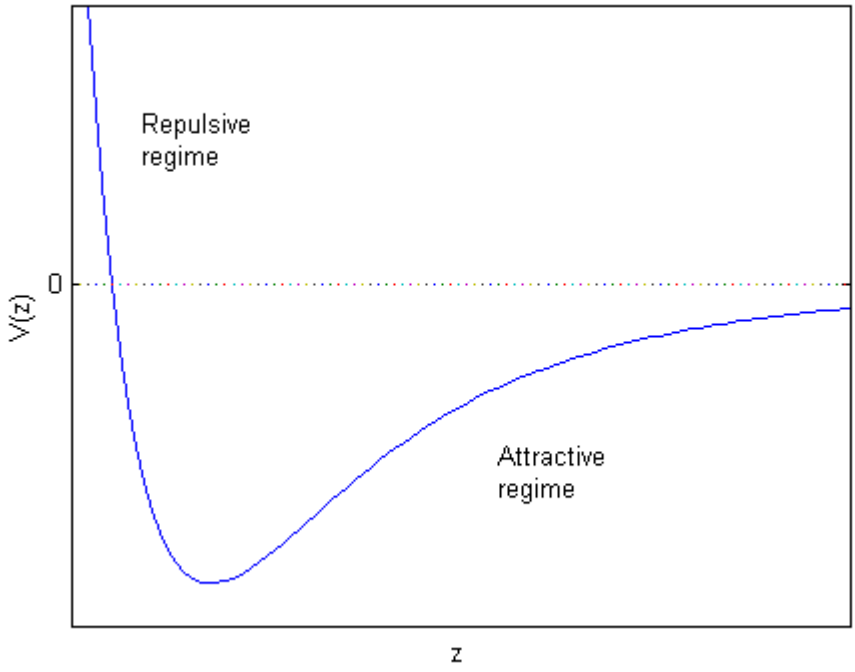

Figure 1.1: Tip-sample interaction potential V as a function of distance between the two z. At intermediate range the Van der Waals attraction dominates, while at short range the electrostatic repulsion dominates.

interacting with the tip near-field to couple to the fiber's propagating modes. Due to the subwavelength size of the aperture, very little light is transmitted through it. According to the Bethe-Bouwkamp model of diffraction through small holes [31, 32], $T \propto \left(\frac{d}{\lambda}\right)^4$. This implies a rapid decline in transmission as one attempts to improve the resolution by decreasing aperture size. In typical experiments, this corresponds to a transmission on the order of $10^{-6} - 10^{-9}$. Therefore it is important to use methods such as interferometry and avalanche detection as well as high source power to increase available signal to detectable levels.

The probe is scanned across the surface at nanometric resolution. The scan is actuated by a piezoelectric crystal, allowing sufficiently small steps such that the resolution is limited by the probe rather than the scanner. The image is formed by point-by-point recording of the field intensity (or other quantity of interest). As it is scanned, the probe must be maintained at a constant height above the

sample surface to prevent damage to either one. Since the sample may have an uneven topography, this requires an active feedback mechanism. Although this is occasionally done with electron tunneling as in STM, it is most commonly done through atomic force feedback. When the probe is brought close to the surface, molecular interactions between the tip and the sample are used to measure the distance. A qualitative diagram of these interactions may be seen in Fig. 1.1. At medium range, the Van der Waals force, which is attractive in nature, dominates while at close range, the interaction is governed by the Coulombic electrostatic repulsion (ESR). The ESR goes to infinity as the probe and sample get closer, so it is essential that the probe be held where the net force is small. Of course, when the probe is far away the probe-sample interaction goes asymptotically to 0.

There are a number of ways in which the force on the probe may be measured. In normal force feedback, the bent probe is mounted on a horizontal tuning fork and oscillated vertically [33]. As the probe comes into contact with the sample, the resonance shifts due to the Van der Waals and electrostatic forces. In shear force feedback, the probe is mounted on a vertical tuning fork and oscillated side to side. Though the exact forces in this case are not well understood, likely candidates include capillary action, friction, and viscous drag. In beam-bounce feedback, a laser beam is reflected off the top of the probe, and its deflection off-center is measured by a position-sensitive detector (PSD). The beam-bounce configuration may be used to measure the probe resonance in a normal-force scheme, or it can directly measure the deflection of the probe due to ESR. The former arrangement is called "tapping mode", due to the probe oscillation, while the latter is called "contact mode", since the probe is in continuous rather than intermittent contact with the sample. Although contact mode may offer higher signal strengths, the strong-probe sample interaction may be damaging to one or the other.

The feedback signal (tuning fork resonance shift, beam deflection, etc.) is connected to a control mechanism, typically a PID (proportional-integral-derivative) controller. The controller drives a vertical scanner so as to hold the feedback signal constant, thereby maintaining the tip at a constant height. Since the error signal (the difference between present and target value of the feedback signal) reflects

changes in the sample height, and therefore acts mostly as a derivative of the topography, the integral value is generally highest, in order to ensure that responses to rapid changes are held in place for a long time. Specific values of the PID multipliers should be set for each individual probe according to control theory. At each point in the scan, the tip height is adjusted to reflect the sample height, which has the side benefit of producing a map of the sample topography in addition to the optical quantities of interest. For aperture NSOM, the topography is generally not as good as that measured by a purpose-built AFM, due to the width (∼300-500 nm) of the aperture tip which limits the mechanical resolution. Scattering-type (apertureless) probes may see improved lateral resolution.

1.2 Integrated Photonics

The notion of integrated photonics comes from two major technological advances: electronic integration and photonic telecommunications. Electronic integration began with the invention of the transistor [34] by Shockley and his team at Bell Labs, for which they were later awarded the Nobel Prize. This allowed logical operations to be performed in electronics completely in the solid state. The next fundamental step in this area was the invention of the integrated circuit [35], primarily developed by Jack Kilby at Texas Instruments, for which he too was awarded the Nobel Prize. Integration revolutionized computing by enabling many electronic components, including transistors, to be packaged on a single chip, in an automated and repeatable fashion. Large-scale integration led to major progress in computing power, while automation substantially brought down the cost of computation. In 1965, Intel founder Gordon Moore predicted [36] that transistor density on silicon chips would double every 18 month's. Moore's Law has been consistently upheld, and indeed the doubling time has even dropped to about 1 year, although many experts believe it is reaching its limits due to on-chip heat generation and quantum tunneling effects.

Around the same time came the development of photonic communication. In principle communicating at optical rather than radio frequencies is preferable,

as it allows higher bandwidth. Since free-space communication is impractical due to line-of-sight restrictions, long-distance optical waveguides were required. Although the concept of dielectric wave guiding by total internal reflection had been known since the mid-19th century, innovations in the 1930s and 40s developed the idea of using a thin glass rod coated with a lower-index cladding. Initially optical fiber was developed for medical imaging, for which their 1 dB/m loss was acceptable, but unusable for telecommunication. In the 1960s, Charles Kao of Standard Telecommunications Lab in the UK demonstrated [37] that these losses were due to impurities in the glass rather than the glass itself, a realization which began the fiber optic communications revolution.

The success of these two areas has led to a great deal of interest in integrating photonics on chip, in particular using the standard CMOS processes already available to industry at low cost. Photonic integration has the capacity to transfer large optical systems composed of many bulky optical components onto single chips, reducing footprint and improving predictability and repeatability. Additionally, adding photonic components to microelectronics may be useful in increasing speed and decreasing heat generation, helping to forestall the decline of Moore's Law. Silicon photonics [38], first suggested by Soref [39] takes advantage of silicon's low absorption in the near-infrared and leverages the existing infrastructure used for microelectronics to create the next generation of photonic devices.

1.3 Near-Field Measurements of Integrated Photonics

The development of integrated photonic devices, in particular at the industrial scale, requires reliable testing and characterization methods to determine device functionality and performance, as well as understand the physics of various designs. In many cases the standard for characterization is transmission and reflection testing using bench-top fiber and free-space measurement systems. Although this kind of far-field 'black box' testing is very useful for determining whether a photonic circuit works as designed, and often for quantitatively characterizing the

degree to which it works, it lacks the ability to measure local properties, and thus frequently cannot determine why a device does not work, or isolate a problematic component in a system. The 'cutback' method, in which portions of the chip are successively removed and measurements taken at each one, has had some success [40], but has numerous disadvantages such as destroying the chip, not allowing 'in-situ' characterization of the final device, consuming a considerable amount of time, and requiring realignment of the optical system for each measurement which may not be identical. Additionally, it does not offer the opportunity to image the fields as they propagate.

Near-field microscopy offers an opportunity in this regard. Light propagating in a waveguide or waveguide-based device has an evanescent field at each core-cladding boundary. This means that where the top is accessible, the NSOM probe can be used to access this evanescent field. If we take the evanescent field to be representative of the confined field as a whole (in terms of relative magnitude, phase, etc.) it offers a useful insight into device operation. When the probe is placed at a distance from the waveguide much shorter than the decay length, some of the evanescent field couples into the probe and the detection system. Even though the Poynting vector of the field is typically along the waveguide (i.e. perpendicular to the probe), there is an exponential decay in the direction parallel to the probe that can be coupled by scattering into the optical fiber. This phenomenon is inherently perturbative, as the presence of the probe affects the mode propagation due to scattering, but this perturbation occurs 'downstream' from the probe, so for non-resonant devices the NSOM image can be taken to be a reliable representation of the field in absence of the probe [41].

Although fabrication and simulation technology has improved steadily, numerous defects such as etch roughness, proximity effect, and under-etching contribute in unpredictable or poorly quantifiable ways to integrated photonic device performance, making their incorporation into simulations impractical. Therefore, local characterization techniques are necessary to fully understand device operation and properties. First explored by Choo et al. [42] and Toda et al. [43], NSOM characterization of waveguide-based devices is now a well-established tech-

nique [44, 45, 46]. In addition to simple channel waveguide structures, this mode of NSOM, known as photon scanning tunneling microscopy (PSTM) [47], can also be used for photonic crystal [48, 49] and plasmonic waveguides [50, 51], as well as any number of guided-wave devices.

In this dissertation we make use of a heterodyne NSOM (H-NSOM) which has the capability of imaging phase. This technique was first introduced by Phillips et al. in 2000 [52] using a pseudoheterodyne Mach-Zehnder interferometer, and soon expanded to a full heterodyne arrangement [53, 54, 55]. With the sample and NSOM tip placed in the signal arm of a Mach-Zehnder interferometer, with a modulated external reference as the other arm, it is possible to quantitatively detect phase, and the SNR increases substantially, for reasons explained in Section 2.2. Using short-pulse lasers [56], or low-coherence sources [57], H-NSOM is capable of doing time-resolved measurements. It can also fully characterize complex polarization [58] and even magnetic field [59]. Although here we principally discuss aperture NSOM, it should be noted that the heterodyne setup can be applied to apertureless NSOM as well [60].

1.4 Organization of the Dissertation

This dissertation discusses characterization of integrated photonic devices and introduces the technique of heterodyne near-field imaging under liquid cladding. It presents several structures and describes their design and fabrication, explains how NSOM can be applied to characterize them, and shows how the NSOM data can be effectively analyzed. The disseration is organized as follows:

Chapter 2 describes the NSOM setup in detail and discusses the behavior of the heterodyne interferometer.

Chapter 3 discusses a novel asymmetric mode converter. After describing the concept of the device, we present maps of the near field and introduce Fourier analysis of the complex field.

Chapter 4 introduces the new technique of near-field imaging of amplitude and phase in a liquid-clad structure, using silicon waveguides as a model system.

Experimental considerations necessary to the device design and microscope setup are analyzed, and measured data are presented to validate and justify the technique.

Chapter 5 presents near-field images of long range surface plasmons, enabled by the liquid cladding method. Once again, the necessary considerations for device design to accomodate the measurement are presented, as well as measured data and detailed analysis.

Chapter 6 concludes the dissertation with a summary of contributions.

Chapter 7 suggests future directions for research to follow what has been presented here.

Chapter 2

Experimental Setup

2.1 NSOM System

All experiments in this thesis were performed with a Nanonics NSOM head and SPMD-260 controller, which is run using Nanonics NWS (NanoWorkShop) software. The work done with NSOM in a liquid environment uses the Nanonics MV-1000 head with liquid cell, while the work without any liquid uses the Nanonics MV-2000 head. The MV-1000 uses beam-bounce normal-force feedback without any tuning fork and it is operated in tapping mode, based on the mechanical resonance of the probe itself. The MV-2000 also uses normal-force feedback in tapping mode, but the probe is mounted on a piezoelectric tuning fork, which returns the mechanical oscillation amplitude to the controller via a pair of magnetic metal contacts which also attach the probe mount to the head. The probes are bent fiber aperture probes supplied by Nanonics Imaging, Ltd, constructed from single-mode (SMF-28) optical fiber with a gold coating and a chromium adhesion layer. Aperture sizes range from 50 nm to 250 nm, though most experiments are done with apertures between 150 and 200 nm, which empirically provide a reasonable balance between resolution and SNR (signal-to-noise ratio).

X-Y scanning is done by 2 pairs of piezoelectric crystals which each of a range of $\sim 35\mu$m, for a total scan distance of $\sim 70\mu$m, with either axis being allowed to be the fast or slow axis. On the MV-1000 the sample is scanned, while on the MV-2000 the tip is scanned. Another $\sim 35\mu$m piezo scanner raises and

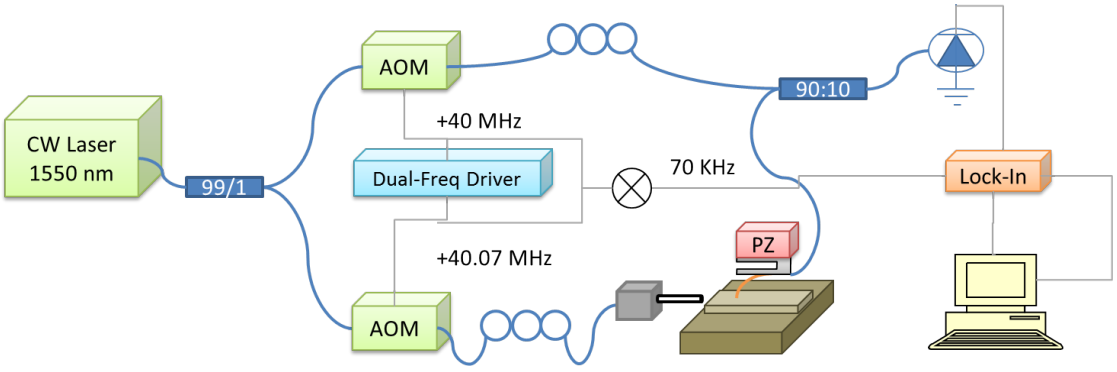

Figure 2.1: Diagram of the heterodyne interferometer. NSOM in signal arm. Signal and reference arms acousto-optically modulated at slightly different frequencies. Difference frequency used as reference for lock-in amplifier.

lowers the tip according to the feedback gains to accomodate the topography of the sample. The head performs a raster scan of the sample, collecting topographic and optical data at each point in the scan through the data translation box. The images are then reconstructed point-by-point in software. MATLAB code was written to plot and analyze the images produced by the NWS software.

2.2 Heterodyne Interferometer

The NSOM probe is integrated into a heterodyne interferometer [61], in order to allow phase acquisition, and improve measured SNR. The setup is shown in Fig. 2.1. The source is a laser at 1550 nm, which is split into a signal and reference arm by a 2x2 90:10 coupler. The asymmetry in coupling strengths is chosen due to the low optical power transmitted through the tip. On each arm the splitter is connected to an acousto-optic modulator (AOM), one at 40.00 MHz, the other at 40.07 MHz. The two AOMs are driven by a common-phase RF dual frequency generator, which also outputs reference signals at those frequencies connected to an RF mixer. The 70 kHz difference frequency signal from the mixer serves as a reference for the lock-in amplifier.

On the reference arm, after the AOM there is a set of polarization paddles, which can be used to align the reference polarization with that of the signal from the tip for maximum interferometric intensity. There is also a variable delay line

which may be used for low-coherence time-resolved NSOM measurements. On the signal arm, the light proceeds from the AOM to a set of polarization paddles, which is used to align the incoming signal polarization with the linear polarizer which follows, to insure that the input field is in a linearly polarized state; the fiber is mounted in a chuck which may be rotated to vary this polarization between horizontal and vertical. The light then enters the sample, where it propagates partway through, and is then picked up by the near-field tip into another optical fiber. The near-field signal from this fiber is then interferometrically mixed with the reference in a 99:1 2x2 coupler, with the ratio chosen due to low near-field signal strength. The superposed fields strike a Laboptic DPT100FC-15V insert detector detail here photodector, the output of which is used as the input of a lock-in amplifier. The amplitude and phase are taken from the lock-in amplifier and read into the computer via the NWS software.

In order to understand the behavior of the heterodyne detection system in relation to the NSOM, we now mathematically derive the photodetector signal as a function fo the input field paramters. Before the AOM, the field on the reference arm at time t may be modeled as:

$$E_{ri}(t) = \sqrt{I_{ri}} e^{i(\omega t + \phi_{ri})}, \tag{2.1}$$

where I_{ri} is the initial field intensity, $\omega = \frac{2\pi c}{\lambda}$ is the frequency, and ϕ_{ri} is an arbitrary phase shift. The AOM then shifts the frequency by $\Delta\omega_r = 40.00$ MHz, using the Doppler shift of the first order of a moving acoustically-induced Bragg grating. This gives a reference field:

$$E_r(t) = \sqrt{I_r} e^{i((\omega + \Delta\omega_r)t + \phi_r)}. \tag{2.2}$$

We have changed the notation for the intensity and phase here to reflect the loss and phase shift due to the AOM and fiber, but it will be seen that these are of no consequence in the final result. We may follow a similar derivation to obtain the field on the signal arm:

$$E_s(x, y, t) = \sqrt{I_s(x, y)} e^{i((\omega + \Delta\omega_s)t + \phi_s(x,y))}. \tag{2.3}$$

Note that the signal intensity and phase (and thus the field) are now functions of the tip position (x, y). It is of course expected that the field will vary over the area of the scan.

The fields of the two arms are then superposed by the coupler, which gives an interference intensity:

$$I(x,y,t) = |E_r + E_s|^2 \tag{2.4}$$

$$= |E_r|^2 + |E_s|^2 + \sqrt{I_r}\sqrt{I_s}e^{i((\Delta\omega_s - \Delta\omega_r)t + \phi_s - \phi_r(x,y))} + c.c. \tag{2.5}$$

$$= I_r + I_s(x,y) + \sqrt{I_r I_s(x,y)}\cos((\Delta\omega_s - \Delta\omega_r)t + \phi_s(x,y) - \phi_r) \tag{2.6}$$

This signal is then coupled into the photodetector, with responsivity R, which converts the intensity into a voltage:

$$V(x,y,t) = V_{bg} + R\sqrt{I_r I_s(x,y)}\cos((\Delta\omega_s - \Delta\omega_r)t + \phi_s(x,y) - \phi_r) \tag{2.7}$$

Here the first two terms in (2.4) are rolled into a background voltage V_{bg}, since the lock-in amplifier selects out the term which are at its reference frequency. It can be seen that the two slightly different optical frequencies of the two arms subtract to form an RF beat frequency, 70 kHz in this case. The reference frequency put out by the mixer is the difference between the modulation frequencies of the two arms $\Delta\omega = (\Delta\omega_s - \Delta\omega_r)$, identical to the frequency of the final term in (2.7). The lock-in amplifier therefore reports the amplitude and phase of this cross term. At any given point (x, y) the amplitude is proportional to the field amplitude (square root of the intensity) $I_s(x, y)$ coupled by the tip, with the proportion being given by the detector responsivity, the reference field amplitude, and the loss in the fiber and components. The phase is given as $\phi_s(x, y) - \phi_r$, also as a function of the tip position. This is the signal phase relative to a constant reference ϕ_r; the reference phase is not important as we are only concerned with the relative phases at different points in the scan. Therefore the heterodyne NSOM allows simultaneous acquisition of topography, amplitude and phase.

In addition to phase-imaging capability, the heterodyne setup also provides the NSOM with an increase in signal power. Since photodetectors only measure the intensity, if the tip were connected directly to the detector, the voltage would

be proportional to I_s, which as established in 1.1.2 is quite small due to low tip transmission. However the heterodyne setup measures the field amplitude $\sqrt{I_s}$, meaning it drops with decreasing aperture diameter (and therefore increasing resolution) according to d^{-2} rather than d^{-4} as in the intensity case. Additionally, the multiplication by the reference field amplitude $\sqrt{I_r}$ provides an additional gain. Overall the interferometer provides a gain of $\sqrt{\frac{E_r}{E_s}} \sim 10^4$ over the non-interferometric case. Furthermore, the lock-in amplifier provides gain according to the chosen sensitivity, but this gain also amplifies electronic noise that occurs between the detector and the amplifier.

We now discuss the noise performance and accuracy of the detection system, principally following the analysis presented in [62]. The SNR of the detection system may be written:

$$SNR = \frac{P_{AC}}{P_{SN} + P_{TN}}, \tag{2.8}$$

where P_{AC} is the total AC signal power at the detection frequency (determined by the square of the interference cross-term in (2.7)), $P_{SN} = 2eBSP_{opt}R_0$ is the shot noise power due to the quantization of the electric charge (for bandwidth B, sensitivity S, optical power P_{opt}, and detector resistance R_0) and $P_{TN} = d4k_BTB$ is the Johnson (thermal) noise power due to thermal fluctuations of the electrons (where k_B is Boltzmann's constant, and T is temperature). Since the shot noise power is proportional to the incident optical power on the detector, $P_{opt} = P_r + P_s$ (sum of the reference and signal arm powers), if the power is sufficiently high the detection will be in the shot noise limit, which is desirable as it asymptotically maximizes the SNR. Generally we have $P_r \gg P_s$, so the shot noise power is dominated by the reference arm. Here the interferometric setup is advantageous as the reference power may be tuned to put the system into the shot noise limit, as long as it does not saturate the detector or data acquisition system. In practice, this setup does operate in the shot noise limit [62].

Knowing the SNR, we may determine the errors in the amplitude and phase reported by the lock-in amplifier. The relative standard deviation of the relative

amplitude, calculated in terms of the signal and noise currents i_N and i_{AC}, is:

$$\frac{\Delta V}{V} = \sqrt{\frac{\overline{i_N^2}}{\overline{i_{AC}^2}}} = \frac{1}{\sqrt{SNR}}. \tag{2.9}$$

It can also be shown that the absolute standard deviation in the phase due to noise can be written:

$$\Delta\phi = \frac{1}{\sqrt{SNR}} \tag{2.10}$$

This of course is identical to the relative amplitude error given in (2.9). Empirically, typical power SNR for this system, measured according to the voltage, is on the order of 50 dB. This corresponds to a phase deviation of approximately .2° due to electronic noise. However, larger variations may be observable due to thermal fluctuations and drift of the coupling fiber. The effect of phase drift is treated further in Subsection 4.4.1

Chapter 3

Asymmetric Mode Converter Validated by NSOM

3.1 Background

The breaking of time-reversal symmetry of light is typically achieved with magneto-optical materials that introduce a set of antisymmetric off-diagonal dielectric tensor elements [63, 64] or by involving nonlinear optical activities [65, 66]. However, practical applications of these approaches are limited for the rapidly growing field of silicon (Si) photonics because of their incompatibility with conventional complementary metal-oxide-semiconductor (CMOS) processing. Si optical chips have demonstrated integrated capabilities of generating [67, 68, 69, 70, 71], modulating [72], processing [73] and detecting [74] light signals for next-generation optical communications but one component which has not been demonstrated is an asymmetric mode converter.

Parity-time (PT) symmetry is crucial in quantum mechanics. In contrast to conventional quantum mechanics, it has been proposed that non-Hermitian Hamiltonians where $\hat{H} \neq \hat{H}^{\dagger}$ can still have an entirely real spectrum with respect to the PT symmetry [75, 76]. Due to the equivalence between the Schrdinger equation in quantum mechanics and the wave equation in optics, PT symmetry has been studied in the realm of optics with non-Hermitian optical potentials [77, 78, 79].

The breaking of PT symmetry has recently been experimentally observed, showing asymmetric characteristics transverse to light propagation above the PT threshold [80, 81]. Here, we have designed a Si waveguide integrated with complex optical potentials that have a thresholdless broken PT symmetry along the direction of light propagation.

3.2 Theory

On a Si-on-insulator (SOI) platform, the designed two-mode Si waveguide is 200 nm thick and 800 nm wide, allowing a fundamental symmetric quasi-TE mode with a wave vector of $k_1 = 2.59k_0$ and a higher-order antisymmetric mode with a wave vector of $k_2 = 2k_0$ at the wavelength of 1.55 µm. Periodically arranged optical potentials are implemented in the Si waveguide and occupy half of the waveguide width in the x direction (Fig. 3.1(a)). The optical potentials have a complex modulation in their dielectric constants along light propagation in the z direction compared with the Si waveguide background ($\varepsilon_{\mathrm{Si}} = 12.11$), as shown in Fig. 3.1(b)

$$\Delta\varepsilon = e^{iq(z-z_0)} \tag{3.1}$$

where $q = k_1 - k_2$, and z_0 is the starting point of the first modulation region. This complex exponential variation of $\Delta\varepsilon$ along the z direction introduces a one-way wave vector that is intrinsically asymmetric because its corresponding Fourier transform is one-sided to the guided light inside the Si waveguide. These complex optical potentials are located in phase with each other with a spacing of $2\pi/q$ (or multiples of $2\pi/q$) in between, such that light modulation always remains in phase with and is consistently applied to guided light. We chose the dielectric constant modulation to be completely passive in order to make the experiment easier to perform, meaning that the modulation length of each optical potential is π/q. Therefore, no gain is required to construct these optical potentials. From a quantum mechanics analysis, these optical potentials have a spontaneously broken PT symmetry with a non-Hermitian Hamiltonian $\hat{H}^\dagger(x,z) \neq H(x,z)$ or $\hat{H}^\dagger(x,-z) \neq H(x,z)$, suggesting noncommutative binary operations to the Hamiltonian $PT\hat{H}^\dagger \neq \hat{H}PT$.

In our system, this is observed as asymmetric mode conversion through the optical potentials in the Si waveguide.

More intuitively, the introduced one-way wave vector q shifts the incoming photons of the symmetric mode with an additional spatial frequency: $k_1 + q$ for forward propagation and $-k_1 + q$ for backward propagation. The mode transition between the symmetric mode and the antisymmetric mode can happen only when the phase-matching condition is approximately satisfied $\Delta k = \pm(k_1 - k_2) + q \approx 0$, where + and - represent forward and backward propagation, respectively. In our case, for an incoming symmetric mode the phase-matching condition is only valid in the backward direction, supporting a one-way mode conversion from k_1 to k_2 (Fig. 3.1(c)). In the modulated regime, the electric field of light is given by:

$$E(x,z,t) = A_1(z)E_1(x)e^{i(k_1 z - \omega t)} + A_2(z)E_2(x)e^{i(k_2 z - \omega t)} \tag{3.2}$$

where $E_{1,2}(x)$ are normalized mode profiles of two different modes, and $A_{1,2}(z)$ are the corresponding normalized amplitudes of two modes, respectively. Assuming a slowly varying approximation, the coupled-mode equations can be expressed as follows:

$$\begin{aligned}
\frac{d}{dz}A_1(z) &= -iB_1\exp(-iqz)A_1(z) - iC_1A_2(z) \\
\frac{d}{dz}A_2(z) &= -iC_2\exp(-i2qz)A_1(z) - iB_2\exp(-iqz)A_2(z)
\end{aligned} \tag{3.3}$$

for forward propagation and

$$\begin{aligned}
\frac{d}{dz}A_1(z) &= iB_1\exp(-iqz)A_1(z) + iC_1\exp(-i2qz)A_2(z) \\
\frac{d}{dz}A_2(z) &= iC_2A_1(z) + iB_2\exp(-iqz)A_2(z)
\end{aligned} \tag{3.4}$$

for backward propagation, where $B_1 = \frac{1}{2k_1}\frac{\omega^2}{c^2}\frac{\int E_1^*(x)E_1(x)dx}{\int |E_1(x)|^2dx}$, $C_1 = \frac{1}{2k_1}\frac{\omega^2}{c^2}\frac{\int E_1^*(x)E_2(x)dx}{\int |E_1(x)|^2dx}$, $C_2 = \frac{1}{2k_2}\frac{\omega^2}{c^2}\frac{\int E_2^*(x)E_1(x)dx}{\int |E_2(x)|^2dx}$, and $B_2 = \frac{1}{2k_2}\frac{\omega^2}{c^2}\frac{\int E_2^*(x)E_2(x)dx}{\int |E_2(x)|^2dx}$. The mode transition can happen only when the phase-matching condition is satisfied as the exponential term disappears because $\exp(-i\Delta kz) = 1$. Therefore, it is evident that with an initial condition of $A_1 = 1$ and $A_2 = 0$, photons from the symmetric mode can be converted to the antisymmetric mode only for backward propagation, whereas

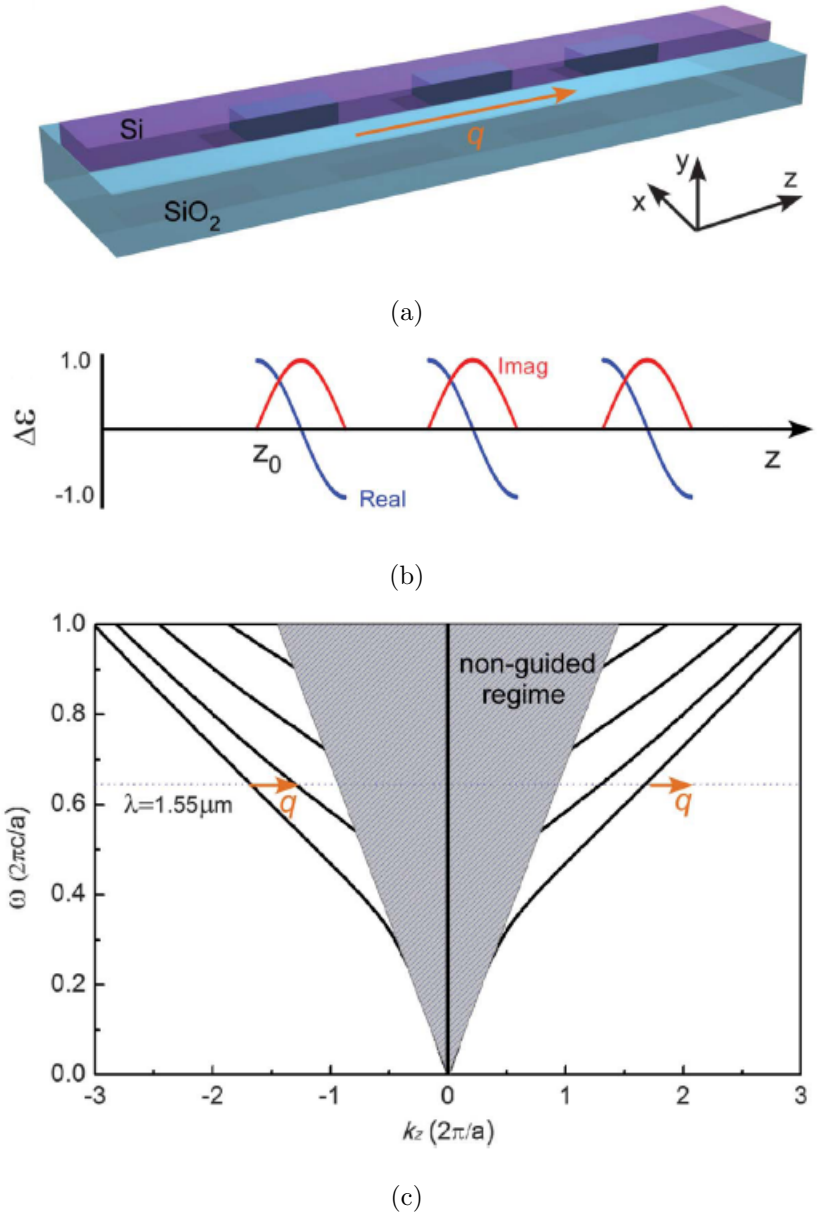

Figure 3.1: (a) Asymmetric mode conversion in a silicon photonic device, in the "ideal" design . Based on a SOI platform, PT optical potentials with exponentially modulated dielectric constants, as depicted in (B) where blue and red curves represent the real and imaginary parts of $\Delta\varepsilon$, respectively, are embedded in the Si waveguide to introduce an additional wave vector q to guided light. (c) Band diagram for TE-like polarization of the Si waveguide, where the frequency and wave vector are normalized with $a = 1\mu$m. At the wavelength of 1.55 m, if incoming light is a fundamental symmetric mode, one-way mode conversion is only expected for backward propagation where the phase-matching condition is satisfied as indicated by arrows.

A_2 remains 0 for forward propagation, indicating negligible mode conversion. The asymmetric nature of the mode transition here results from the spontaneous breaking of the PT symmetry of guided light by the engineered complex optical potentials. It is worth emphasizing that this unidirectional mode transition is always valid with any modulation intensity, indicating a completely thresholdless breaking of PT symmetry (22), in stark contrast to previous work on threshold PT symmetry breaking (20, 21).

Fully vectorial three-dimensional (3D) finite element method simulations have been performed to validate the proposed asymmetric propagation of guided light at the telecom wavelength of 1.55 µm. With a TE-like symmetric incident mode, after forward propagating through the PT optical potentials where $\Delta\varepsilon$ follows the exponential modulation, guided light does not meet any phase-matching condition with the additional wave vector q and therefore retains the same symmetric mode profile. However, for backward propagation, it is evident that the antisymmetric mode is converted from the incoming symmetric mode due to the phase matching with the additional wave vector q, showing a one-way mode transition (Fig. 3.1(a)). The asymmetric mode conversion can also be analytically calculated using the coupled-mode theory from (3.3) and (3.4), consistent with the simulated results.

3.3 Design and Implementation

However, the approach so far demonstrated to create the exponentially modulated $\Delta\varepsilon$ [81] is difficult to integrate with Si photonics. It is therefore necessary to design an equivalent guided-mode modulation that at a macroscopic scale mimics the intrinsically microscopic exponential modulation of the PT optical potentials. To simplify fabrication, each complex exponential modulation is separated into two different modulation regions: one providing only the imaginary sinusoidal modulation of the dielectric constant covering one transverse half space (bottom) of the waveguide, and the other creating the real cosine modulation occupying the other

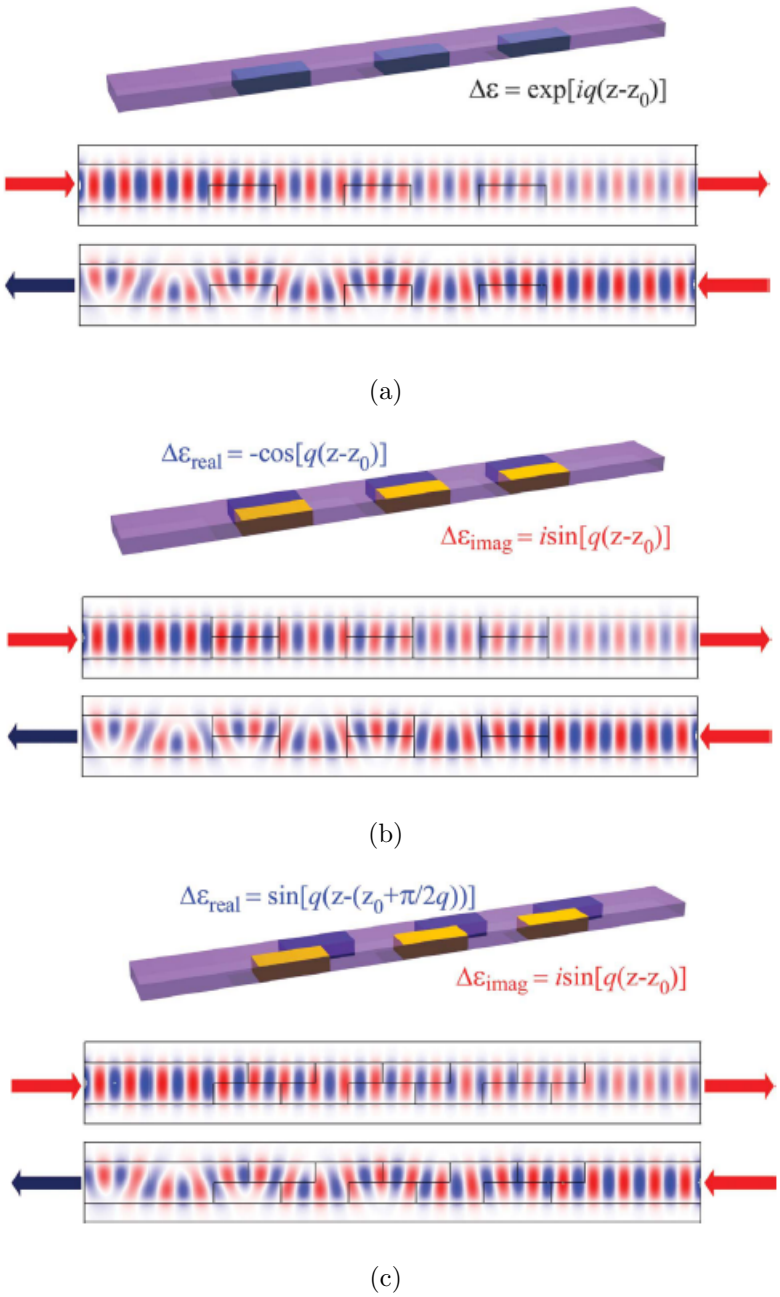

Figure 3.2: Evolution of PT optical potentials in the Si waveguide (top) and their corresponding field distributions of E_x for forward (middle) and backward (bottom) propagation with an incoming symmetric mode. (a) Original PT optical potentials with exponentially modulated dielectric constant. (b) Two different kinds of optical potentials with real cosine and imaginary sinusoidal modulated dielectric constants. (c) Optical potentials with the real part modulation in (B) are shifted $\pi/2q$ in the z direction.

transverse half space (top) of the waveguide (Fig. 3.1(b)), as follows:

$$\Delta\varepsilon_{real} = -\cos[q(z - z_0)]$$
$$\Delta\varepsilon_{imag} = i\sin[q(z - z_0)] \tag{3.5}$$

Although individual sinusoidal or cosine modulation does not contribute to the breaking of PT symmetry, simultaneous modulations of both cause an equivalent one-way mode transition. Guided light in different half spaces experiences complementary mode modulation from each other and therefore behaves as if the PT optical potentials do exist. Moreover, to have only the positive $\Delta\varepsilon_{real}$ of the modulations for ease of fabrication, regions of $\Delta\varepsilon_{real}$ are shifted $\pi/2q$ in the z direction: $\Delta\varepsilon_{real} = \sin[q(z-(z_0+\pi/2q)]$ (Fig. 3.2(c)). The resulting one-way mode transition of guided light consequently remains the same.

Finally, to achieve sinusoidal optical potentials using microscopically homogeneous materials, sinusoidal-shaped structures are adopted on top of the Si waveguide for both real and imaginary modulations to mimic the modulations described in (3.5) (Fig. 3.3(a)). An 11-nm germanium (Ge)/18-nm chrome (Cr) bilayer structure is applied for the imaginary modulation $\Delta\varepsilon_{imag}$ as guided modes have the same effective indices as $\Delta\varepsilon = i$. For the real modulation $\Delta\varepsilon_{real}$, an additional 40-nm Si layer on top of the original Si waveguide achieves the same effective indices of guided modes as $\Delta\varepsilon = 1$. The length, period, and locations of these sinusoidal shaped structures follow those in Fig. 3.2(c). The designed sinusoidal-shaped structures have almost the same effective indices of the waveguide modes, as if the real and imaginary function-like modulations exist in the waveguide (Fig. 3.3(b) and (c)), such that the same unidirectional wave vector q can be introduced. Therefore, an equivalent one-way mode transition is realized, as shown in Fig. 3.3(d): Forward propagating light remains in the symmetric profile, whereas mode conversion from the symmetric mode to the antisymmetric mode exists for backward propagation. It is thus evident that our classical waveguide system successfully mimics the quantum effect inherently associated with a broken PT symmetry. Overall, at different steps of the evolution of PT optical potentials from Fig. 3.2 to Fig. 3.3, guided light exhibits almost identical phase and intensity for both forward and backward propagation, further proving the equivalence of our

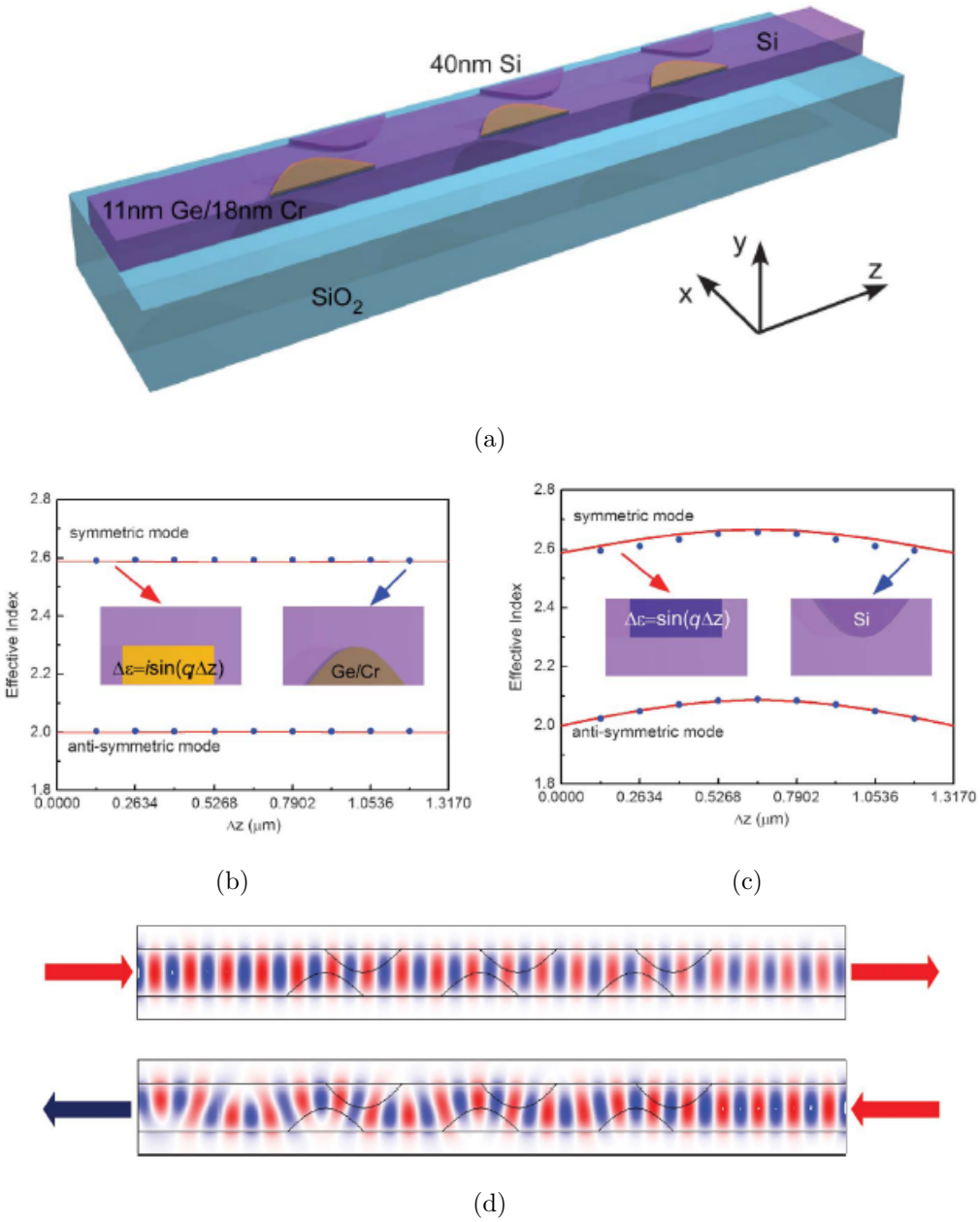

Figure 3.3: (a) Design of the metallic-Si waveguide to mimic the light modulation of PT optical potentials. (b) Effective indices of symmetric and antisymmetric modes with the imaginary part sinusoidal-modulated optical potential (red lines) and the sinusoidal-shaped Ge/Cr bilayer structure (blue dots). (c) Modes effective indices with the real part sinusoidal-modulated optical potential (red lines) and the sinusoidal-shaped Si structure (blue dots). Insets in (b) and (c) show the considered waveguide, and z starts from where modulation begins. (d) Numerical mappings of E_x for forward (upper) and backward (lower) propagation with an incoming symmetric mode.

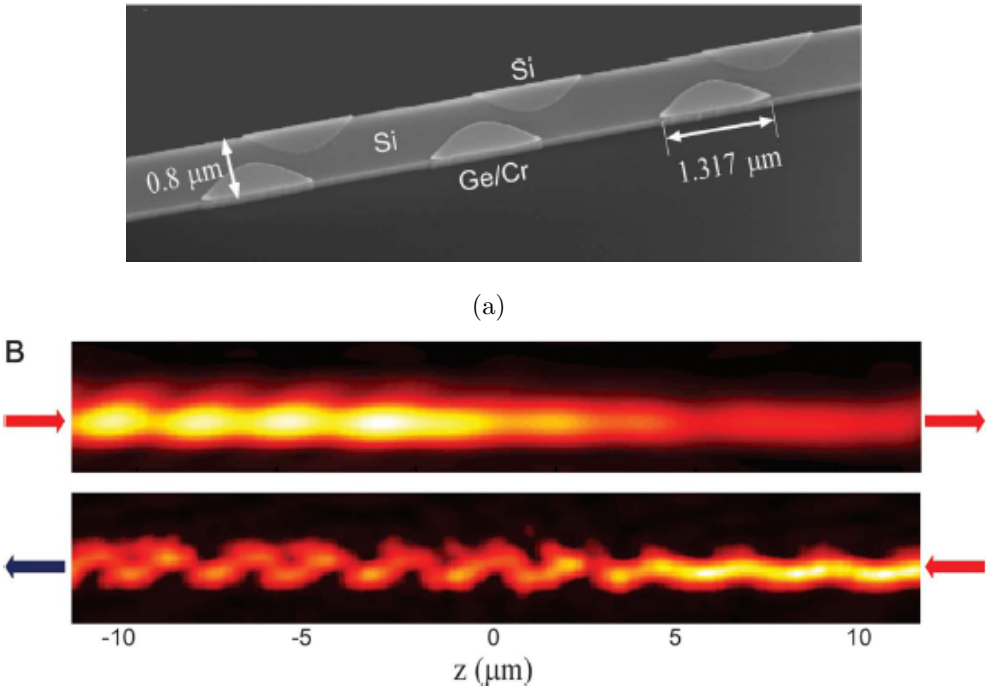

Figure 3.4: (a) Scanning electron microscope image of the fabricated device. (b) Measured near-field amplitude distribution of light in the one-way mode converter for both forward (upper) and backward (lower) light propagation.

classical design to the quantum PT potentials for guided light.

3.4 Experimental Results

A picture of the fabricated device is shown in Fig. 3.4(a). The light propagation in the Si waveguide was observed using the H-NSOM. In experiments, a tapered fiber was used to couple light into the waveguide. Although the fundamental symmetric mode is dominant in incidence, there also exists some power coupled to the antisymmetric mode as shown in Fig. 3.4(b). Consistent with simulations, light remains predominantly the fundamental symmetric mode after propagating through the optical potentials for forward propagation. However, the symmetric-mode-dominant incoming light in backward propagation clearly shows mode conversion to the antisymmetric mode after the device. It is therefore evident

that one-way mode conversion has been successfully realized in CMOS-compatible Si photonics. Although the insertion loss of about 7 dB is observed through the optical potentials, it can be completely compensated by incorporating gain into the imaginary part modulation of the PT optical potentials in (3.1) and eqrefdielectric-modulation. The excited antisymmetric mode can be removed in transmitted fields by implementing, next to the PT optical potentials, an optical mode filter that completely reflects the antisymmetric mode but allows the symmetric mode to transmit. However, it should be noted that the mode conversion efficiency in one direction is equal to the mode attenuation in the other.

We can further confirm the one-way mode conversion effect by taking advantage the phase data collected by the H-NSOM and applying a Fourier transform to look at the modal spectrum. This allows us to examine the behavior of the modes independently as they pass through the device. The center of Fig. 3.5 shows the amplitude A multiplied by the sine of the phase ϕ to obtain a representation of the field $A \sin \phi$. Although this is of course a purely real quantity, it provides some intuition into the complex field behavior.

The proposed one-way system is completely linear and expected to have higher efficiencies and broader operation bandwidths than nonlinear strategies.

The text of this Chapter, in part or in full, is a reprint of the material as it appears in the following journal publication:
Liang Feng, Maurice Ayache, Jingqing Huang, Ye-Long Xu, Ming-Hui Lu, Yan-Feng Chen, Yeshaiahu Fainman, and Axel Scherer. Nonreciprocal light propagation in a silicon photonic circuit. *Science (New York, N.Y.)*, 333(6043):729–33, August 2011

The dissertation author was a primary co-investigator and co-author of this paper. The other authors assisted and supervised the research.

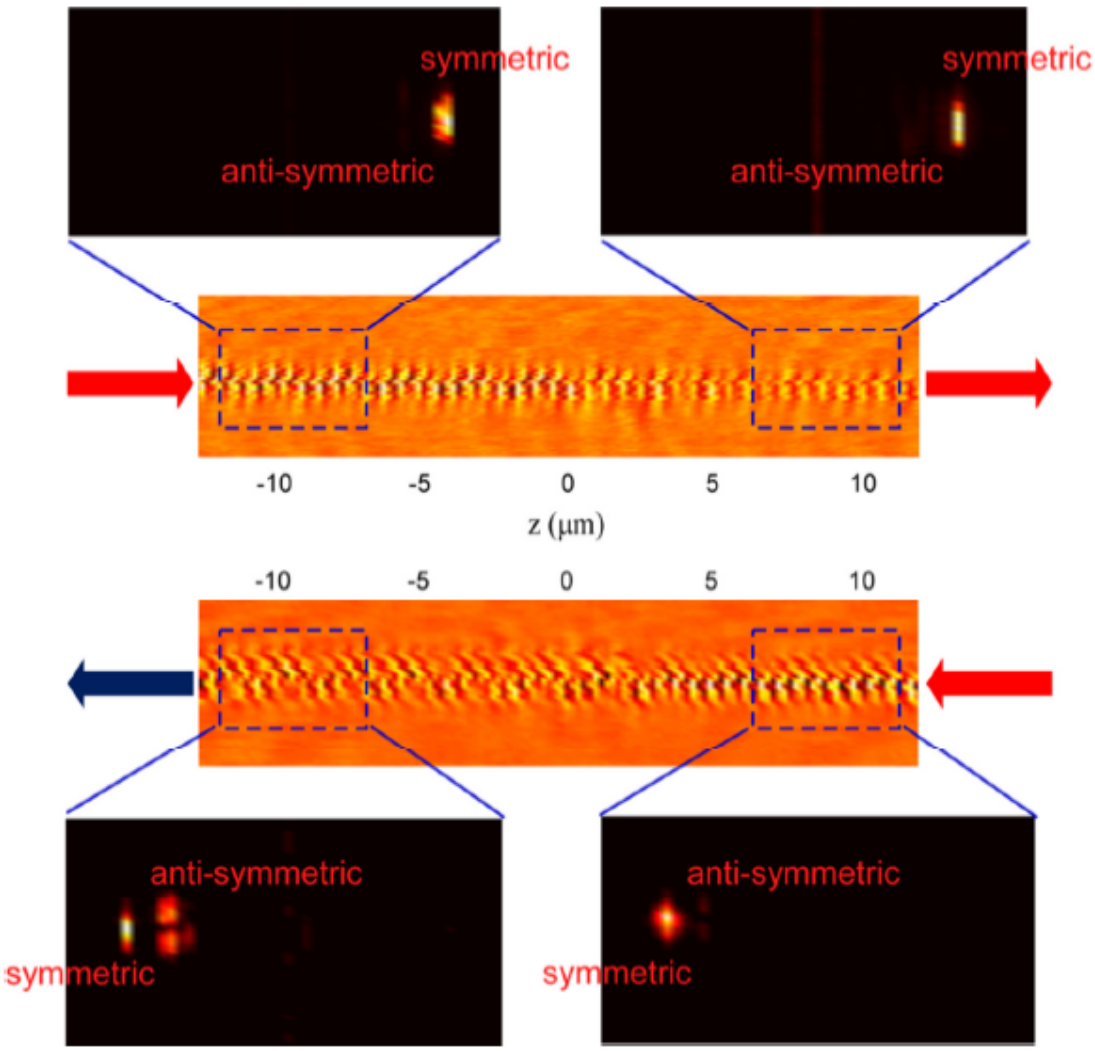

Figure 3.5: Experimental mappings of electric field $A \sin \phi$ for both forward (upper) and backward (lower) propagation, and their corresponding Fourier transforms before and after the device.

Chapter 4

Near-Field Measurement of Amplitude and Phase in Silicon Waveguides with Liquid Cladding

4.1 Introduction

Photonic integrated circuits are typically coated with a solid overcladding to improve symmetry, protect the sample, and allow deposition of successive layers. Near-field characterization of such circuits must be done without the cladding since it prevents the NSOM probe from accessing the evanescent fields at the core-cladding boundary. With no cladding, however, numerous devices lose or change their functionality, making such characterization deviate from the performance of the final device. Here we demonstrate a technique that allows optical near-field characterization of devices while preserving their optical properties. To do so, a liquid cladding is introduced to emulate the actual cladding of the final operational device while allowing the probe to sample the fields at the core-cladding boundary for NSOM analysis. NSOM has previously been applied in a liquid environment for characterization of biological samples [82, 83, 84]. A significant contribution was made by Ji et al. [85] who used the NSOM to measure the intensity profile of a waveguide with a liquid overcladding. However, to date there has been no

heterodyne near-field imaging of a waveguide with a liquid overcladding, which is essential due to the effect of cladding on phase.

In this experiment we measure amplitude and phase of air- and liquid-clad waveguides in the near-field, then use Fourier analysis of the complex field to obtain the effective index difference between them. To the best of our knowledge this is the only H-NSOM technique that allows characterization of complex photonic circuits in their final form, as a part of the fabrication and validation process. As a proof-of-concept, we consider a silicon waveguide, resting on top of a silicon dioxide substrate, with a liquid cladding. Such a configuration serves as a canonical example for many chip-scale device and circuit designs in numerous material systems.

4.2 Liquid NSOM

Characterization of the waveguide is done with a liquid-capable heterodyne near field microscope (H-NSOM) . Rather than the MV-2000 head we used before, here we use a Nanonics MultiView (MV) 1000 (see Fig. 4.1) with a liquid cell module which enables full probe and sample immersion in a liquid environment. This permits simultaneous acquisition of topographic and optical data. The MV-1000 uses the beam-bounce feedback discussed in Subsection 1.1.2, and in this experiment we operate in tapping mode with the beam deflection used to measure the mechanical oscillation of the probe. The sample is mounted in a liquid cell sealed with a rubber gasket. When the liquid is transferred to the bath, it must form a meniscus high enough to immerse not just the sample, but the probe as well. Full immersion of the probe is necessary to prevent it from feeding back on the liquid-air interface, or from the resonance properties changing as the probe enters the liquid. Because of the nature of the feedback system, the head must be based on sample-scanning, as opposed to tip-scanning, to avoid having to scan the entire optical system in tandem with the probe. This makes it impossible to use a static optical fiber for coupling. Instead, in order to preserve alignment during sample motion, the fiber must be rigidly bound to the waveguide. A method for

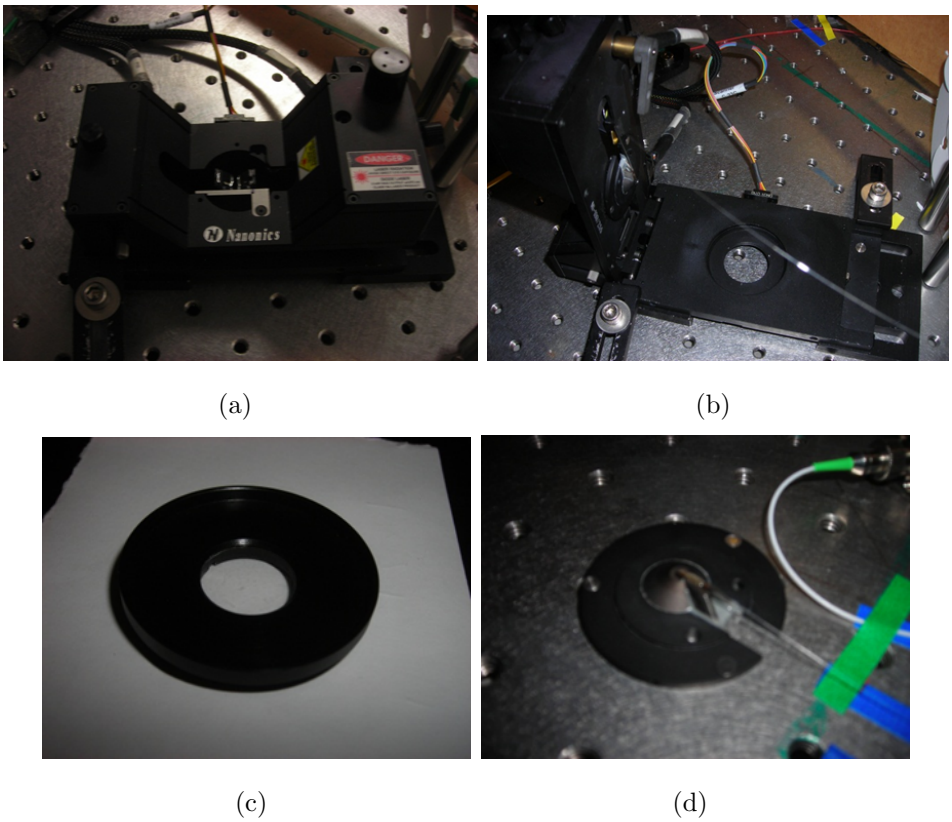

(a) (b)

(c) (d)

Figure 4.1: Nanonics MV-1000 head. (a) Top view of the head. (b) Head while open, with mounted probe fiber exiting to right. During scanning, sample moves underneath fixed tip. (c) Liquid cell module where tip is mounted. The walls of the bath allow full tip and sample immersion in the liquid. (d) Liquid-capable probe mount. Conical shape allows damping of probe induced oscillation in the liquid.

doing so will be detailed later.

The presence of the liquid causes a number of mechanical and optical effects which influence the mechanical performance of the probe, chief among them damping and noise. The effects of damping may be understood by considering the probe as a standard mechanical resonator in the "mass on a spring" model. This model is described by the differential equation:

$$\frac{d^2x}{dt^2} + \frac{\gamma}{m}\frac{dx}{dt} + \frac{k}{m}x - F = 0. \tag{4.1}$$

Here $x = x_0 e^{i\omega t}$ is the probe position describing oscillation at frequency ω, $F = F_0 e^{i\omega t}$ is the applied oscillation force, γ is the damping due to the liquid, k is the probe spring constant, and m is the probe mass. By defining ω_0 as the undamped resonance frequency of the probe, we can solve for its frequency response:

$$x_0 = \frac{1}{m}\frac{F_0}{(\omega^2 - \omega_0^2) - i\gamma\omega} \tag{4.2}$$

The damping γ broadens the resonance, to a width of 2γ, and brings down its peak value by a factor of γ. This causes the probe to oscillate less strongly at its peak frequency, as well as to be less responsive to changes in the resonance due to contact. Thus the gain must be increased which may have the effect of increasing unwanted oscillation. Because of the slowed response of the probe in the liquid, the damping also causes the resonant frequency to drop to $\sqrt{\omega_0^2 - 2\gamma^2}$. The liquid also introduces unwanted noise due to its stronger ability to conduct mechanical waves as a result of its higher density as compared to air. As a result, many new mechanical resonances are introduced due to the multiple interactions between the probe and the environment through the liquid. The liquid can also conduct waves induced by the probe oscillation itself through the bath and back to the probe. The probe mount for the MV-1000, as seen in Fig. 4.1(d), thus has a partial cone shape designed to damp these oscillations. However, one must be careful to select the correct the correct resonance based on the strength of the probe response, the resonance width, and its freqency relative to the probe frequency in air.

The optical properties of the liquid also come into play for detection of the mechanical oscillation. The laser that is reflected off of the top of the probe must now pass through the liquid. The beam strikes the first mirror and is reflected

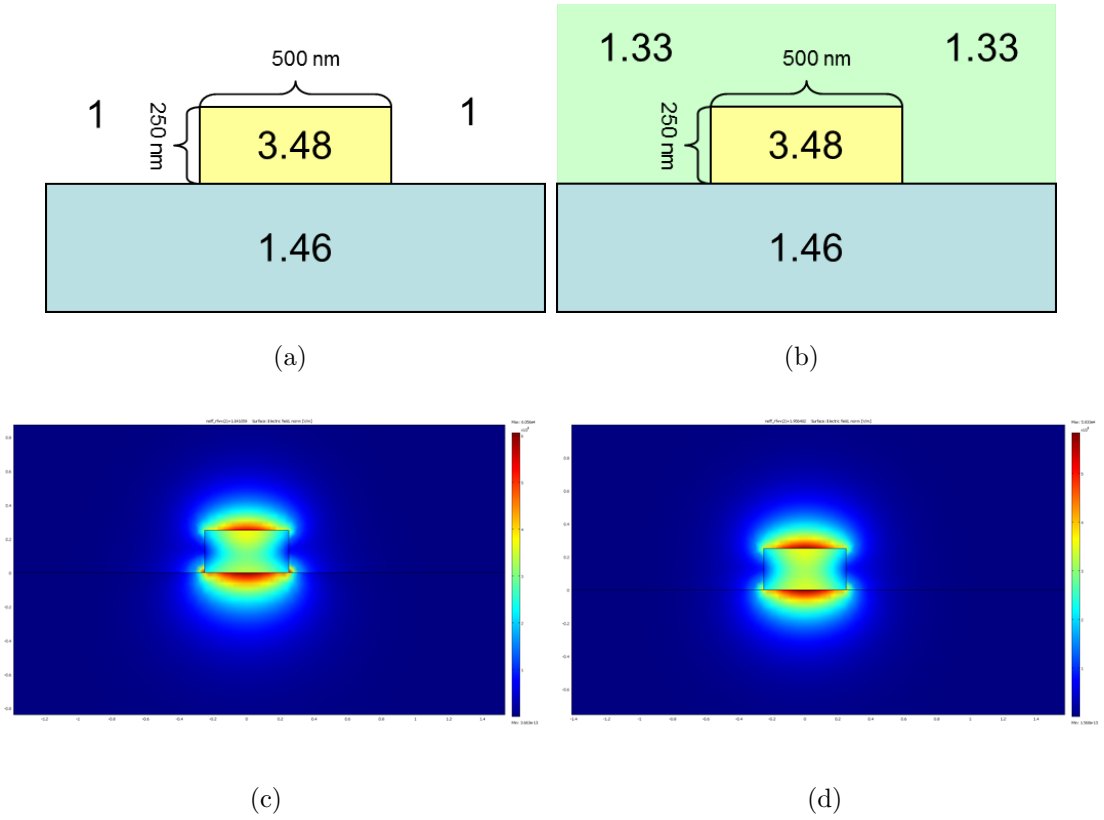

Figure 4.2: Top figures show the designed refractive index distribution of the waveguide in cross-section for both (a) air and (b) water overcladding. Bottom figures show the electric field distributions, calculated by finite element analysis, of the quasi-TM mode for the corresponding overcladdings ((c) air and (d) water). This mode has a large vertical penetration depth, permitting the NSOM probe access to a significant portion of the optical power.

down through the window and into the liquid. At this point there is a Fresnel reflection due to the index mismatch between the glass of the window and the liquid. However, this reflection is smaller than in air, so the loss due to reflection is reduced. The same phenomenon occurs as the beam exits the bath through the window. However, there is an increased loss in the beam due to absorption and scattering in the liquid. Furthermore, the beam must be focused onto the probe in air, so introducing the liquid causes a small defocusing effect, once again reducing the optical power reflected from the probe onto the second mirror and eventually onto the PSD. In practice, the sum of all these effects causes less optical signal to be reflected onto the PSD, necessitating a higher gain of the photodetector signal.

4.3 Sample Design and Fabrication

The sample, as designed, is a 500 nm wide by 250 nm tall silicon (n = 3.48) channel on top of a SiO_2 (n = 1.46) substrate. The designed cross-sections are displayed with their refractive index distributions, for both air (n = 1) and water (n = 1.33) overcladdings in Fig. 4.2(a) and (b). In order to estimate the results of the experiment, we numerically simulate this structure in cross-section according to the design parameters with commercial finite element software (COMSOL Multiphysics RF module). The simulation returns the field distribution as well as the effective index of the hybrid quasi-TM mode of the designed structure, for both air and water overcladdings. The results of the simulation are shown in Fig. 4.2. Although the field is predominantly localized in the silicon core, the distribution of the quasi-TM mode demonstrates low confinement in the vertical direction, making it favorable to NSOM characterization. The simulation returns the effective index for both cases, defined as

$$n_{eff} = \frac{k}{k_0}, \tag{4.3}$$

for a field propagating in the x direction as

$$E(x, y, z) = f(y, z)exp^{i(kx-\omega t)}. \tag{4.4}$$

The simulation gives n_{eff} = 1.84 for air overcladding, and n_{eff} = 1.95 for water overcladding. This constitutes a shift of .11 for the silicon waveguide.

Water is optically lossy in the near-infrared wavelength regime, and we can learn the effect of this absorption by including its complex refractive index in the simulation. The imaginary part of the refractive index is $k = 9.86\times10^{-5}$ [86], which corresponds to a loss of 3.47 dB/mm for propagation completely through water. Using the complex refractive index, the simulation returns $n_{eff} = 1.95+3.92\times10^{-5}$. This gives a loss of 1.38 dB/mm. For a longitudinal scan range of 25 µm, this is a loss of 1.38 dB, or 1%. The region of interest also sits approximately 2 mm from the chip entrance, which means there will be about 6.94 dB of loss due to absporption during propagation from the beginning of the waveguide to the tip location. This is a loss of 48%. In particular, one would expect approximately

twice the SNR for the air-clad waveguide as for the water-clad for the same-size tip.

The fabrication process is diagrammed step-by-step in Fig. 4.3. HSQ (hydrogen silesquioxane) resist is deposited on a standard silicon-on-insulator wafer, then patterned by electron beam-lithography and developed. The silicon is then etched using a reactive ion etching with the waveguides being protected by the HSQ mask, which is then removed by a 30 s soak in 1:10 Buffered Oxide Etch (BOE) solution. Each waveguide is comprised of a 500 nm wide by 250 nm tall silicon channel on top of a silicon dioxide substrate buried oxide layer. The pattern produced after etching is a set of these waveguides with a 90 bend, with a taper at each end. The wafer is then spin-coated with NR-9 resist to protect it during singulation. In order to form a single chip with the waveguide coming to both ends, we singulate the wafer by a special dicing process. Cuts are partially diced into each wafer at the input end, leaving a 500-µmgap around of the set of tapers. The wafer is then cleaved along an edge defined by these cuts, forming a clean break which is relatively smooth due to its orientation along the silicon crystal axis. It should be noted that this break may occur anywhere within the width of the cut ($\sim$ 70µm), but most likely occurs at the center of the cut; the taper is designed to take this effect into account. A full dice is performed across the output end since minimizing scattering is not critical there. The NR-9 is then removed with acetone.

In order to accomodate the fiber-chip bonding process and improve fiber-waveguide coupling, the waveguides have tapers [87] at either end. Below a critical width, reducing the width of a waveguide begins to force the mode outside of the core and into the cladding, and in fact increases the mode field diameter (MFD) as the waveguide width is reduced. The mode cross-section of such a narrow waveguide is shown in Fig. 4.4(b). This can be used to adiabatically couple light from a high-mode field diameter (MFD) structure such as a fiber to a low-MFD structure such as a silicon waveguide. In such a coupler, the width of the waveguide tapers parabolically from the full 500 nm width, to a minimum width on the order of 100 nm. A 2-d model of the propagation through the taper is shown in Fig.

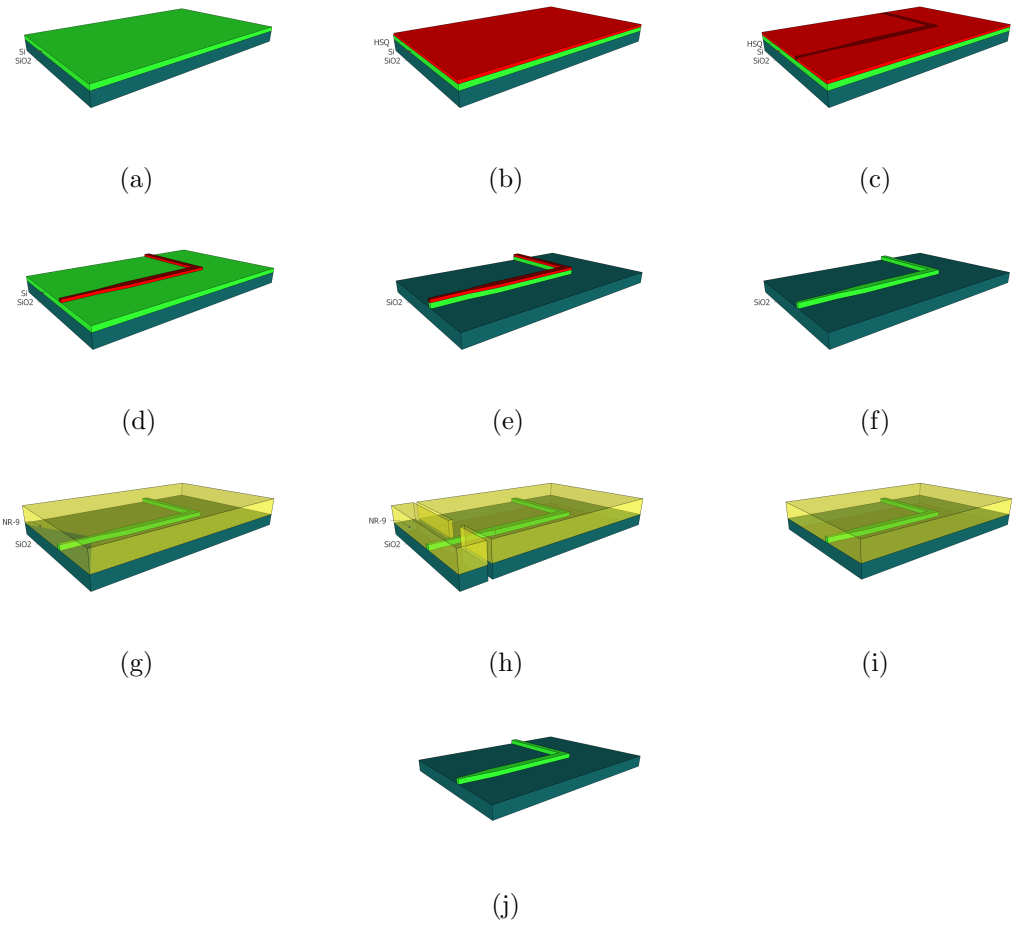

Figure 4.3: Fabrication process for silicon waveguides. (a) SOI wafer. (b) Spin-coat HSQ resist. (c) Expose HSQ by e-beam lithography. (d) Develop resist. (e) Reactive ion etching of Si. (f) Resist removal with 1:10 BOE solution. (g) Spin-coat protective NR-9 layer. (h) Partial dicing. (i) Cleave between dicing cuts to create smooth edge at taper. (j) Remove NR-9 with acetone

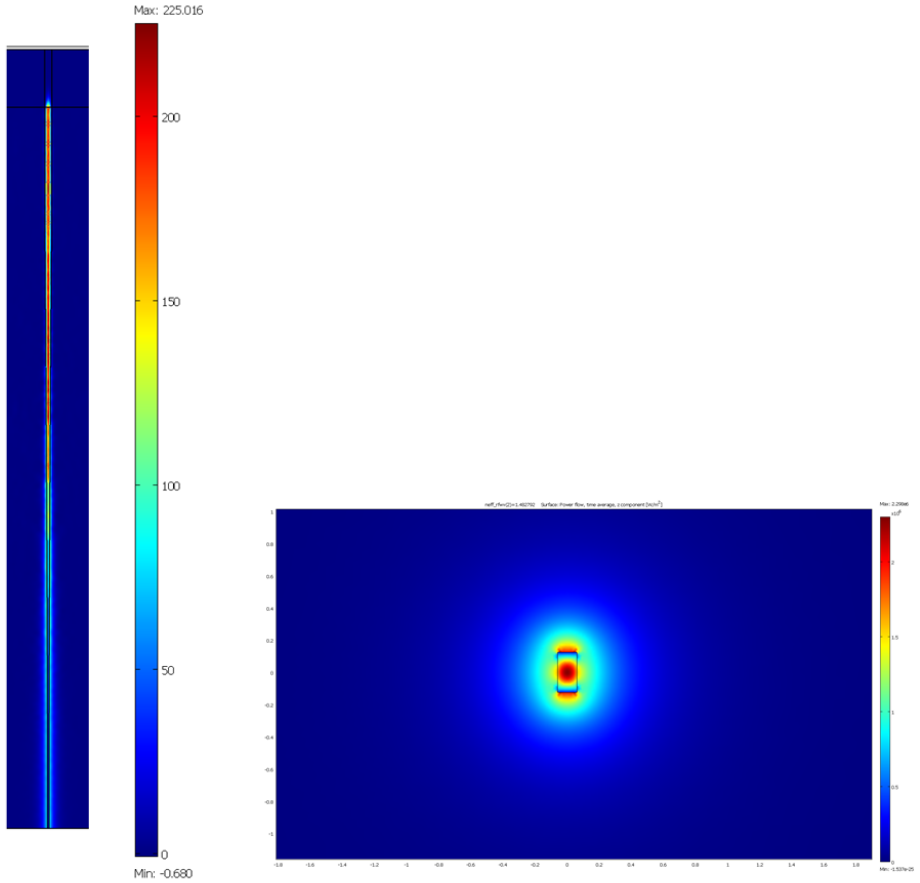

(a) (b)

(c)

Figure 4.4: Taper to adiabatically couple light from high-MFD fiber to low-MFD waveguide. (a) In-plane overview of mode propagation in taper. Notice mode is deconfined in narrow section of taper, then almost totally contained in full-width section. (b) Cross-section of low-confinement mode distribution in narrow section of taper. (c) Optimization plot for taper width for both TE and TM illumination from an optical fiber of MFD=4.8 µm. Taken from [87]

4.4(a). As the waveguide expands, the mode becomes increasingly confined in the waveguide core. Because of the low-confinement nature of the taper mode, the refractive indices of the undercladding and overcladding must be well-matched in order to sustain the mode. In this case, the epoxy for fiber bonding serves as the overcladding. Although the waveguide width can be optimized to match the fiber mode through simulation, as shown in Fig. 4.4(c), in practice due to inexact knowledge of the cladding dispersion it is necessary to fabricate a number of tapers and maximize the coupling expeirmentally. It was found that maximum fiber-waveguide coupling is obtained when the waveguide tapers to 135 nm.

Since the field mostly occupies the low-index cladding, the modal effective index is quite low (1.48 for a 135 nm taper), which reduces Fresnel reflection at the chip edge due to effective index mismatch with free space. For this reason, there is also a taper on the output end of the waveguide, which minimizes backreflection into the waveguide in order to prevent standing waves from appearing in the NSOM image. The expected reflection can be calclulated according to the Fresnel equation for normal incidence:

$$R = \left(\frac{n_2 - n_1}{n_2 + n_1}\right)^2 \tag{4.5}$$

Using $n_1 = n_{eff}$, and substituting in the values for n_{eff}found previously through simulation, we estimate a backreflection of 3.5% in air and .3% in water, calculated on an intensity basis, with the output taper. Without the output taper, we would expect 8.7% reflection in air 3.6% in water.

Since the MV-1000 scans the sample underneath the tip, the fiber must be bonded to the chip. The chip is mounted in a fiber-based transmission setup, where its output is imaged through two 4f setups onto a camera (see Fig. 4.5). A single-mode polarization-maintaining fiber is aligned to the waveguide by maximizing the transmission as measured by the camera. The fiber is oriented with the electric field vertical to the chip plane in order to excite the quasi-TM waveguide mode, which is favorable to NSOM characterization due to its long vertical evanescent decay. When the the fiber is aligned, it is bonded to the tapered waveguide end with low-shrinkage UV-cured epoxy (Dymax OP-20), as shown in Fig. 4.6. The fiber is then bonded to the slide on which the chip sits using low-shrinkage epoxy (OP-

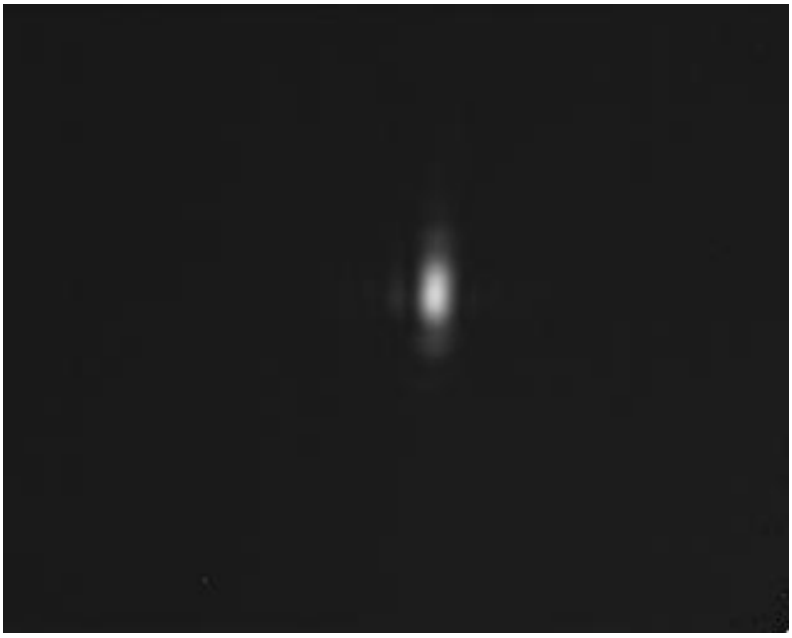

Figure 4.5: Image of quasi-TM mode as captured by infrared camera through two 4f systems.

4-20632-GEL). This forms an integrated package with high mechanical stability.

4.4 Experimental Measurement

4.4.1 Phase Drift

This is a phase-sensitive measurement, so minimizing phase aberrations is critical, in particular due to the quantitative nature of the desired results. The key effect to be concerned about is phase drift due to thermal variation among the fibers, which has previously been observed in [88]. At room temperature, the silicon dioxide has a thermal expansion coefficient $\alpha = 5.5 \times 10^{-}7^{\circ}\mathrm{C}^{-1}$. For the 10 m of fiber in each arm of the heterodyne interferometer, we apply the thermal expansion formula:

$$\frac{\Delta L}{L} = \alpha \Delta T, \tag{4.6}$$

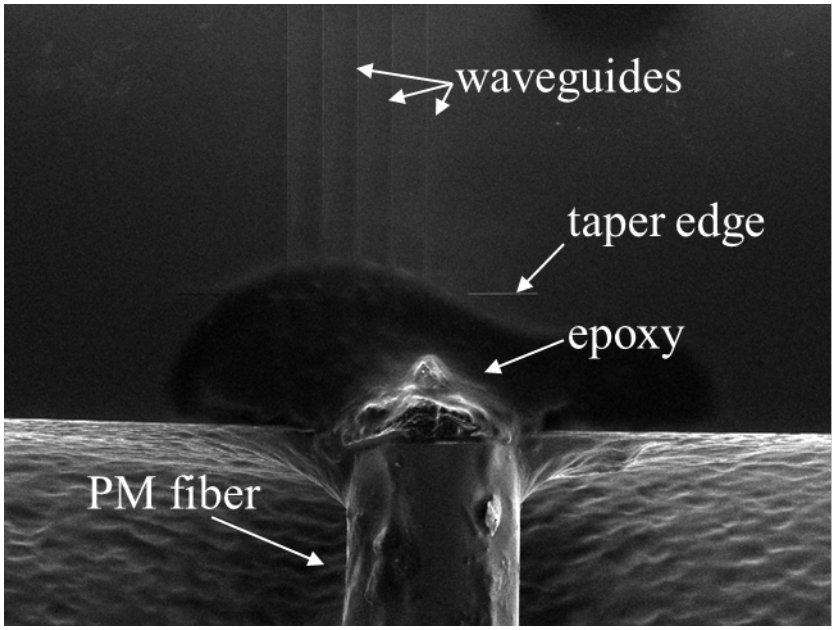

Figure 4.6: Scanning electron micrograph of PM fiber bonded to silicon waveguide. Epoxy forms overcladding for tapers

which can be rearranged to:

$$\frac{\Delta L}{\Delta T} = \alpha L, \tag{4.7}$$

to find a thermal expansion of 5500 nm for each °C change in the fiber temperature. A relative change in length ΔL of the fiber in the two arms induces a phase change $\Delta\phi = \beta\Delta L$, with $\beta = \frac{2\pi n}{\lambda_0}$ (for single mode fiber $n \sim n_{eff}$ due to low core-cladding index contrast). Thus we have:

$$\frac{\Delta\phi}{\Delta T} = \frac{2\pi n\alpha L}{\lambda_0}. \tag{4.8}$$

For $n = 1.46$ and $\lambda_0 = 1550nm$, (4.8) implies that it only takes a change of .03°C in the temperature difference between the two arms to change the interferometer phase byπ.

We determine the degree of phase drift present in the system by tracking the phase recorded by the lock-in at a single location of the tip over time. With the heterodyne system uncovered, the phase is recorded at a single point of the waveguide for 150 s. The lock-in returns phases between 0 and 2π, so the phase is unwrapped before plotting. The plot of $\phi(t)$ is given in Fig. 4.7(a). There is a

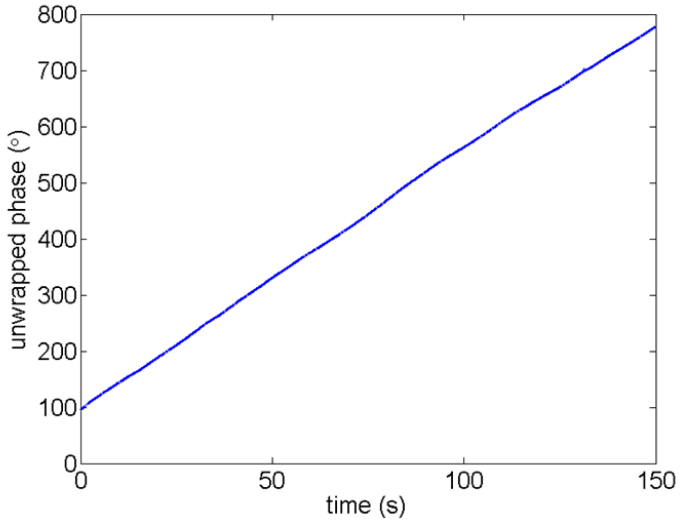

(a)

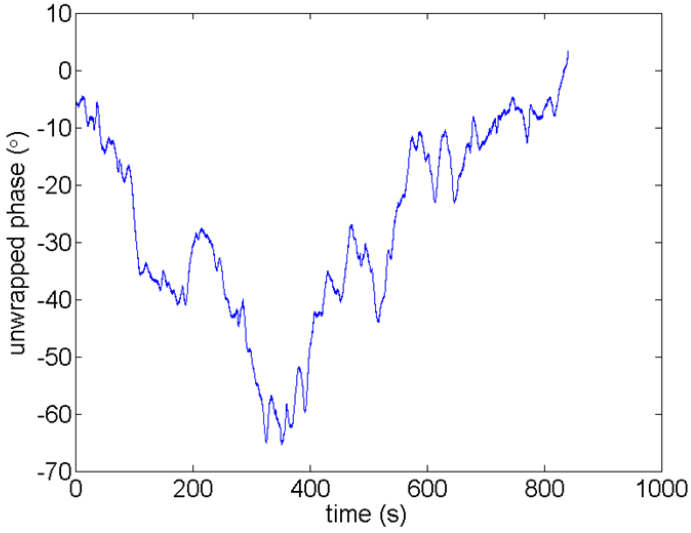

(b)

Figure 4.7: Variation in phase over time $\phi(t)$ as recorded by the lock-in for a single position of the tip. (a) Heterodyne system uncovered. (b) Heterodyne system covered with an acrylic box.

clear linear drift observable in the data, at a rate of 4.7°/s. The drift is caused by thermal gradients and air currents present in the room, likely tied to the HVAC system. This linear drift is problematic for a quantitative measurement for the following reason. Under a phase drift $\phi_d(t) = at$, the NSOM will record a phase

$$\phi = \phi_s(x, y) - \phi_r + at. \tag{4.9}$$

For a scan in the x direction at a rate $v = x/t$ of a waveguide with propagation constant k, this becomes

$$\phi(x, y) = (k + a/v)x - \phi_r. \tag{4.10}$$

Thus a linear drift in the phase corresponds to a constant shift a/v in the measured frequency (and consequently in the Fourier transform), necessitating a substantial reduction in its severity.

The heterodyne system is then covered with an acrylic box and allowed to sit for several hours for the thermal gradients within the box to settle. The drift is re-recorded for about 15 minutes (approximately the length of time required for one typical NSOM scan), with the results shown in Fig. 4.7(b). With the box covered, we observe a stochastic drift with a random-walk appearance. The full range of variation is less than 70°over the 15 minute span, and not in a consistent direction. Each measured point effectively has a small random phase in addition to the true phase. In frequency space, this corresponds to a widening of the Fourier transform, due to the distribution of phase jitter causing a larger distribution of frequencies to be present.

4.4.2 Measurement and Results

With the fiber-connectorized waveguide is mounted in the liquid cell in the MV-1000 head, we measured at $\lambda_0 = 1550$ nm wavelength with the H-NSOM using a 200-nm metal-coated aperture probe, with overcladdings of air and water. The waveguide is raster-scanned beneath the probe, with the fast (x) axis 25 m long, parallel in the 128 x 128 point grid. The results of the experiment for air and water overcladding are shown in Fig. 4.8. In addition to the raw topography, amplitude

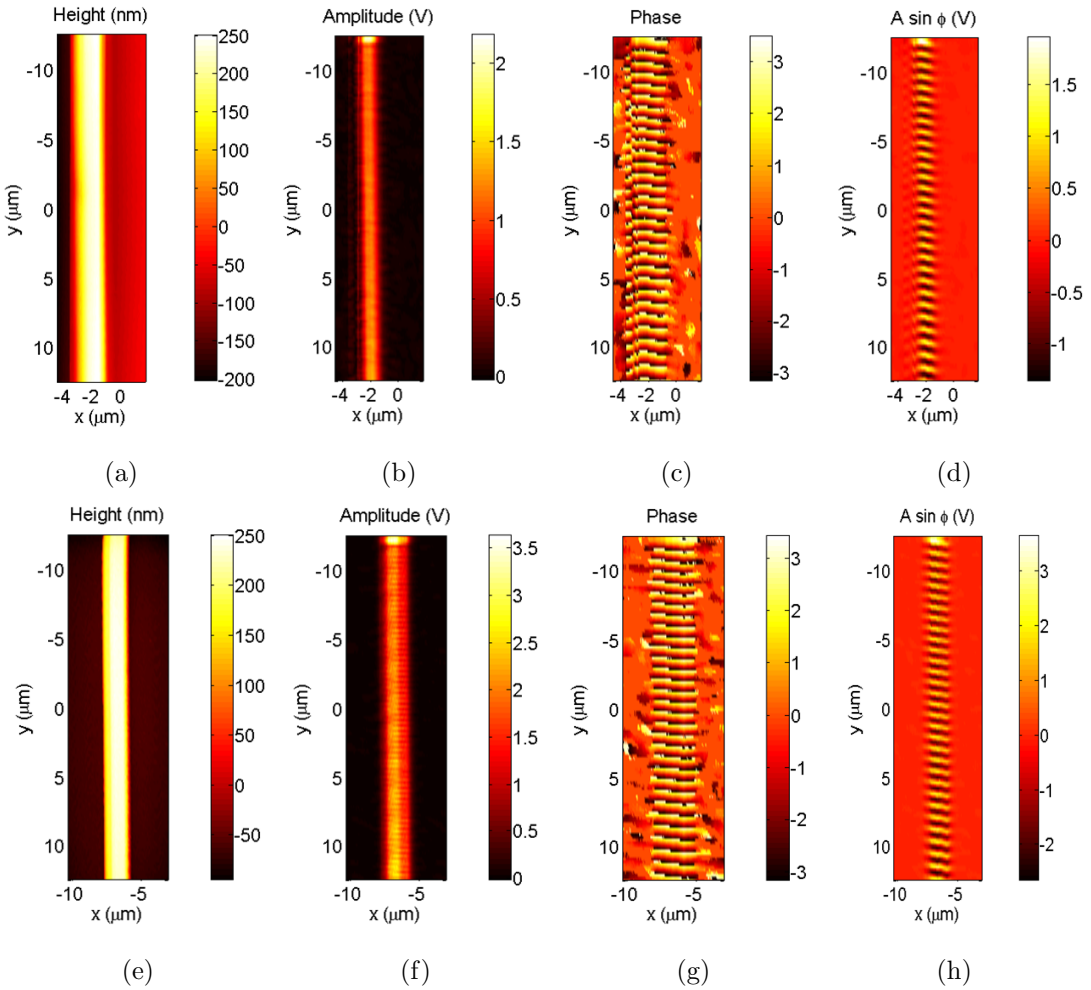

Figure 4.8: Silicon waveguide NSOM results in (a-d) air and (e-g) water overcladding. (a,e) Topography. (b,f) Optical amplitude A. (c,g) Optical phase ϕ. (d,h) $A \sin \phi$, the imaginary part of the complex electric field.

A and phase ϕ, we also show the calculated $A\sin\phi$, which is the imaginary part of the complex electric field propagating along the waveguide, i.e. the optical field distribution at a particular time. Despite the presence of the water, the measured waveguide height matches closely to the design, and the overall profile is similar to that recorded without any water. The amplitude plot displays a weak modulation due to reflection of the mode at the waveguide output, which will be addressed in Section 4.5.

4.5 Fourier analysis

To evaluate quantitatively the effect of the water, Fourier analysis is applied to each set of amplitude and phase maps. For amplitude A and phase ϕ, using the Fast Fourier Transform (FFT) along the x-axis on Fig. 4.8, we calculate the estimated power spectral density $|\mathcal{F}_x(Ae^{i\phi})|^2$, where x is the direction of propagation. The frequency axis is given by $n_{eff} = k\lambda_0$, where k is the FFT spatial frequency coordinate, which gives the phase spatial frequency or propagation constant. The square magnitude corresponds to the power spectrum of the propagating modes. By only taking the Fourier transform along one direction, we preserve the information about the transverse distribution of the modes. To obtain the effective indices, we can then integrate along the transverse (y) coordinate.

As an initial example, Fig. 4.9 shows the raw integrated Fourier spectrum without any preprocessing, calculated according to:

$$\int |\mathcal{F}_x(Ae^{i\phi})|^2 dy \tag{4.11}$$

For both air and water claddings, we see a spectrum with two peaks; one at an effective index close to the simulation value, and one at a lower effective index. A number of hypotheses fail to account for this extra peak. These include birefringence of TE and TM modes, phase drift, and angle of the waveguide relative to the scan. In fact, the extra peak seems to be an artifact of spectral leakage [89], which is the formation of spurious peaks due to phase discontinuities at the two ends of a scan. The phase discontinuity arises from the fact that the scan resolution is not an integral multiple of the signal wavelength, and effectively corresponds to an

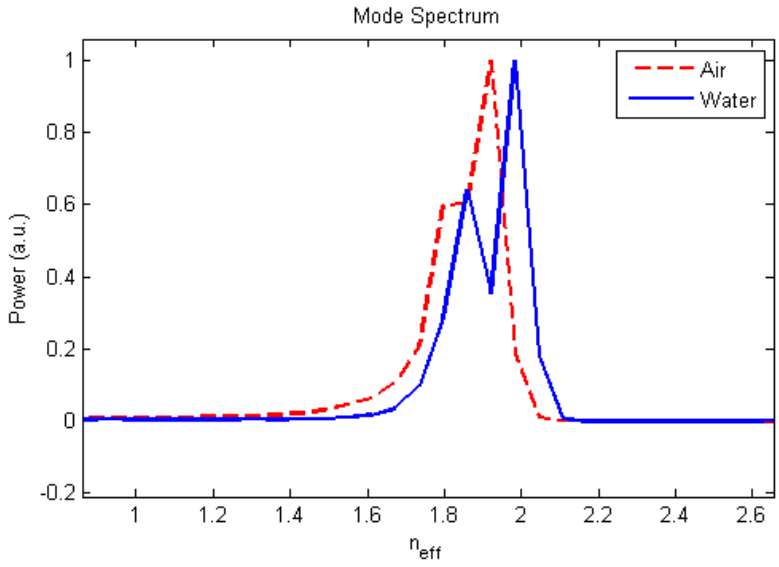

Figure 4.9: Raw integrated Fourier data for both air and water claddings. The peak power has been normalized to 1 for readability. Note the double peaks on each curve due to spectral leakage.

extra frequency introduced in the signal. The extra peak only occurs on one side of the real peak due to the complex nature of the field used for the transform.

An alternative method is to remove lines from the end of the scan to attempt to equalize the phase, then take the Fourier transform. We remove one line from the scan for air overcladding, and two from the scan for water overcladding. The results of this method are shown in Fig. 4.10, with the peak power arbitrarily scaled to 1 to improve readability. Although the extra peak is not apparent, the spectrum appears to have an asymmetric tail. In fact, this tail is the remnant of the suppressed peak. Each scan line represents a given amount of phase, so it is not necessarily possible to equalize the phase exactly, if the line does not correspond to an integer multiple of the difference between the phases at the beginning and end. If we continue to remove lines, the peak periodically disappears, and reappears, lending strong credence to the phase discontinuity hypothesis. A Gaussian fit is applied to the two spectra. In each case the fit has $R^2 > 95\%$ and measures the effective index with a tolerance of $\pm.005$.

To improve further, rather than removing scanlines, we can apply a window function $w(x)$ before performing the Fourier transform. Specifically we apply the

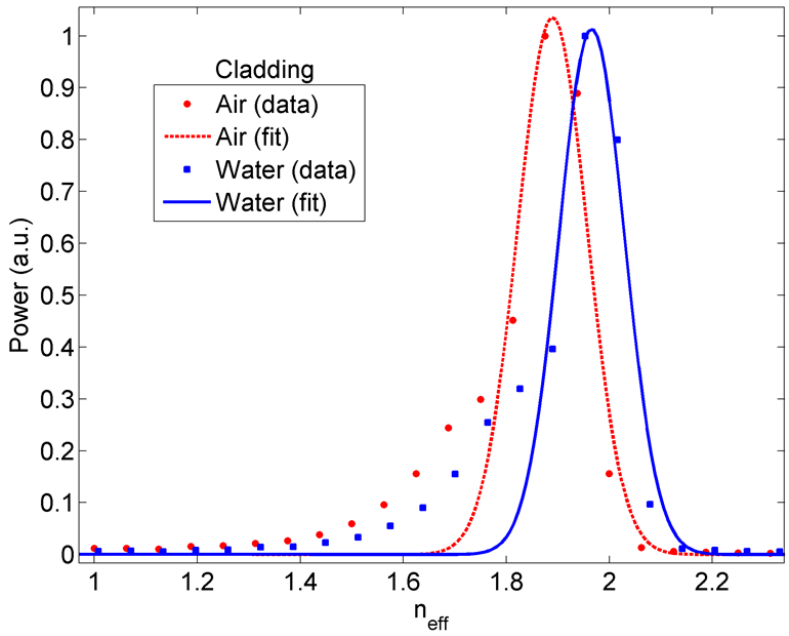

Figure 4.10: Integrated Fourier transform of the complex field with scan lines removed (1 for air overcladding, 2 for water overcladding) to reduce spectral leakage. This leaves a low-index tail visible which is the remnant of the suppressed peak.

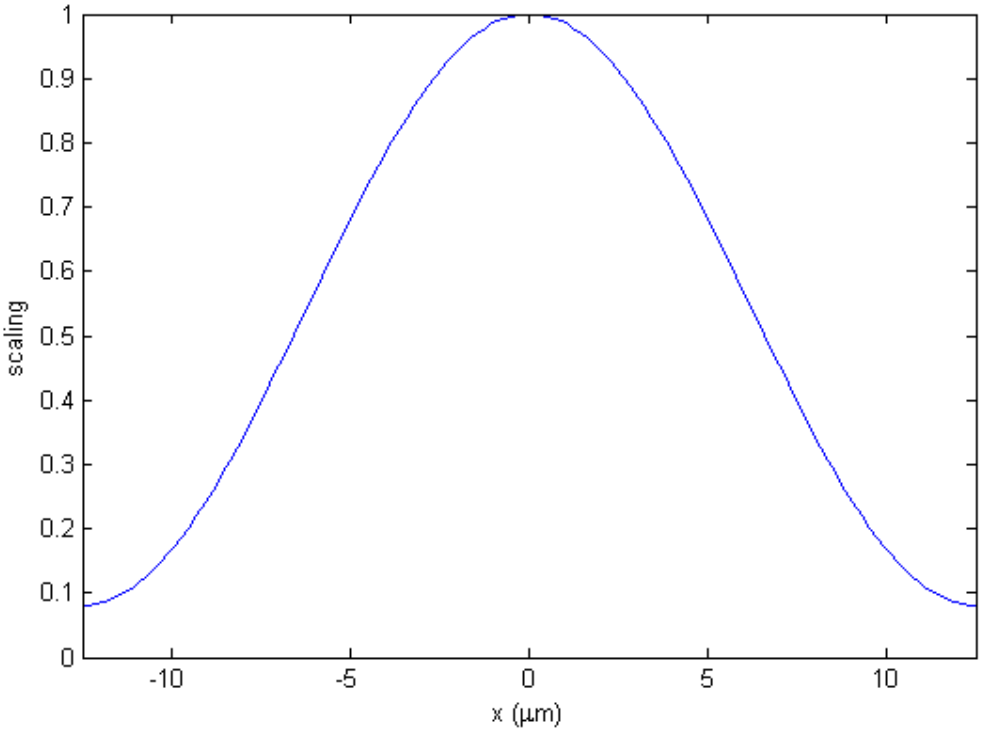

Figure 4.11: The Hamming window function given by (4.12). The Hamming function reduces the influence of the edges on the Fourier transform.

Hamming window [90], defined for a set of points n by:

$$w(n) = .54 - .46\cos\left(2\pi\frac{n}{N}\right), \tag{4.12}$$

where N is the number of points in the domain. Although the function is typically defined for a set of points on a discrete domain, we may easily redefine it for the real-space variable x by taking $n = x$ and setting N to the length of space sampled, provided it is centered at 0. It is clear from examining the plot of (4.12) shown in Fig. 4.11 that the effect of the Hamming window is to weight the center of the image while discounting the edges, in order to suppress the phase discontinuities at the edges.

After calculating $|\mathcal{F}_x\{w(x)A(x,y)e^{i\phi(x,y)}\}|^2$ and plotting the results in Fig. 4.12(c) we can see that the symmetry of the peak is greatly improved. The Gaussian fit has $R^2 > 98\%$, demonstrating the effectiveness of this model. Fig. 4.12 (a) and (b) show the square magnitude of the power spectral density (without

integration) in the x direction for air and water claddings, respectively. The horizontal coordinate gives the effective index, which increases as the cladding index is increased. The shape of the single TM mode is visible along the y-axis (perpendicular to the guide), with a peak in the middle that decays evanescently to the sides.

By integrating the estimated power spectral density (PSD) along the y-axis, as shown in Fig. 4.12, and fitting it to a Gaussian distribution, we obtain the effective index at the peak of this Gaussian fit. With an air overcladding, the effective refractive index obtained by analyzing the experimental data is $1.881 \pm .002$, close to the value of 1.84 obtained from the simulation. With a water overcladding, the index estimated from the experimental data is $1.96 \pm .002$, also close to the value of 1.95 predicted by the simulation. The precision is quite high due to the high SNR enabled by the heterodyne setup and integration over the waveguide width; the accuracy, which determines the difference between the simulation and the experiment, is primarily affected by phase drift and mechanical stability. The addition of the water causes a measured effective index shift of .08, 4%. This corresponds to a π phase difference over 10 µm, less than characteristic lengths of typical silicon photonic devices, making an accurate cladding essential to preserve the phase properties of the device.

It was previously noted that the amplitude displays a standing wave pattern typically associated with reflections at the output facet. Measured crest-to-crest directly on the amplitude image, the wavelength of this modulation is approximately 419 nm. One expects the the wavelength of a standing wave will be half that of the traveling wave that generated it. The wavelength of the traveling wave, as measured in the phase signal, is $\frac{\lambda}{n_{eff}} = 791$ nm, approximately twice the value measured in the amplitude data. The use of the complex phase in the Fourier transform allows the separation of positive and negative frequencies. Fig. 4.13 shows the integrated Fourier spectrum (raw data) in the neighborhood of the negative effective index previously calculated. There we observe a weak backpropagating mode at the expected effective index. By comparing to the power in the fowardpropagting mode, we determine that the reflection at the output is less than 1% by

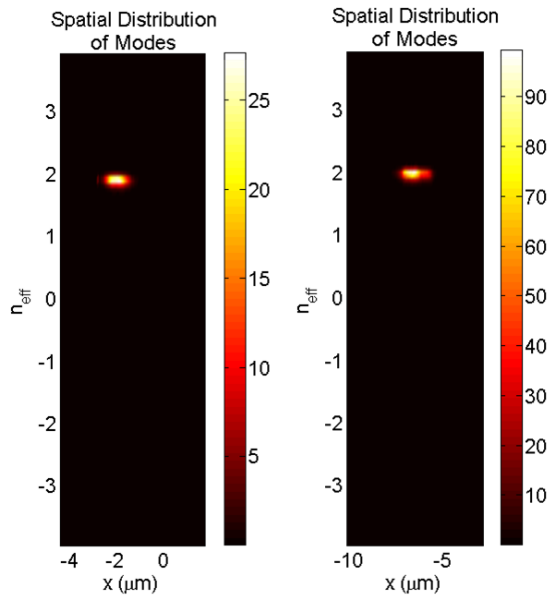

(a) (b)

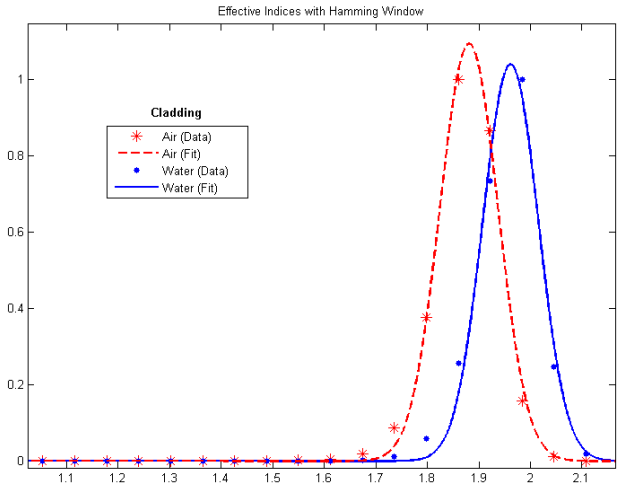

(c)

Figure 4.12: Fourier transform of the complex field data with Hamming window applied. The effective distribution of each modal peak is now highly symmetrical, due to the window de-weighting the phase-discontinuous edges in the plot. (a,b) Estimated power spectral density for both (a) air and (b) water, showing a single mode in each case. (c) y-integrated data from (a) and (b), demonstrating an effective index shift of 0.08 from air to water cladding.

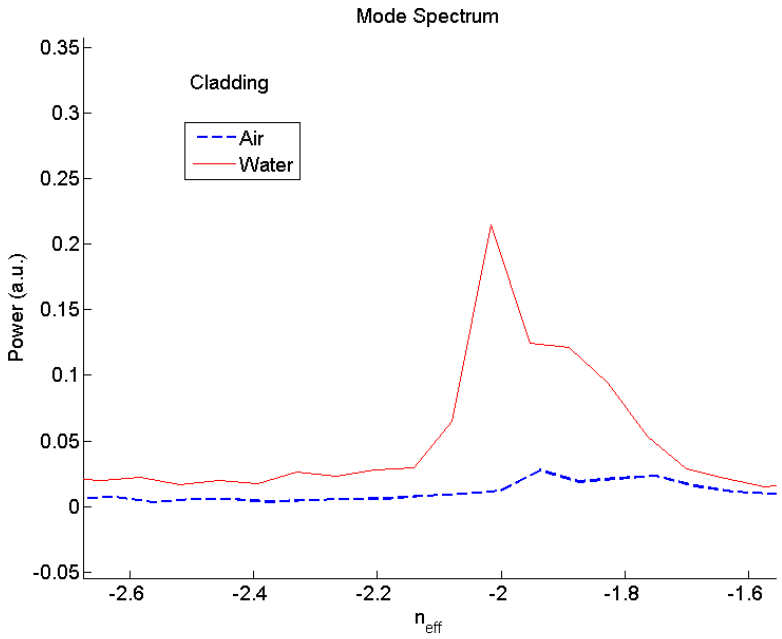

Figure 4.13: Backward-propagating mode due to Fresnel reflection (¡1% intensity). Applying the Fourier transform to the complex field allows separation of negative and positive frequencies.

intensity. This is close to the .3% predicted by theory in Section 4.3. The reason for this small disparity is not clear.

In summary, we demonstrated a technique of liquid-based heterodyne near-field characterization of photonic devices and circuits. As a proof-of-concept, we measured the full complex field (amplitude and phase) of the guided quasi-TM mode in a waveguide with air and water overcladdings. Using Fourier analysis of the measured fields we obtained the effective indices of the guided modes, which are in good agreement with the results obtained from numerical simulations. This technique opens up a number of new possibilities, including using H-NSOM as a part of photonic circuit validation during and after the fabrication process. Availability of liquids with refractive indices varying from 1.3 to 1.8 allows emulation of most solid dielectrics commonly used as a cladding. For structures with SiO_2 undercladding, using index-matching liquid at n=1.46 to create a symmetric environment would be useful in measurement of losses, as well as characterization of low-confinement fields such as those associated with tapers and higher-order

modes. Additionally, aqueous solutions would be useful for high-resolution phase-contrast imaging of biological molecules and live cells.

The text of this Chapter, in part or in full, is a reprint of the material as it appears in the following journal publication:
Maurice Ayache, Maziar P. Nezhad, Steve Zamek, Maxim Abashin, and Yeshaiahu Fainman. Near-field measurement of amplitude and phase in silicon waveguides with liquid cladding. *Optics Letters*, 36(10):1869, May 2011 The dissertation author was the primary investigator and author of this paper. The other authors assisted and supervised the research.

Chapter 5

Direct Imaging of Long-Range Surface Plasmons

5.1 Introduction to LRSP

Surface plasmon polaritons (often referred to as surface plasmons or SPPs) are waves that form at the interface between a metal and a dielectric. The SPP consists of an electromagnetic field coupled to coherent oscillations of the "sea of electrons" in the metal. Because of the metal's complex refractive index, SPPs peak at the interface and decay in the direction normal to it, while propagating along the interface. For similar reasons, their effective wavelength can be substantially lower than the vacuum wavelength, confining light well below the classical diffraction limit. SPPs have been applied

To understand the electromagnetic origin of SPPs, we consider an interface between a metal and a dielectric in two dimensions. The interface occurs at $z = 0$ and extends infinitely in both the x and $-x$ directions. The dielectric has a purely real dielectric constant ε_d, while the metal has a complex dielectric constant $\varepsilon_m = \varepsilon_{mr} + \varepsilon_{mi}$, where $\varepsilon_{mr} < 0$. The negative nature of ε_{mr} is responsible for the existence of the surface mode.

Although SPPs are subject to loss because of ε_{mi}, it is possible to take advantage of their surface-bound nature while substantially reducing attenuation

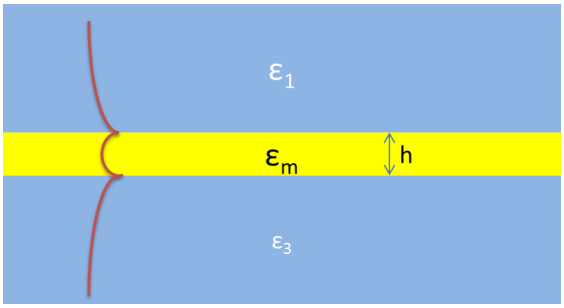

Figure 5.1: Metal slab configuration of thickness h. Decaying E-field of LRSP mode is shown.

using long-range surface plasmons (LRSPs). Consider, as depicted in Fig. 5.1 a metal slab of thickness h with dielectric on either side of it. It is clear that both metal-dielectric interfaces will independently support SPPs. Now imagine that we reduce t until it is comparable to the SPP decay length. When the two modes become sufficiently close together, they will no longer act independently. In fact, they will combine to form two *supermodes* which are linear combinations of the individual modes. This is similar to other situations where two resonant oscillators are brought togther, such as bonding and anti-bonding states of two atoms in close proximity. Although the original modes on either inteface are identical, in combination two new modes form to break the degeneracy: one symmetric (shown in Fig. 5.1) and the other anti-symmetric. Like single-interface SPPs, these modes must be TM-polarized.

In the anti-symmetric configuration, the field in the lower half-space is identical in magnitude but opposite in sign to that in the upper half-space, as is the charge density in the metal. The field is highly confined within the metal core. This implies high absorption in the metal and therefore a short propgation length. Although this mode has a zero at the waveguide center, leading one to suspect lower field confinement, it turns out that the energy is primarily carried in the core. It is the symmetric mode that is of interest here, as the anti-symmetric is mostly contained in the metal and is therefore absorbed quickly. The symmetric mode, on the other hand, has a long z-decay length in the cladding and is mostly located there. Therefore it has low loss and a long propagation length, since the

dielectric cladding is taken to be totally transmissive.

To further understand the behavior of the metal slab, we discuss the dispersion of the two modes, following the analysis of Burke [91]. For a magnetic field propagating as $\vec{H} = \vec{J}H_0 f(z)e^{i(\omega t - \beta x)}$, the field variation in the three sections may be modeled as:

$$f(z) = e^{S_1 z}, z < 0 \tag{5.1}$$

$$f(z) = \cosh(S_2 z) + \frac{S_1 \varepsilon_m}{S_2 \varepsilon_1} \sinh(S_2 z), 0 < z < h \tag{5.2}$$

$$f(z) = e^{-S_3(z-h)}, z > h \tag{5.3}$$

The relative constants in (5.2) are chosen to preserve the transverse magnetic boundary condition at $z = h$. Each boundary has a surface-bound mode which decays exponentially, as in the single interface case. The two hyperbolic sinusoidal terms in (5.2) reflect the two possible linear combinations of exponential functions, $\cosh(x) = e^x + e^{-x}$ and $\sinh(x) = e^x - e^{-x}$.

The decay factors S_i are subject to the constraints:

$$S_1^2 = \varepsilon_1 k_0^2 - \beta^2 \tag{5.4}$$

$$S_2^2 = \varepsilon_m k_0^2 - \beta^2 \tag{5.5}$$

$$S_3^2 = \varepsilon_3 k_0^2 - \beta^2 \tag{5.6}$$

These equations allow positive or negative values for the real part of S_i, but only negative values of the real part of S_1 correspond to bound modes. Note that f(z) is identical for positive or negative S_2. Since f(z) gives the variation of the transverse magnetic field, the electric field may be determined using Maxwell's equation:

$$E_x = \frac{i}{\omega \varepsilon_0 \varepsilon} \frac{\partial H_y}{\partial z} \tag{5.7}$$

Applying (5.7) to (5.2) and (5.3) and setting them equal at $z = h$ according to continuity of transverse electric field gives the following dispersion relation:

$$\tanh(S_2 h)(\varepsilon_1 \varepsilon_3 S_2^2 + \varepsilon_m S_1 S_3) + [S_2(\varepsilon_1 S_3 + \varepsilon_3 S_1)] = 0 \tag{5.8}$$

This is a transcendental equation which must be solved numerically. If the metal is taken to be lossy, i.e. $\varepsilon_m = \varepsilon_{mr} + \varepsilon_{mi}$, there will be a complex $\beta = \beta_r + \beta_i$,

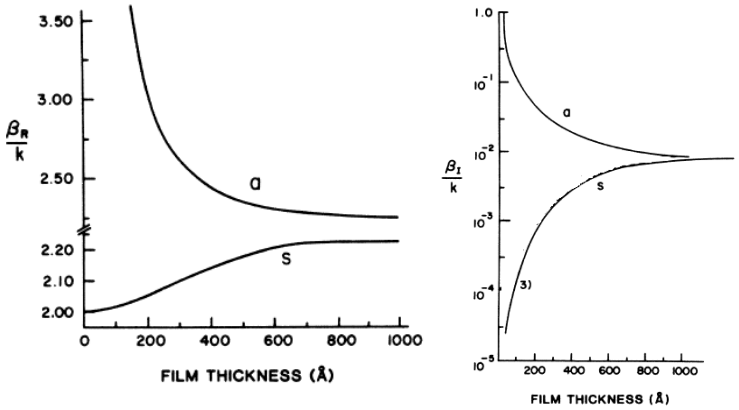

(a) (b)

Figure 5.2: Dispersion of the metal slab, from [91]. (a) Real and (b) imaginary parts of the propagation constant, scaled to vacuum wavenumber, as a function of slab thickness.

and therefore also S_1 and S_3 according to (5.6). We first consider the specific case $S_1 = S_3$, where the geometry is symmetrical about the line $z = h/2$. The intensity distribution then must be symmetrical, meaning the field distribution must be either symmetric or anti-symmetric. Additionally, (5.8) will always have two solutions. In Fig. 5.2 we present the solution from [91]. The system (5.6) and (5.8) is solved numerically for a range of thicknesses h, for a silver ($\varepsilon_m = -19 - .53i$) slab surrounded by a dielectric ($\varepsilon_1 = \varepsilon_3 = 2.13$), at a wavelength $\lambda_0 = 633$ nm. This calculation returns the values $\beta_r(t)$ and $\beta_i(t)$, which appear in the plot for both symmetric and anti-symmetric solutions.

We observe a number of interesting features here. There are two observable branches of each plot. The upper branch represents the anti-symmetric mode, while the lower branch represents the symmetric mode. For the anti-symmetric branch, β_r increases as h drops, meaning that $S_1 = S_3$ increases. This implies a faster decay into the cladding, and so conservation of energy dictates more of the optical power must be carried in the metal. The effect of the increased metal confinement is visible in Fig. 5.2(b), where we can see that as the thickness goes to 0, the loss factor β_i goes to infinity, meaning the absorption increases without limit. The symmetric mode (lower branch) exhibits the opposite behavior. A decrease

in slab thickness results in a slower decay into the dielectric cladding, which then carries more of the optical power. The loss β_i therefore declines toward 0 as the slab becomes thinner, because of reduced light-metal interaction. Therefore the symmetric mode for small h is termed a *long-range surface plasmon*. At 0, $\beta_r = \varepsilon_1 k_0$, which is the propagation constant of a plane wave in the dielectric media. This makes intuitive sense as one imagines the disappearance of the metal slab. The symmetric mode becomes increasingly like a TEM plane wave in the cladding.

At the other end of the thickness range, where $h \to \infty$, β for both modes goes to the same value as the coupled modes separate out into the single-interface SPPs. In this case $\tanh(S_2 h) \to 1$, so (5.8) becomes:

$$(S_1\varepsilon_m + S_2\varepsilon_1)(S_3\varepsilon_m + S_2\varepsilon_3) = 0 \tag{5.9}$$

This equation can be easily factored, and then β can be calculated from the values of S_i. Breaking them out into real and imaginary parts, we have for the interface with ε_1:

$$\beta_{1r}(h \to \infty) \simeq \varepsilon_1^{1/2} k_0 \left(\frac{\varepsilon_{mr}^2 - \varepsilon_{mr}\varepsilon_1 + \varepsilon_1^2}{|\varepsilon_m + \varepsilon_1|^2} \right)^{1/2} \tag{5.10}$$

$$\beta_{1i}(h \to \infty) = \frac{\varepsilon_{mi}\varepsilon_1}{2\beta_{1r}} \frac{k_0^2}{|\varepsilon_m + \varepsilon_1|^2} \tag{5.11}$$

The equations are the same for interface with ε_3, with the substitution ε_3 for the case of non-symmetric geometry.

It is clear now how the thin metal slab behaves when the dielectric medium is identical to either side of it. How does the situation vary when the dielectric is different at one interface from the other? (5.8), which is written generally, still applies in this case. However, the existence of two bound solutions is not guaranteed as it was for the symmetric case [91]. In fact, when the index difference becomes too high, the symmetric solution breaks down, and the long-range mode goes into cutoff [92]. Thus it is important that to preserve the existence of the long-range plasmon mode, the indices must be sufficiently matched for the slab thickness.

5.2 Metal Slab Configuration

While the original work on LRSPs centered on metal slabs of infinite width, in 1999 Berini [93] first investigated the propagation of LRSPs on metal waveguides of finite width. This is known as the metal stripe configuration, and is useful since it can keep power confined in two dimensions rather than one. This configuration may be more practical for real implementation of LRSPs at the chip scale for practical purposes due to its high power concentrations. The stripe arrangement, due to its more complicated geometry, does not lend itself to analytic calculations, even of the dispersion relation. However, we may simulate it to estimate its performance.

The typical thickness of the metal stripe is similar to that of the metal slab, on the order of 20-50 nm. The width, however, may have considerable variance, from 1 µmto 10s of µm. There is effectively no maximum, as the metal stripe with infinite width is simply the metal slab previously considered. High widths introduce many new modes beyond the fundamental which vary in their horizontal distribution. The modes vary in four basic ways and are named accordingly. They may be symmetric or anti-symmetric in the x and y directions, which give the first and second letters respectively (a or s). They may be bound or leaky; here we consider only bound modes, which have a 'b' as a subscript. Finally, higher order modes will have higher numbers of nodes, which are used as a superscript in the modal nomenclature. Thus, the sa_b^0 mode is symmetric along the transverse (x) direction, anti symmetric perpendicular to the waveguide surface (y direction), and has no nodes along x.

The mode of interest in this study is the ss_b^0, which corresponds to the s_b long range surface plasmon in the metal slab. It is easy to see in Fig. 5.3 that this mode is highly deconfined, as compared to the other bound modes of the metal stripe. It has a long propagation distance for that reason. At 1550 nm, the COMSOL simulation reveals the ss_b^0 mode has $\Re[n_{eff}] = 1.445$, close to the silica cladding index of 1.444, due to the low confinement. Since the field has very little overlap with the metal, it has an extremely low loss $\Im[n_{eff}] \sim 10^{-5}$. For comparison, the other low-order modes all have loss factors on the order of .01, so they are absorbed quickly even under ideal conditions. The low loss of the

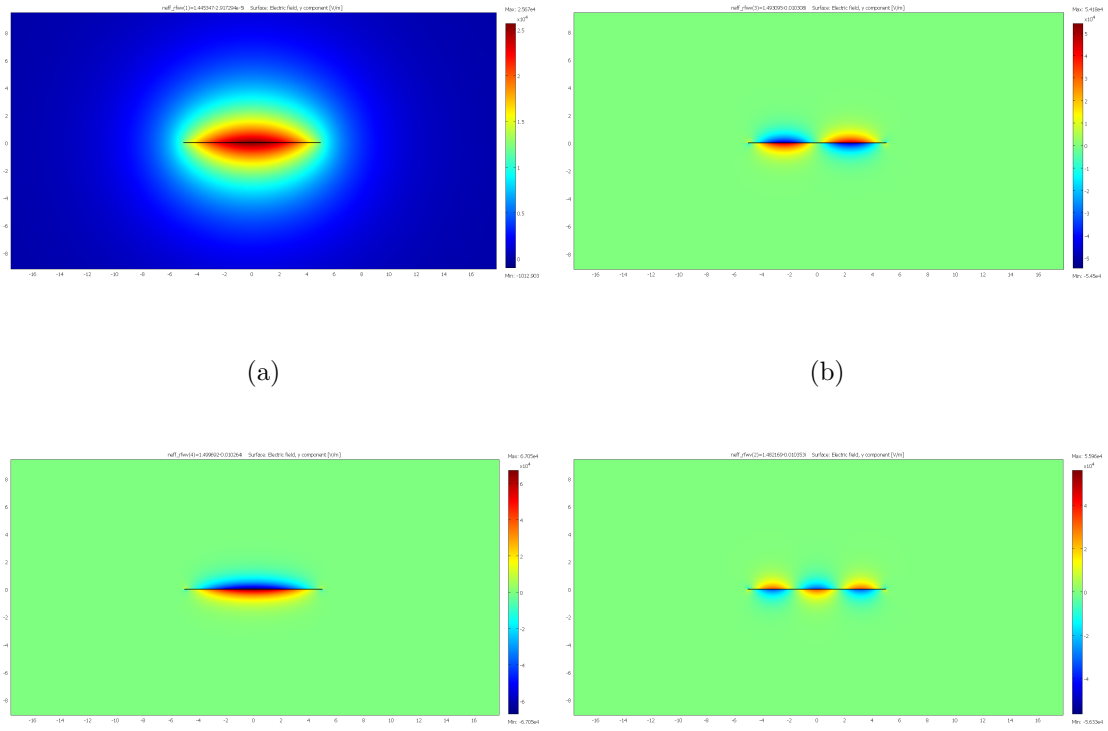

(a) (b)

(c) (d)

Figure 5.3: $E_y(x, y)$ for several modes of the metal stripe. (a) ss_b^0 (b) aa_b^1 (c) sa_b^0 (d) sa_b^2. The low confinement of the ss_b^0 long-range surface plasmon mode, which allows it to propagate long distances, is easy to see here.

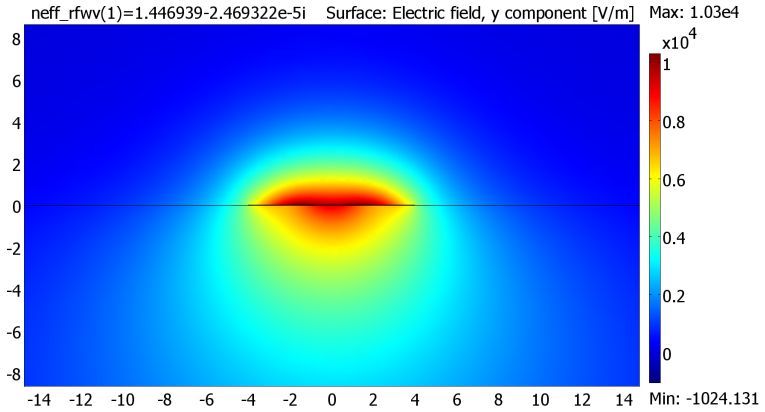

Figure 5.4: COMSOL simulation of 20 nm Au stripe between dielectric media of $n = 1.444$ and $n = 1.448$. Mode is drawn into high index substrate but is still bound rather than leaky.

ss_b^0 mode allows it to be termed a long-range surface plasmon mode, and to have potential practical applications in integrated optics.

As in the slab, the index matching between the undercladding and overcladding is critical in the metal stripe to maintain a bound symmetric mode for small thickness of the metal. This effect is visible in Fig. 5.4, which shows the mode of a 12 µmAu stripe bounded below by a medium of $n = 1.448$, and above by a medium of $n = 1.444$. The field is drawn into the high-index medium, causing a geometrical imbalance in the mode distribution. For small index mismatch, the simulation converges on a bound solution, which for these parameters has $n_{eff} = 1.447 + 3.59 \times 10^{-5i}$.

As the index mismatch on either side of the metal stripe increases, the field increasingly projects into the high-index medium, until it cuts off. This can be seen in Fig. 5.5(a), which is adapted from [94]. The structure under consideration here is a 20 nm-thick Au stripe of varying width on an SiO_2 ($n = 1.447$)-like medium. The effective index is plotted for a range of overcladdings ("superstrates") as a function of the index contrast Δ between the two media. The modes enter cutoff when their effective index reaches the higher index of the two claddings. For $\Delta < 0$, the cutoff occurs at $n = 1.447$, while for $\Delta > 0$, the index of the higher

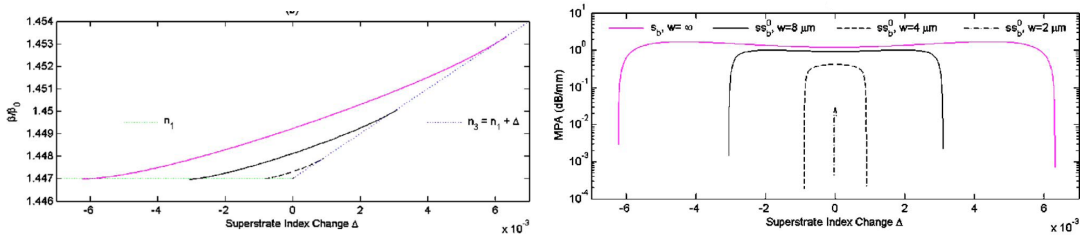

(a) (b)

Figure 5.5: Effects of cladding index mismatch on metal stripe LRSP for a variety of stripe widths. (a) Effective index dominated by higher index medium. (b) Modal power attenuation (loss) exhibits small variation ¡ 10 for most of range, then drops rapidly near cutoff index contrast

index medium varies according to the superstrate contrast $n_2 = n_1 + \Delta$. This makes sense, as in the limit where the mode is pulled out of confinement and into a free-space wave in the high-index region (i.e. cutoff), its effective index would be the index of that region.

We can also examine the effect of index mismatch on the propagation loss, which is given as the modal power attenuation (MPA) in Fig. 5.5(b), also from [94]. Initially the loss increases slightly with increasing index difference, corresponding to an increased penetration depth into the metal from the low-index side. Past a critical value of Δ, the loss drops rapidly. In this regime, the field is distributed primarily in the high-index dielectric, which is taken to be lossless. Ideally the indices would be chosen to be in this regime, but in practice this is not feasible because of the very low index range before the waveguide enters cutoff, represented by the asymptote of the plot. Therefore we typically desire $\Delta = 0$, which has the lowest realistically available MPA. It is absolutely essential that Δ be sufficiently small to put the waveguide outside of the cutoff region.

This sensitivity to index mismatch has posed a challenge for applying NSOM to long range plasmon structures. Although there is an extensive history of NSOM characterization of surface plasmons in general, there have been limited efforts towards NSOM characterization of LRSPs. Since the top and bottom claddings must be of equal index, to allow propagation of LRSPs in an air environment requires the creation of suspended waveguides, a technically challenging

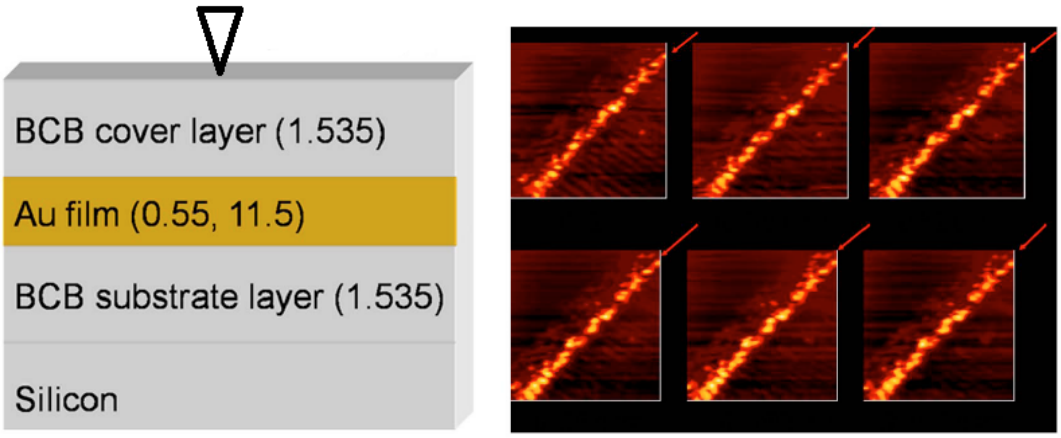

(a) (b)

Figure 5.6: NSOM experiment on LRSP imaging from [95]. (a) Experimental setup, with solid dielectric layer on either side of Au film. (b) Optical intensity distribution recorded by NSOM for various tip heights from 0 to 1000 nm. Because the tip sits atop a solid dielectric, the NSOM actually records far-field scattering rather than near-field evanescent waves. Both images adapted from [95].

feat. Traditionally, NSOM has been limited to the air environment.

One attempt in this direction was made by Salakhutdinov *et al.* [95]. Their experimental setup is depicted in Fig. 5.6(a). A gold stripe on a BCB (benzocyclobutene, $n = 1.535$) substrate is symmetrically coated with a BCB layer on top. The LRSP mode is excited by endfire coupling, and the NSOM tip is scanned over the BCB surface to detect the near-field signal. Their results are shown in Fig. 5.6(b). Although there is a detected signal which corresponds roughly to the waveguide shape, it should be noted that this is not the LRSP mode being evanescently coupled to the tip, since the probe is not being placed in the near-field. Rather, as the authors say, "the light collected by the SNOM is scattered light from the surface and not the evanescent field." The detected signal is from light scattered by the rough metal-dielectric interface; thus even though it originates in the LRSP mode, this is a far-field detection method which can offer none of the traditional advantanges of NSOM.

The liquid NSOM technique we developed in Chapter 4 offers the potential to achieve a true near-field measurement of LRSPs. Here we use a liquid cladding

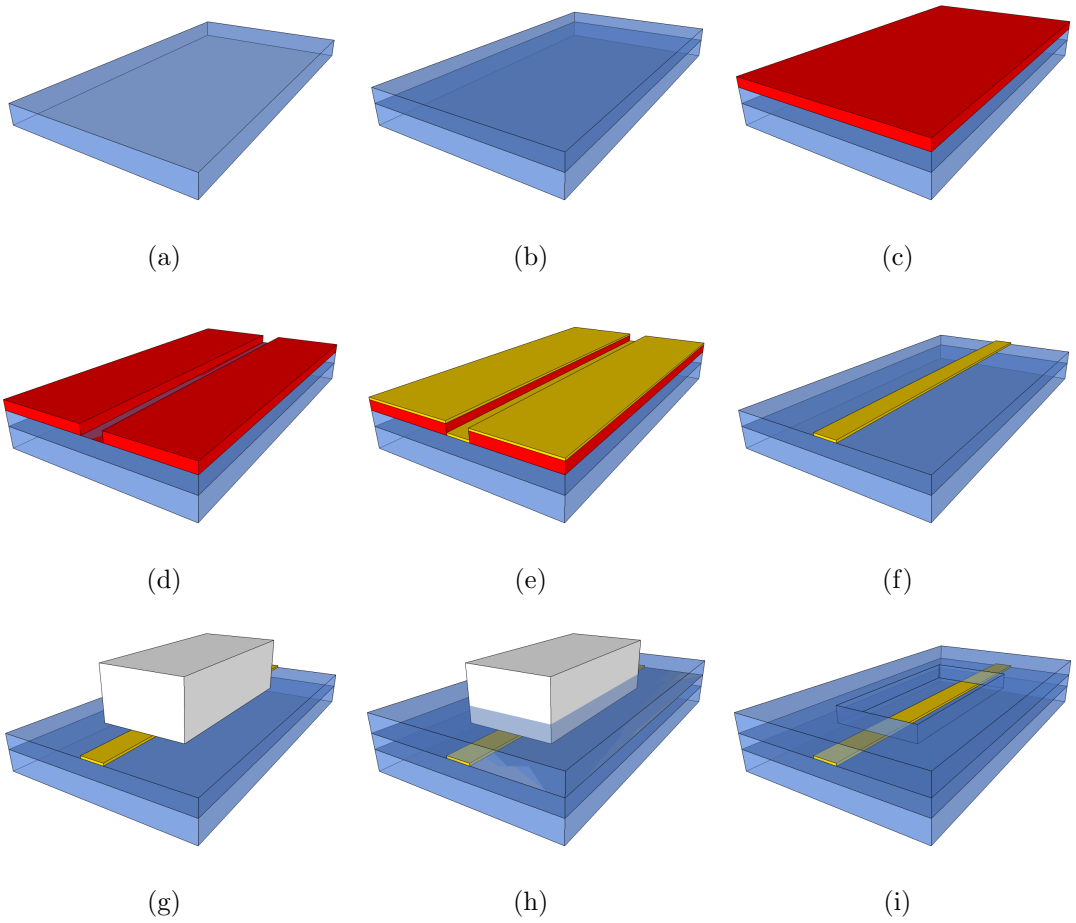

Figure 5.7: LRSP waveguide fabrication process. (a) SiO_2 wafer. (b) PECVD of additional SiO_2. (c) Spin-coating of SU8 resist. (d) Photolithography. (e) Evaporation of 20 nm Au layer. (f) Liftoff of SU8. (g) Placement of macroscopic Si block. (h) PECVD of SiO_2. (i) Removal of Si block

which is index-matched to the substrate to maintain refractive index symmetry while allowing the near-field probe direct access to the evanescent fields at the core-cladding boundary. The device is fabricated in a manner tailored to the NSOM measurement, then bonded using a version of the process described in Chapter4, then measured in amplitude and phase with the liquid NSOM. This represents the first true near-field imaging of long-range surface plasmons.

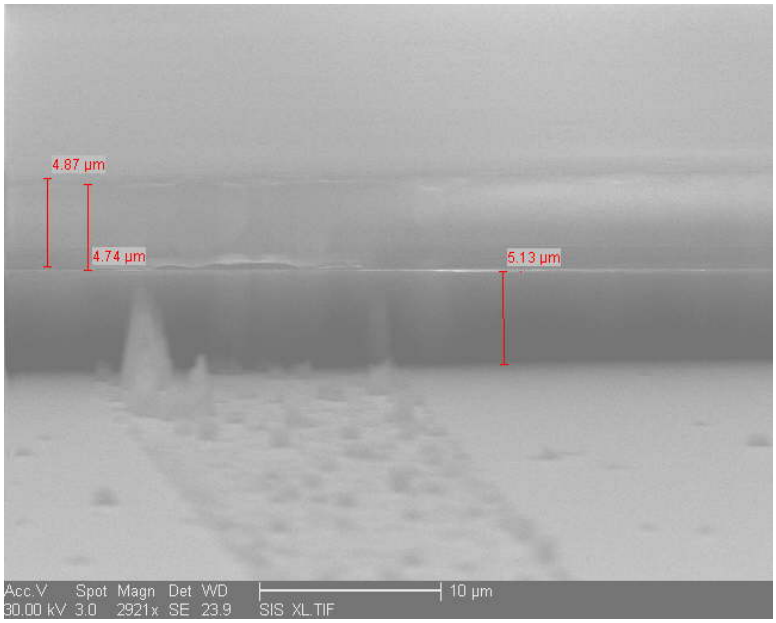

Figure 5.8: Sample after attempted window etching. Waveguide destroyed due to Ar sputtering.

5.3 Sample Preparation

The chip consists of several sets of gold waveguides, with widths ranging from 2 to 20 µm, on a silicon dioxide substrate. The fabrication process is detailed in Fig. 5.7. An SiO_2 wafer is coated with another layer of thermal SiO_2 by PECVD (plasma-enhanced chemical vapor deposition). The thermal oxide layer is necessary in order to maximize index matching to the top layer of SiO_2 which will have to be deposited layer. SU-8 negative photoresist is spin-coated on a SiO_2 wafer, then exposed by photolithography according to a prefabricated mask with the waveguide pattern. After developing, 20 nm of gold is deposited by e-beam evaporation. Although it is frequently difficult to adhere gold films to glass, the gold adheres well because at low thickness, it forms a series of islands which have high adhesion rather than a single film. However, the gold still behaves optically as a single film. The resist is removed by acetone in a liftoff process, leaving the gold waveguides on the SiO_2 substrate. At this point it is necessary to apply another layer of SiO_2 as an overcladding.

Ideally, the overcladding would not be necessary due to the liquid cladding.

However, as will be explained later, a partial cladding is required for the fiber bonding process. Specifically, we seek to have the edges of the chip coated in SiO_2, with a "window" open in the center to allow the probe access to the waveguide. In practice, this is a significant fabrication challenge. One approach is to fabricate the chip, deposit the SiO_2 overcladding, then perform reactive ion etching (RIE) to remove the window. In this case the oxide is etched with a mixture of CHF3 and Ar. Even though the difficulty of knowing the exact etch rate to sufficient precision prevents being able to stop the etch exactly at the top of the waveguide, in principle the waveguide itself, being made of non-reactive gold, should act as a mask for the SiO_2 beneath it which will remain unetched and provide structural support. The liquid cladding would then fill in the gaps created between the waveguides. In practice, the waveguide is destroyed during etching. A scanning electron micrograph showing the results of this process is given in Fig. 5.8. The remnants of the waveguide are clearly visible. The most likely explanation is that the gold was mechanically sputtered away by the argon atoms, a well-known effect frequently used in metal deposition, and without it the SiO_2 could be etched off by the CHF3. It should be noted that even without any argon, the waveguides were still destroyed; it is probable that the CHF3 is also capable of sputtering gold.

A form of liftoff was therefore pursued as an alternative approach. In a traditional liftoff process, a resist is deposited and patterned, after which the material of interest is deposited. The resist is then removed, leaving the material in the pattern defined by the original mask. For liftoff to be successful, the resist layer must be thicker than the final material, to separate the pieces to be lifted off from those to remain on the sample. The SiO_2 must be several µmthick, while the thicknesses of spin-coated layers of resist typically max out on the order of several hundred nm. To form the window, a 350 µmthick piece of silicon wafer, diced to a 5 mm x 1mm area, was placed atop the chip before PECVD of 6 µmof SiO_2. Silicon was chosen as a block material over SiO_2, which posed the risk of bonding to the cladding or the substrate, and metal, which could bond to the gold. After PECVD, the wafer was simply removed by hand, leaving a window where the chip had no cladding. A micrograph of the window edge is shown in Fig. 5.9. The

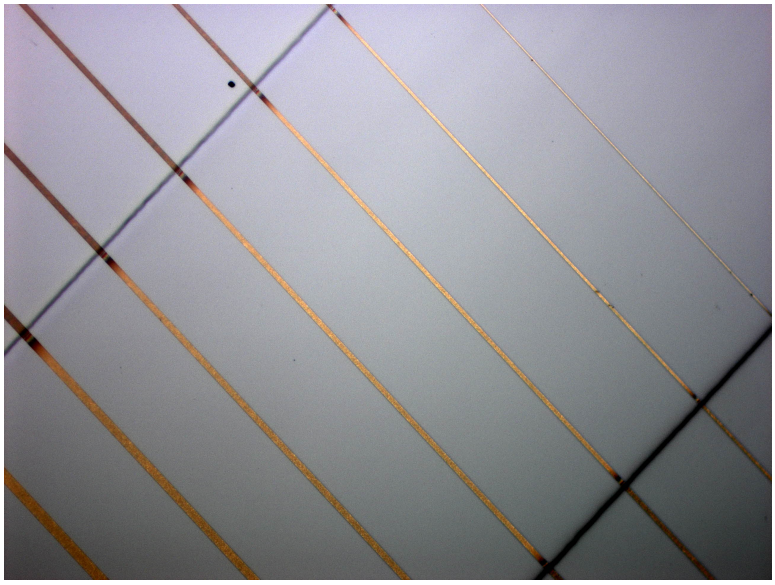

Figure 5.9: Au waveguides on SiO_2 with window created by the Si block method. The waveguides are visibly intact without damage from the block.

edge is well-defined, and no damage appears to have been done to the waveguides. The sloped sidewall of the window is visible as a multicolor thin-film interference pattern immediately adjacent to the edge.

The next step was to bond a fiber, as before, to the chip aligned to one of the LRSP waveguides. In the case of the silicon waveguide, the waveguide is able to transmit light without any overcladding, allowing the fiber bonding to be done without the liquid cladding. The LRSP waveguide however requires a symmetric cladding environment to carry the mode. Thus the liquid cladding must be in place for the fiber bonding process. The refractive index oils used are likely to interfere with proper setting of the epoxy, so the window previously described was created to contain the liquid cladding, with the solid-clad portion having refractive index symmetry permitting the LRSP mode to propagate. It was found experimentally that the sidewalls are too shallow at 6 µmto contain the fluid. The window still serves an important role as surface tension allows a drop of index-matching oil to sit at the chip center. When aligning the fiber for bonding, the presence of the SiO_2 cladding at the edges ensures LRSP propagation, while the liquid-filled center later enables NSOM measurements. Additionally, the SiO_2 layer provides superior

index matching to the epoxy used in the Si waveguide experiment.

To prepare the chip for fiber bonding, it is inserted in the previously described fiber-free space transmission setup. A drop of index-matching oil (Cargille Series A 1.46) small enough to just cover the window without spreading is placed at the chip center. For the initial alignment, the fiber is turned to produce a 45°polarization. The fiber is translated until a suspected output waveguide mode is seen on the video camera. The output polarization is then measured by rotating a linear polarization analyzer. If the mode is maximum when the analyzer pass axis is vertical (corresponding to TM), it is taken to be the LRSP mode. The background is at 45°as initially chosen. This disparity between the signal and background polarizations allows discrimination between the two, even though the straight nature of the waveguides (necessitated by the high bending loss of the LRSP) causes a great deal of background light to appear on the camera. Then the fiber is turned to be TM-polarized, and realigned by visually matching the output mode to the image recorded at 45°polarization.

A drop of OP-4-20632-GEL epoxy is deposited on the fiber facet. Although this epoxy is not index-matched to the substrate as well as the OP-20 used in the Si waveguide experiment, index matching is no longer necessary due to the solid overcladding. The fiber is brought close to the waveguide, maintaining alignment, and moved toward the chip until the drop bridges the fiber-chip gap. The epoxy is cured with UV light, and the fiber is bonded again to the slide on which the chip sits for mechanical stability.

5.4 NSOM Measurement

The experiment is based on providing a liquid cladding for the gold waveguide chip, index-matched to the SiO_2 substrate. For index-matching to be successful, the liquid must be sufficiently close in refractive index at the wavelength chosen to the substrate to sustain the LRSP mode. The allowed Δn before the waveguide goes into cutoff depends on the stripe thickness and width, as shown in Fig. 5.5. Refractive index oils are commercially available in a range of indices from ~ 1.3

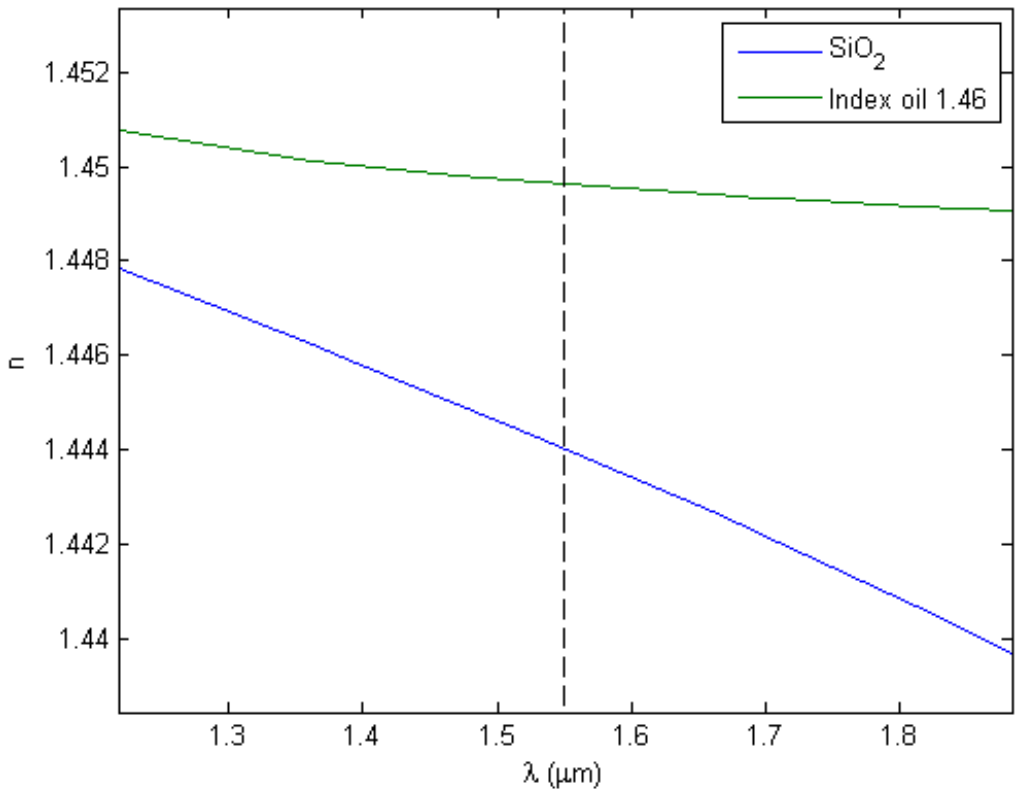

Figure 5.10: Index matching between SiO_2 deposited by PECVD and Cargille Refractive Index Liquid Series A 1.46 near 1550 nm wavelength, marked by dashed line.

to ~ 1.8; this experiment used Cargille Series A 1.46, which is so named because it has $n(\lambda = 589nm) = 1.46$. Since the experiment is being done at 1550 nm, we must consider the dispersion, which can be approximated for a liquid according to the Cauchy relation:

$$n(\lambda) = A + B\lambda^{-2} + C\lambda^{-2} \tag{5.12}$$

Typically (5.12) is accurate to within .005. For this liquid, the coefficients are given by the manufacturer as $A = 1.447924$, $B = 4.074357 \times 10^{-8}\mu m^2$, $C = 4.15 \times 10^{-5}\mu m^4$. The SiO_2 dispersion is obtained from [96]. The dispersion relations $n(\lambda)$ near 1550 nm are compared in Fig. 5.10, with a vertical dashed line marking the wavelength of choice. As the wavelength increases, the refractive indices separate. At 1550 nm, for SiO_2 $n = 1.444$, and for the oil $n = 1.450$. This is just at the edge of the range allowed in Fig. 5.5 for an 8 µmguide at 20 nm thickness. However, given the Cauchy tolerance of $\pm.005$ and the increased width of the waveguide used in the experiment (12 µm), this difference may be acceptable.

The fiber-connectorized chip is coated with the index-matching oil and characterized with the NSOM at 1550 nm wavelength. The waveguide was 20 nm thick and 12 µmwide. Topography, amplitude, and phase are all measured within the window with the fast axis of the scan set to the longitudinal direction. The results of the scan are shown in Fig. 5.11. A few interesting features are notable in the plots. The topography recorded by AFM displays a rough texture. This is caused by the e-beam evaporation method discussed previously, which results in isolated islands rather than a single film. The roughness is visible on both the trace and retrace signals, which gives confidence that it is real and not an artifact of the probe oscillation.

The optical amplitude shows a signal clearly correlated with the location of the waveguide. There is a visible modulation in the amplitude signal along the direction of propgation. This modulation is likely to be due to interference between the guided LRSP mode and stray light from the illuminating fiber. The phase signal displays a number of bright spots seemingly randomly distribut ed in space, but also a faint modulation in the direction of propagation underneath. The bright spots are correlated to points of high optical amplitude. As established

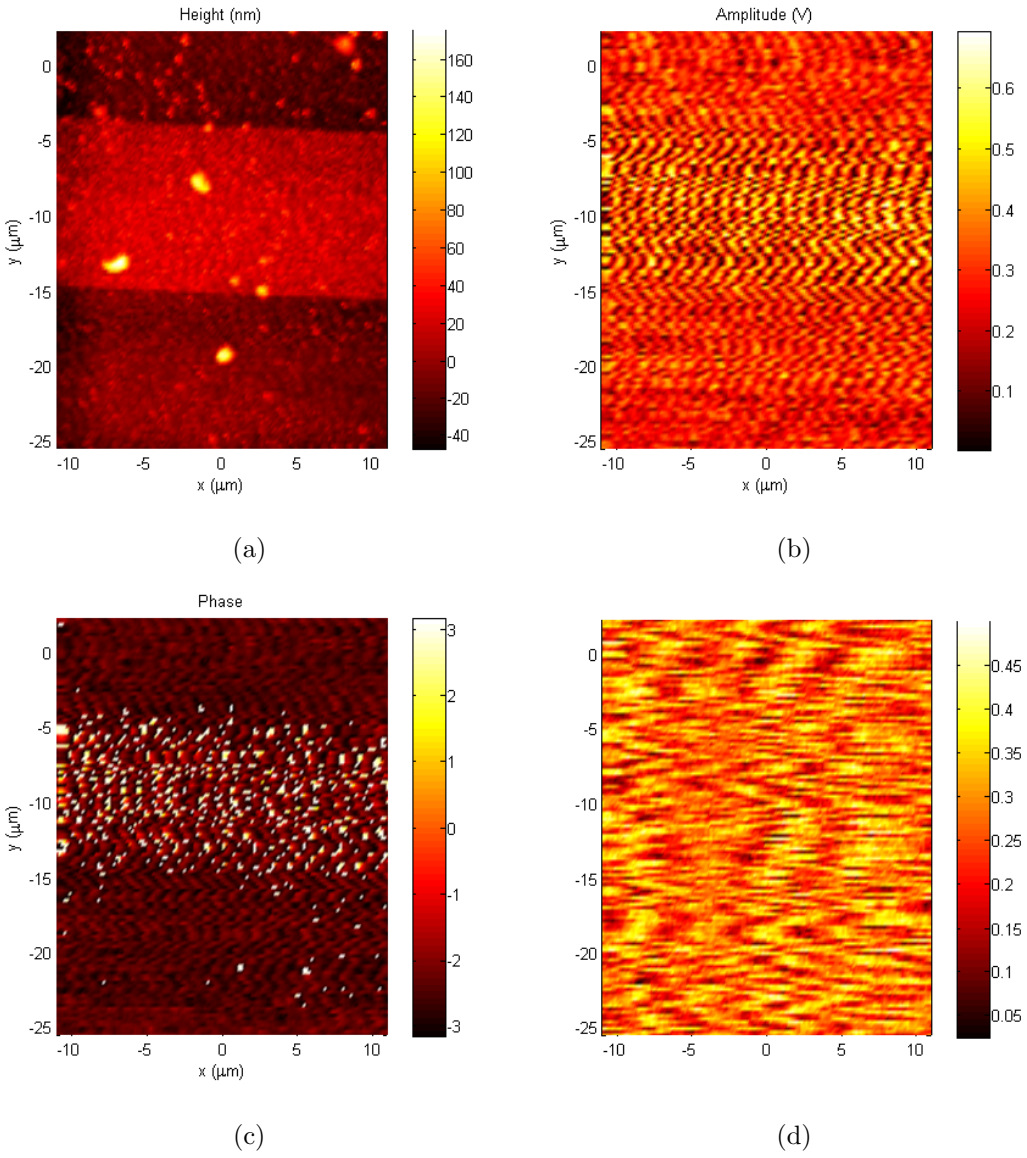

Figure 5.11: Results of NSOM measurement of LRSP sample. (a) Topography. (b) TM amplitude (c) TM phase (d) TE amplitude.

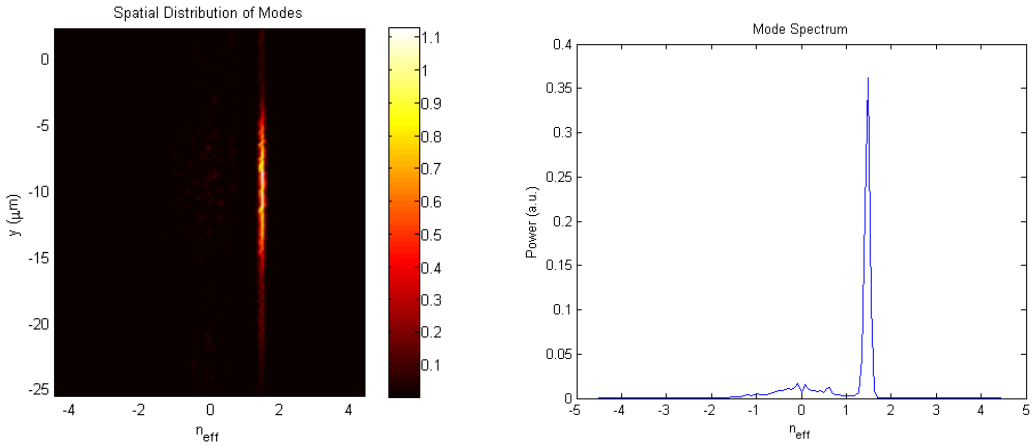

(a) (b)

Figure 5.12: FFT of the LRSP data. (a) One-dimensional FFT showing transverse distribution of a single LRSP mode. (b) Mode spectrum produced by integrating along the transverse direction, showing a single LRSP mode at $n_{eff} = 1.47$.

previously, we can also combine the two signals in a plot of one field component $A \sin \phi$. The modulation appears here too, and there is no discrepancy between the amplitude and phase.

We can confirm the existence of the guided plasmonic mode, as opposed to stray light propagating from the fiber and scattering from the top, by varying the polarization. To switch the input polarization to TE rather than TM, a slow-to-fast axis PM fiber was inserted between the linear polarizer and the device pigtail. The device was remeasured under the same experimental conditions in the orthogonal polarization. The detected optical amplitude is shown in Fig. 5.11(d). It is easy to see that no signal propagates in this TE polarization, which serves as evidence of the plasmonic nature of the signal detected under TM illumination conditions.

We may also analyze the modal properties of the detected signal by Fourier analysis, as previously discussed in Chapters 3 and 4. With the amplitude $A(x, y)$ and phase $\phi(x, y)$ from the NSOM data, we calculate $\mathcal{F}_x(A(x, y)e^{i\phi(x,y)})$ using the FFT. Prior to taking the Fourier transform, the mean of each scanline is subtracted from each datapoint in that line in order to remove the DC component visible in the amplitude data. The transform is also taken with a Hamming window applied to the data as discussed in Chapter 4. This calculation gives the modal structure

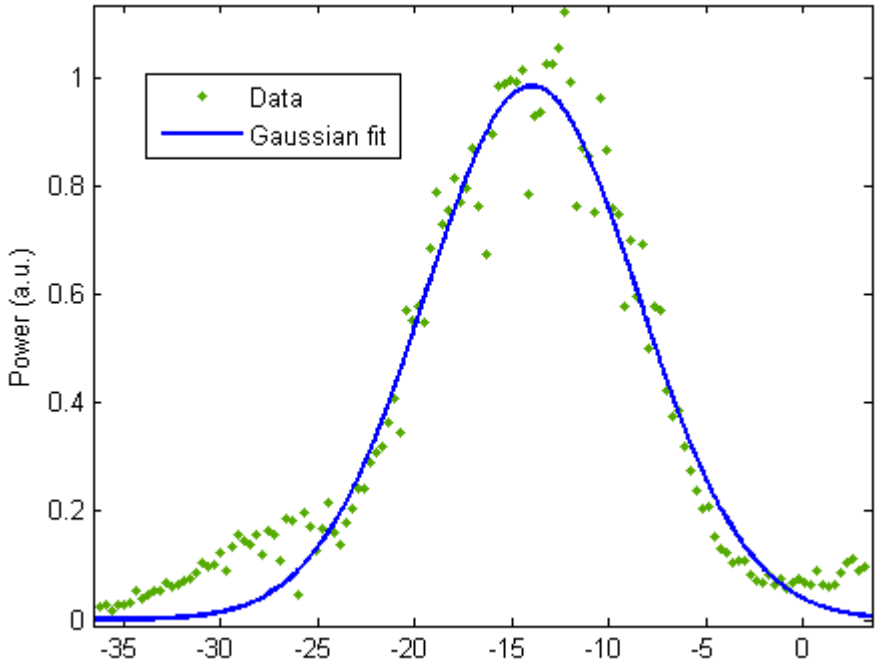

Figure 5.13: Transverse distribution of the LRSP mode with Gaussian fit. Fit has FWHM=12.9µm, with $R^2 > 95\%$.

which is shown in Fig. 5.12(a), with the transverse-integrated spectrum shown in Fig. 5.12(b). We observe a single mode, at an effective index of $n_{eff} = 1.47$, as compared to the simulated value of $n_{eff} = 1.45$. As expected, this is close to the SiO_2 cladding refractive index of 1.44 due to the low confinement of the LRSP mode. There is no measurable reflected mode visible for $n_{eff} < 0$.

It is also interesting to examine in detail the transverse distribution of the mode. Fig. 5.13 shows a cross section of the mode across a single effective index from Fig. 5.12(a). The distribution data is fit with a Gaussian function $Ae^{-\frac{(x-x_0)^2}{2\sigma^2}}$. Although we do not expect the mode shape to be defined by a Gaussian, it turns out to be an empirically good model with $R^2 > 95\%$. The fitting returns values of $x_0 = -14$µm and $\sigma = 5.50 \pm .21$µm. This distribution has $FWHM = 2.35\sigma = 12.9$µm, a reasonable value given the waveguide width of 12 µmand the extent of the ss_b^0 mode over the full width.

Chapter 6

Conclusion

In this dissertation we have explored techniques in heterodyne near-field imaging of integrated photonic devices, and introduced the concept of H-NSOM in a liquid environment. The operation of the heterodyne interferometer was discussed in conjunction with the principles of near-field imaging with aperture tips. We applied this to several samples in order to explore new possibilities.

First, we used the H-NSOM to analyze the operation of an asymmetric mode converter designed to break PT symmetry on a silicon photonic chip. The electric field propagating through the converter was imaged with propagation in both directions. The image clearly showed conversion from the first mode to the second mode in one direction, with no conversion in the other direction. Since the H-NSOM records both amplitude and phase, it was possible to apply a Fourier transform to the complex field to determine the mode structure of the fields. A 1-D FFT was applied both before and after the device, which separated out the modes of propagation according to their effective indices, while preserving their transverse distributions. Similar to the pure amplitude image, this visibly demonstrated one-way mode conversion.

Next, NSOM imaging of amplitude and phase in liquid-clad waveguides was introduced. Although integrated photonic devices are typically fabricated with a solid overcladding, the presence of the cladding prevents the NSOM probe from accessing the core-cladding boundary. Therefore we substituted a liquid cladding to emulate the solid cladding in the real device. Silicon channel waveguides were

fabricated on SiO_2, and one of them was pigtailed with polarization-maintaining fiber, using inverse tapers to solve the issues of misalignment due to epoxy shrinkage. Using a liquid-capable NSOM, we measured the amplitude and phase of 1550 nm light propagating in the waveguide, with claddings of both air and water. We then used Fourier analysis to measure the effective index in both situations. The measured effective indices corresponded closely to COMSOL simulations, and demonstrated a shift of .08 between the two, both validating the technique and establishing its importance for accurate characterization of phase in real devices.

Finally, the liquid cladding technique was applied to long-range surface plasmons in Au-on-SiO_2 stripe waveguides. LRSPs require a symmetric cladding environment to propagate due to their low confinement. To allow bonding to the fully clad edge while maintaining a space for NSOM analysis, the waveguides were fabricated with a window in the SiO_2 overcladding. The sample was immersed in index-matching oil and measured with the H-NSOM under TM excitation at 1550 nm. The amplitude demonstrated a clear correlation with the waveguide topography. There was a visible amplitude modulation due to interference of the LRSP mode and the incident free-space light. The FFT, using both amplitude and phase, showed a single mode at an effective index of 1.47, close to that predicted by simulation. To verify the plasmonic nature of the measured field, the incident light was turned to TE, and no signal was observed, confirming the validity of the observation. Thus the the liquid cladding technology enabled measurement of a mode previously unobservable by near-field techniques.

Chapter 7

Future Directions

The techniques introduced in this dissertation open the door to a number of possibilities in near-field imaging. The potential to combine subwavelength imaging in a liquid environment with heterodyne detection enables a new source of contrast for a multitude of applications. In this chapter we explore several of these possibilities and suggest areas of research to develop them.

Extending the work done in Chapter 4, using liquid cladding for silicon and other integrated photonic devices offers the potential to accurately characterize these devices as a standard part of the fabrication and testing procedure. A wide variety of silicon photonic devices, such as modulators, gratings, and couplers, should be imaged with index-matching liquid cladding to understand how fields propagate within them in their true form. This is particularly essential for low-confinement modes. As observed in the case of both inverse tapers and long-range surface plasmons, waveguide modes with low confinement require a symmetric cladding medium due to their tendency to be drawn into the region of higher index. In addition to the modes previously mentioned, there are generally second- and higher-order modes available in waveguides with a symmetric cladding not available when the top cladding is removed. NSOM analysis of waveguide behavior in these regimes can offer useful insights, whether the presence of these modes is desired in the final device or not. Finally, index symmetry of the cladding environment has important effects in 2-d photonic crystal devices, so liquid NSOM may find applications there.

Another potential application is phase contrast imaging of live cells. A liquid environment is generally necessary to keep cells alive, so one can easily imagine using the liquid-capable NSOM for bioimaging. NSOM has an extensive history in biological imaging, but the introduction of phase contrast could allow new features to be resolved in a label-free fashion. One can conceive of illuminating an immersed cell from below, through the transparent mount, and measuring the transmitted field over a given area using the H-NSOM. An aqueous solution could be flowed in and out of the NSOM's liquid cell, and introducing the solution at the appropriate temperature would allow cell survival for signifcant periods of time. In this configuration, the phase signal would correspond to variations in the refractive index and thickness, potentially showing important cell features. This method would be highly surface-sensitive, so the image would be of features at the cell membrane. Surface features are essential in many cellular proceses such as sensing. One such application would be validating the autodigestion hypothesis of insulin resistance, which holds that surface insulin receptors are cleaved due to the presence of certain enzymes. The liquid NSOM technique offers the opportunity to introduce such enzymes in the cell environment and image the receptors directly in optical phase contrast.

Optofluidics has garnered strong interest in recent years. The combination of optics with microfluidics has enabled a wealth of applications in the areas such as sensing, liquid core waveguides, and imaging. In principle, liquid-capable heterodyne NSOM can be a useful tool for characterizing optofluidic devices. This will require a strong understanding of the optical as well as mechanical effects of the tip on the measurement. In liquid-core waveguides, for instance, the presence of the tip may serve as an impediment to flow. However, if these questions are resolved or minimized, the NSOM can offer direct visualizations of the near-field effects of phenomena such as analyte binding, as well as provide a diagnostic aid for devices that do not work as expected. The presence of phase information increases the utility of H-NSOM for these applications.

The effect of the tip on the measurement is a significant issue for the NSOM community. It is an ongoing question to what extent the fields measured by the

NSOM, for a given structure, represent the fields which would be present if the tip were not there. A number of approaches have been attempted toward minimally perturbing near-field tips. Some of these include fluorescent particles being used as NSOM probes. This approach can be expanded by index-matching the fluorescent particle to the surrounding liquid medium. One can choose a particle of the same refractive index as the tip holding it (typically SiO_2), immersed in a liquid of the same index. In this arrangement, the only perturbation is the evanescent field asborbed by the particle being reradiated to the environment. However, there is no "lightning rod" effect due to the presence of the metal, and it is not possible to use the heterodyne setup because of the difference in wavelength between the source and detection wavelengths. Additionally, the sample may heat according to the local electric field, which will vary the fluorescence behavior.

More generally, a strategy of tip design for minimal perturbation should be pursued. Metallized aperture tips are highly perturbative, which causes problems in resonant structures as well as structures supporting localized surface plasmons. In addition to fluorescent particles, the use of single-particle metallic probes is recommended, in particular with index-matching liquid to "hide" the tip. We can extend this to nanoantenna-based probes specially designed for increasing field localization, such as metallic tapers, bowties, and nanocrescents. These types of probes siginfiicantly increase imaging resolution, but metal-metal interactions are responsible for unpredictable behavior in imaging of metallic samples, so it is worth devoting effort to reducing their effect on sample behaviors.

Appendix A

Fourier-Space Measurement of Surface Plasmon Dispersion

Here we briefly present a near-field method used to measure the spatial dispersion relation of a metal film. Similar methods have been presented in [97, 98].

We consider a rough silver film of arbitrary thickness in air under collimated illumination at an angle θ (see Fig. A.1(a)). To excite a surface plasmon, a wavevector must be introduced to compensate the difference between the surface plasmon wavevector k_p and the component of the wavevector which lies in the plane k_x. The film roughness $R(x)$ has many different spatial frequency components, which can be determined by its Fourier transform:

$$\tilde{R}(k) = \int R(x) e^{ikx} dx. \tag{A.1}$$

When $k = k_p - k_x$, for $|\tilde{R}(k)| > 0$, there exists a grating within the film roughness capable of converting the incident light to a plasmon at the silver-air interface. The conversion efficiency is determined by the magnitude of $|\tilde{R}(k)|$.

The NSOM (MV-2000) tip is scanned over the sample within the spot created by the beam, and records an image corresponding to the interference between the planar components of the incident light and the propagating surface plasmons. This interference is given by:

$$I(\vec{r}) = |E_p e^{i\vec{k}_p \cdot \vec{r}} + E_0 e^{i \sin\theta (k_x \hat{x} + k_y \hat{y}) \cdot \vec{r}}|^2 \tag{A.2}$$

A k-space diagram of the interference between the two components given by (A.2) is shown in Fig. A.1(b). We note a number of critical features. There are two possible circles in k-space where interference occurs, corresponding to positive and negative frequencies. The radius of the circles is k_p, so it is a direct measure of the surface plasmon frequency. Each is off-center by an amount $k_{||} = k_i \cos\theta$, the projection of the incident k-vector in the $x - y$ plane.

The measurement returns the amplitude distribution shown in Fig. A.1(c). Although it is difficult to directly extract any information from this image, it is composed of the interference intensity given by (A.2). By taking the FFT of the amplitude image, as shown in Fig. A.1(d), we can directly examine its frequency content which corresponds to the spatial dispersion of the surface plasmons. The obtained image fits well the model shown in Fig. A.1(b). We observe identical two circles, due to the inherently symmetric nature of the FFT, with the separation between the two given by the incident angle. The circle radius is 1.2 μm^{-1}. We can calculate the surface plasmon dispersion relation according to:

$$k_p = \frac{\omega_0}{c}\sqrt{\left(\frac{\varepsilon_1\varepsilon_2}{\varepsilon_1\varepsilon_2}\right)} \tag{A.3}$$

Plugging in the values for air $\varepsilon_1 = 1$ and Ag $varepsilon_2 = 123$, we find $k_p = 1.3\mu m^{-1}$, very close to the measured value.

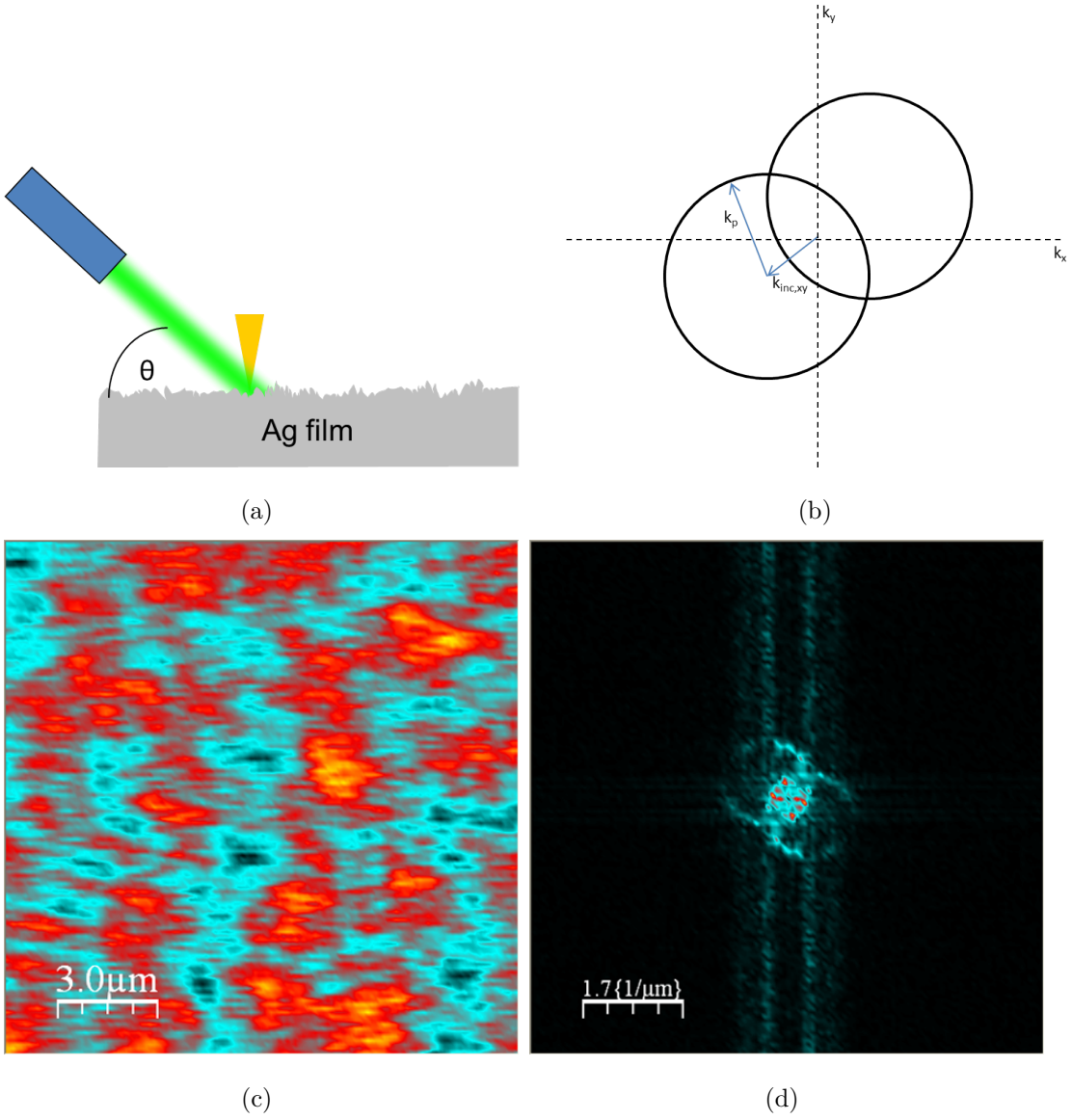

(a) (b)

(c) (d)

Figure A.1: (a) SPP interference experimental setup. (b) Diagram of the interference between the incident field and the omnidirectional surface plasmons. (c) Amplitude distribution measured on the silver film.

Appendix B

MATLAB Code for Data Processing and Analysis

```
function S = importNSOMData (filename)
%take NSOM data from file, put each variable in plottable
    matrix form in
%structure S

if nargin < 1
    f = fullget; %pick a file of NSOM data to import
else
    f = filename; %use the file given in the function
        argument
end
raw = importdata(f); %load the file into variable raw

if(not(isfield(raw,'colheaders'))) %if the file doesn't
    parse properly
    disp('Fixing NSOM Data File....')
    f_fixed = fixNSOMFile(f); %fix it!
    raw = importdata(f_fixed); %now switch to the data from
```

```
        the fixed file
end

[points channels] = size(raw.data);

[S.path, S.filename] = fileparts(f);


%note that x axis is always used as fast axis, and y axis
    always as slow axis
%x
xCol = find(not(cellfun('isempty',regexp(raw.colheaders, '
    X_Axis'))));

%y
yCol = find(not(cellfun('isempty',regexp(raw.colheaders, '
    Y_Axis'))));

%find fast axis and scan size
%{
To find the fast axis and resolution (scan size), we use
    the Fast Fourier
Transform, whose x axis (frequencies) is given by the total
    number of
points divided by the period plus 1 (1 + points/res in this
    case).
The fast axis has the shorter period of oscillation, which
    means it should
be the axis whose FFT has a maximum at a higher index. The
    frequency is
actually doubled due to trace and retrace.
```

```
%}
xVals = raw.data(:,xCol); yVals = raw.data(:,yCol);
[cx, ix] = max(abs(fft(xVals-mean(xVals))));
[cy, iy] = max(abs(fft(yVals-mean(yVals))));
ifast = max(ix , iy);
fastres = points/(2*(ifast-1));
slowres = points/(2*fastres);
%fastres = 128;
%slowres = 128;

x = reshape(raw.data(:,xCol), fastres, slowres*2); %put
    data in matrix form
S.xt = x(:,1:2:end); %trace signal in odd rows
S.xrt = fliplr(x(:, 2:2:end)); %retrace signal in even rows

y = reshape(raw.data(:,yCol), fastres, slowres*2); %put
    data in matrix form
S.yt = y(:,1:2:end); %trace signal in odd rows
S.yrt = fliplr(y(:, 2:2:end)); %retrace signal in even rows

%this can probably be made more efficient
if (ix > iy)
    S.fastvec = linspace(min(mean(S.xt,2)), max(mean(S.xt
        ,2)), fastres);
    S.slowvec = linspace(min(mean(S.yt,1)), max(mean(S.yt
        ,1)), slowres);
else
    S.fastvec = linspace(min(mean(S.yt,2)), max(mean(S.yt
        ,2)), fastres);
    S.slowvec = linspace(min(mean(S.xt,1)), max(mean(S.xt
        ,1)), slowres);
```

```
end

%height
%find the right column:
heightCol = find(not(cellfun('isempty',regexp(raw.
    colheaders, 'Height'))));
height = reshape(raw.data(:,heightCol), fastres, slowres*2)
    ; %put data in matrix form
S.ht = height(:,1:2:end)'; %trace signal in odd rows
S.hrt = fliplr(height(:, 2:2:end))'; %retrace signal in
    even rows

%optical amplitude
amplCol = find(not(cellfun('isempty',regexp(raw.colheaders,
     'NSOM'))));
ampl = reshape(raw.data(:,amplCol), fastres, slowres*2); %
    put data in matrix form
S.at = ampl(:,1:2:end)'; %trace signal in odd rows
S.art = fliplr(ampl(:, 2:2:end))'; %retrace signal in even
    rows

%optical phase
phaseCol = find(not(cellfun('isempty',regexp(raw.colheaders
    , 'Optical Phase'))));
phase = pi/9*reshape(raw.data(:,phaseCol), fastres, slowres
    *2); %put data in matrix form, and rescale to [-pi,pi]
S.pht = phase(:,1:2:end)'; %trace signal in odd rows
S.phrt = fliplr(phase(:, 2:2:end))'; %retrace signal in
    even rows
```

```
% xmin = mean(S.xt(:,1));
% xmax = mean(S.xt(:,xres));
% S.xint = (xmax - xmin) / (xres-1);
% S.xvec = [xmin:S.xint:xmax];
%
% ymin = mean(S.yt(1, :));
% ymax = mean(S.yt(yres, :));
% S.yint = (ymax - ymin) / (yres-1);
% S.yvec = [ymin:S.yint:ymax];
%
% S.xres = xres;
% S.yres = yres;

end

function f_fixed = fixNSOMFile (filename)
    if nargin < 1
        f = fullget; %pick a file of NSOM data to import
    else
        f = filename; %use the file given in the function
            argument
    end
    [pathstr, name, ext, versn] = fileparts(f);
    data = fileread(f);
    data_fixed = regexprep(data, '\t\r', '\r');
    name_fixed = [name '_FIXED'];
    f_fixed = fullfile(pathstr,[name_fixed ext versn]);
    fid = fopen(f_fixed, 'w+');
    fprintf(fid, '%s', data_fixed);
    fclose(fid);
end
```

```
function fileref = fullget()
[file path] = uigetfile;
fileref = fullfile(path, file);

function surfs = plotNSOMData(S, plotnew)
%plot height, amplitude, and phase from a given NSOM data
    structure S
xvec = S.fastvec;
yvec = S.slowvec;
hold off

if nargin<2
     plotnew = false;
end

%height (minus best-fit plane to eliminate tilt)
param = [S.xt(:) S.yt(:) ones(numel(S.at),1)] \ S.ht(:);
ht = (S.ht - (param(1)*S.xt + param(2)*S.yt + param(3)));
newfig(plotnew,1)
h = NSOMPlot(xvec, yvec,ht);
title('Height (nm)')

%optical amplitude
newfig(plotnew,2)
a = NSOMPlot(xvec, yvec, S.at);
title('Amplitude (V)')

%optical phase
newfig(plotnew,3)
ph = NSOMPlot(xvec, yvec, S.pht);
title('Phase')
```

```
%sine of optical phase
newfig(plotnew,4)
ph = NSOMPlot(xvec, yvec, S.at .* sin(S.pht));
title('A sin \phi (V)')

end

function newfig (plotnew, n)
if plotnew == true
    figure
else
    figure(n)
end
end

function hp = NSOMPlot (x, y, z)
%plot a set of NSOM data z along the x and y axes
colormap hot
axis equal
hp = pcolor(x, y, z);
% set(hp, 'ButtonDownFcn', 'bdf')
axis image
xlabel('x (\mum)', 'FontSize', 10)
ylabel('y (\mum)', 'FontSize', 10)
shading interp
colorbar
set(hp, 'linestyle', 'none')
set(gca,'FontSize',10)

function plotNSOMFFT (M)
[FFTdata, k] = NSOMFFT(M);
figure(10);
```

```
pcolor(abs(FFTdata).^2)
n_eff = k*1.55; %calculate effective index, assuming 1550

figure(5);
pcolor (n_eff, M.slowvec, abs(FFTdata).^2);
shading interp; colormap hot; colorbar;
xlabel('n_{eff}'); ylabel('y_(\mum)');
title('Spatial_Distribution_of_Modes');

figure(6);
% a = n_eff;
% b = mean(abs(FFTdata).^2,2);
% disp(a*b);


plot(n_eff, mean(abs(FFTdata).^2,1));
xlabel('n_{eff}'); ylabel('Power_(a.u.)');
title('Mode_Spectrum');


figure(7)
pcolor(M.slowvec,    n_eff, (angle(FFTdata)));
shading interp; colormap hot; colorbar;
ylabel('n_{eff}'); xlabel('y_(\mum)');

ang = angle(FFTdata);
power = abs(FFTdata).^2;

figure(8)
plot(n_eff,ang(:,50));
end
```

```
function [fieldFFT, freq] = NSOMFFT (M)
N = length(M.fastvec);
res = max(M.fastvec) - min(M.fastvec);


% field = M.at.*exp(i*M.pht) - mean(mean(M.at.*exp(i*M.pht)
    ));%.*meshgrid(linspace(exp(i*0),exp(i*-pi/2),128));
field = M.at.*exp(-i*M.pht) ;%.*meshgrid(linspace(exp(i*0),
    exp(i*-pi/2),128));
field = field - mean(field,2)*ones(1,size(M.at,2));
win = repmat(hamming(128)',128,1);
field = field.*win;
fieldFFT = fftshift(fft(field,[],2),2) / sqrt(N);


if mod(N,2)==0
    k=-N/2:N/2-1; % N even
else
    k=-(N-1)/2:(N-1)/2; % N odd
end


freq=k/res;  %the frequency axis
end

function plotNSOMFFTPartial (M, fastcoords,slowcoords)
[FFTdata, k] = NSOMFFTPartial(M,fastcoords,slowcoords);

n_eff = k*1.55; %calculate effective index, assuming 1550
length(n_eff)
length(FFTdata)
```

```
figure(5);
pcolor(n_eff, M.slowvec(slowcoords), abs(FFTdata).^2/max(
    max(abs(FFTdata).^2)));
shading interp; colormap hot; colorbar;
xlabel('n_{eff}'); ylabel('y (\mum)');
title('Spatial Distribution of Modes (a.u.)');

figure(6);
% hold on
plot(n_eff, mean(abs(FFTdata).^2,1)/max(mean(abs(FFTdata)
    .^2,1)));
xlabel('n_{eff}'); ylabel('Power (a.u.)');
title('Mode Spectrum');
% hold off

figure(7)
pcolor( n_eff, M.slowvec(slowcoords), (angle(FFTdata)));
shading interp; colormap hot; colorbar;
ylabel('n_{eff}'); xlabel('y (\mum)');

ang = angle(FFTdata);
power = abs(FFTdata).^2;

end

function [fieldFFT, freq] = NSOMFFTPartial (M, fastcoords,
    slowcoords)
% N = length(M.fastvec);
% res = max(M.fastvec) - min(M.fastvec);
fastvec = M.fastvec(fastcoords);

N = length(fastcoords);
```

```
res = max(fastvec) - min(fastvec);

% field = M.at.*exp(i*M.pht) - mean(mean(M.at.*exp(i*M.pht)
    ));%.*meshgrid(linspace(exp(i*0),exp(i*-pi/2),128));
field = M.at(slowcoords,fastcoords).*exp(-i*M.pht(
    slowcoords,fastcoords)) ;%.*meshgrid(linspace(exp(i*0),
    exp(i*-pi/2),128));
field = field - mean(field,2)*ones(1,size(fastvec,2));

fieldFFT = fftshift(fft(field,[],2),2) / sqrt(N);


if mod(N,2)==0
    k=-N/2:N/2-1; % N even
else
    k=-(N-1)/2:(N-1)/2; % N odd
end


freq=k/res;  %the frequency axis
end
```

Bibliography

[1] Liang Feng, Maurice Ayache, Jingqing Huang, Ye-Long Xu, Ming-Hui Lu, Yan-Feng Chen, Yeshaiahu Fainman, and Axel Scherer. Nonreciprocal light propagation in a silicon photonic circuit. *Science (New York, N.Y.)*, 333(6043):729–33, August 2011.

[2] Maurice Ayache, Maziar P. Nezhad, Steve Zamek, Maxim Abashin, and Yeshaiahu Fainman. Near-field measurement of amplitude and phase in silicon waveguides with liquid cladding. *Optics Letters*, 36(10):1869, May 2011.

[3] Steve Zamek, Liang Feng, Mercedeh Khajavikhan, Dawn T H Tan, Maurice Ayache, and Yeshaiahu Fainman. Micro-resonator with metallic mirrors coupled to a bus waveguide. *Optics Express*, 19(3):623–627, 2011.

[4] Steve Zamek, Dawn T H Tan, Mercedeh Khajavikhan, Maurice Ayache, Maziar P Nezhad, and Yeshaiahu Fainman. Compact chip-scale filter based on curved waveguide Bragg gratings. *Optics letters*, 35(20):3477–9, October 2010.

[5] S. Singh. *Fundamentals of Optical Engineering*. Discovery Press, 2009.

[6] Bahaa Saleh and Malvin Carl Teich. *Fundamentals of Photonics*. John Wiley & Sons, New York, 1991.

[7] Ernst Ruska. The Development Of The Electron Microscope And Of Electron Microscopy, 1986.

[8] S.M. Mansfield and G.S. Kino. Solid immersion microscope. *Applied physics letters*, 4085(October):2615–2616, 1990.

[9] Stefan Hell and Ernst H. K. Stelzer. Properties of a 4Pi confocal fluorescence microscope. *Journal of the Optical Society of America A*, 9(12):2159, December 1992.

[10] R Juskaitis, T Wilson, M A Neil, and M Kozubek. Efficient real-time confocal microscopy with white light sources. *Nature*, 383(6603):804–806, 1996.

[11] S W Hell and J Wichmann. Breaking the diffraction resolution limit by stimulated emission: stimulated-emission-depletion fluorescence microscopy. *Optics letters*, 19(11):780–2, June 1994.

[12] M Minsky. Microscopy Apparatus, 1961.

[13] C Cremer and T Cremer. Considerations on a laser-scanning-microscope with high resolution and depth of field. *Microscopica acta*, 81(1):31–44, September 1978.

[14] Lukas Novotny. The history of near-field optics. *Progress in optics*, 184:137–183, 2007.

[15] E H Synge. A suggested method for extending microscopic resolution into the ultra-microscopic region. *Philosophical Magazine Series 7*, 6(35):356–362, 1928.

[16] John Aloysius OKeefe. Resolving Power of Visible Light. *Journal of the Optical Society of America*, 46(5):359, May 1956.

[17] G. Ash, E.A.Nichols. Super-resolution aperture scanning microscope. *Nature*, 237:510–512, 1972.

[18] G Binnig, H Rohrer, Ch Gerber, and E Weibel. Surface Studies by Scanning Tunneling Microscopy. *Physical Review Letters*, 49(1):57–61, 1982.

[19] G Binnig and CF Quate. Atomic force microscope. *Physical review letters*, 56(9):930–933, 1986.

[20] A Lewis, M Isaacson, A Harootunian, and A Muray. Development of a 500 Åspatial resolution light microscope: I. light is efficiently transmitted through $\lambda/16$ diameter apertures. *Ultramicroscopy*, 13(3):227–231, 1984.

[21] E Betzig, A Lewis, A Harootunian, M Isaacson, and E Kratschmer. Near Field Scanning Optical Microscopy (NSOM): Development and Biophysical Applications. *Biophysical Journal*, 49(1):269–279, January 1986.

[22] D W Pohl, W Denk, and M Lanz. Optical stethoscopy: Image recording with resolution $\lambda/20$. *Applied Physics Letters*, 44(January):651–653, 1984.

[23] T Enderle, T Ha, D S Chemla, and S Weiss. Near-field fluorescence microscopy of cells. *Ultramicroscopy*, 71(1-4):303–9, March 1998.

[24] F de Lange, a Cambi, R Huijbens, B de Bakker, W Rensen, M Garcia-Parajo, N van Hulst, and C G Figdor. Cell biology beyond the diffraction limit: near-field scanning optical microscopy. *Journal of cell science*, 114(Pt 23):4153–60, December 2001.

[25] Shuqing Sun and Graham J Leggett. Matching the Resolution of Electron Beam Lithography by Scanning Near-Field Photolithography. *Nano Letters*, 4(8):1381–1384, 2004.

[26] Joseph W Goodman. *Introduction to Fourier Optics*, volume 45 of *McGraw-Hill physical and quantum electronics series*. McGraw-Hill, 2005.

[27] F Zenhausern, MP Oboyle, and HK Wickramsinghe. Apertureless nearfield optical microscope. *Applied physics*, 65(September):1623–1625, 1994.

[28] E Betzig, J K Trautman, T D Harris, J S Weiner, and R L Kostelak. Breaking the diffraction barrier: optical microscopy on a nanometric scale. *Science*, 251(5000):1468–70, 1991.

[29] G A Valaskovic, M Holton, and G H Morrison. Parameter control, characterization, and optimization in the fabrication of optical fiber near-field probes. *Applied optics*, 34(7):1215–1228, 1995.

[30] P Lambelet, a Sayah, M Pfeffer, C Philipona, and F Marquis-Weible. Chemically etched fiber tips for near-field optical microscopy: a process for smoother tips. *Applied optics*, 37(31):7289–92, November 1998.

[31] H. Bethe. Theory of Diffraction by Small Holes. *Physical Review*, 66(7-8):163–182, October 1944.

[32] C.J. Bouwkamp. Diffraction theory. *Reports on progress in physics*, 17:35–100, 1954.

[33] K Karrai and RD Grober. Piezoelectric tip-sample distance control for near field optical microscopes. *Applied physics letters*, 66(14):1842–1844, 1995.

[34] William Shockley. Circuit element utilizing semiconductive material, 1951.

[35] JS Kilby. Miniaturized electronic circuits. *US Patent 3,138,743*, 1964.

[36] GE Moore. Cramming more components onto integrated circuits. *Proceedings of the IEEE*, 38(8), 1965.

[37] KC Kao. Dielectric-fibre surface waveguides for optical frequencies. *IEE Proceedings*, 133(3):191–198, 1965.

[38] Lorenzo Pavesi and David J Lockwood, editors. *Silicon Photonics*. Springer-Verlag, Berlin, 2004.

[39] RA Soref. Single-crystal silicon: a new material for 1.3 and 1.6 μm integrated-optical components. *Electronics Letters*, 21(21):693–694, 1985.

[40] Yurii A Vlasov and Sharee J Mcnab. Losses in single-mode silicon-on-insulator strip waveguides and bends. *Optics Express*, 12(8):1622–1631, 2004.

[41] Maxim Abashin, Uriel Levy, Kazuhiro Ikeda, and Yeshaiahu Fainman. Effects produced by metal-coated near-field probes on the performance of silicon waveguides and resonators. *Optics letters*, 32(17):2602–4, September 2007.

[42] Ahn Goo Choo, Howard E. Jackson, Udo Thiel, Gregory N. De Brabander, and Joseph T. Boyd. Near field measurements of optical channel waveguides and directional couplers. *Applied Physics Letters*, 65(8):947, 1994.

[43] Yasunori Toda and Motoichi Ohtsu. High spatial resolution diagnostics of optical waveguides using a photon-scanning tunneling microscope. *IEEE Photonics Technology Letters*, 7(1):84–86, January 1995.

[44] S Bourzeix, JM Moison, F Mignard, and F Barthe. Near-field optical imaging of light propagation in semiconductor waveguide structures. *Applied physics letters*, 73(8):1035–1037, 1998.

[45] A L Campillo, C K Madsen, and J W P Hsu. Near-field scanning optical microscopy imaging of multimode interference. *Optics letters*, 28(13):1111–3, July 2003.

[46] G. H. Vander Rhodes, B. B. Goldberg, M. S. Unlu, S. T. Chu, W. Pan, T. Kaneko, Y. Kokobun, and B. E. Little. Measurement of internal spatial modes and local propagation properties in optical waveguides. *Applied Physics Letters*, 75(16):2368, 1999.

[47] Din Ping Tsai, Howard E. Jackson, R. C. Reddick, S. H. Sharp, and R. J. Warmack. Photon scanning tunneling microscope study of optical waveguides. *Applied Physics Letters*, 56(16):1515, 1990.

[48] Sergey Bozhevolnyi, Valentyn Volkov, Thomas Sø ndergaard, Alexandra Boltasseva, Peter Borel, and Martin Kristensen. Near-field imaging of light propagation in photonic crystal waveguides: Explicit role of Bloch harmonics. *Physical Review B*, 66(23):1–9, December 2002.

[49] Maxim Abashin, Pierpasquale Tortora, Iwan Märki, Uriel Levy, Wataru Nakagawa, Luciana Vaccaro, Hans Herzig, and Yeshaiahu Fainman. Near-field characterization of propagating optical modes in photonic crystal waveguides. *Optics express*, 14(4):1643–57, February 2006.

[50] Sergey I Bozhevolnyi, Valentyn S Volkov, Eloïse Devaux, Jean-Yves Laluet, and Thomas W Ebbesen. Channel plasmon subwavelength waveguide components including interferometers and ring resonators. *Nature*, 440(7083):508–11, March 2006.

[51] R. Dallapiccola, C. Dubois, a. Gopinath, F. Stellacci, and L. Dal Negro. Near-field excitation and near-field detection of propagating surface plasmon polaritons on Au waveguide structures. *Applied Physics Letters*, 94(24):243118, 2009.

[52] PL Phillips, JC Knight, and JM Pottage. Direct measurement of optical phase in the near field. *Applied Physics Letters*, 76(5):541–543, 2000.

[53] M L M Balistreri, Jp Korterik, L Kuipers, and van Hulst NF. Local observations of phase singularities in optical fields in waveguide structures. *Physical review letters*, 85(2):294–7, July 2000.

[54] M.L.M. Balistreri, J.P. Korterik, L. Kiupers, and N.F. van Hulst. Phase mapping of optical fields in integrated optical waveguide structures. *Journal of Lightwave Technology*, 19(8):1169–1176, 2001.

[55] A Nesci, R Dändliker, and H P Herzig. Quantitative amplitude and phase measurement by use of a heterodyne scanning near-field optical microscope. *Optics letters*, 26(4):208–10, February 2001.

[56] M L Balistreri, H. Gersen, J P Korterik, L Kuipers, and N F van Hulst. Tracking femtosecond laser pulses in space and time. *Science (New York, N.Y.)*, 294(5544):1080–2, November 2001.

[57] Maxim Abashin, Kazuhiro Ikeda, Robert Saperstein, and Yeshaiahu Fainman. Heterodyne near-field scanning optical microscopy with spectrally broad sources. *Optics letters*, 34(9):1327–9, May 2009.

[58] M. Burresi, R. Engelen, a. Opheij, D. van Oosten, D. Mori, T. Baba, and L. Kuipers. Observation of Polarization Singularities at the Nanoscale. *Physical Review Letters*, 102(3):1–4, January 2009.

[59] M Burresi, D van Oosten, T Kampfrath, H Schoenmaker, R Heideman, a Leinse, and L Kuipers. Probing the magnetic field of light at optical frequencies. *Science (New York, N.Y.)*, 326(5952):550–3, October 2009.

[60] Ilan Stefanon, Sylvain Blaize, Aurélien Bruyant, Sébastien Aubert, Gilles Lerondel, Renaud Bachelot, and Pascal Royer. Heterodyne detection of guided waves using a scattering-type Scanning Near-Field Optical Microscope. *Optics express*, 13(14):5553–64, July 2005.

[61] A Nesci and Y Fainman. Complex amplitude of an ultrashort pulse with femtosecond resolution in a waveguide using a coherent NSOM at 1550 nm. *Proceedings of SPIE*, 5181:62–69, 2003.

[62] Antonello Nesci. *Measuring amplitude and phase in optical fields with sub-wavelength features*. PhD thesis, 2001.

[63] John David Jackson. *Classical Electrodynamics*. Wiley, New Jersey, USA, 4 edition, 1998.

[64] Zheng Wang, Yidong Chong, J D Joannopoulos, and Marin Soljacić. Observation of unidirectional backscattering-immune topological electromagnetic states. *Nature*, 461(7265):772–5, October 2009.

[65] Katia Gallo, Gaetano Assanto, Krishnan R. Parameswaran, and Martin M. Fejer. All-optical diode in a periodically poled lithium niobate waveguide. *Applied Physics Letters*, 79(3):314, 2001.

[66] Zongfu Yu and Shanhui Fan. Complete optical isolation created by indirect interband photonic transitions. *Nature Photonics*, 3(2):91–94, 2009.

[67] Di Liang and John E. Bowers. Recent progress in lasers on silicon. *Nature Photonics*, 4(8):511–517, July 2010.

[68] Roger Chen, Thai-Truong D. Tran, Kar Wei Ng, Wai Son Ko, Linus C. Chuang, Forrest G. Sedgwick, and Connie Chang-Hasnain. Nanolasers grown on silicon. *Nature Photonics*, 5(3):170–175, February 2011.

[69] O. Painter. Two-Dimensional Photonic Band-Gap Defect Mode Laser. *Science*, 284(5421):1819–1821, June 1999.

[70] MP Nezhad, Aleksandar Simic, Olesya Bondarenko, and Boris Slutsky. Room-temperature subwavelength metallo-dielectric lasers. *Nature Photonics*, 4(April):395–399, 2010.

[71] Jin Sun, John C. Schotland, Rainer Hillenbrand, and P. Scott Carney. Nanoscale optical tomography using volume-scanning near-field microscopy. *Applied Physics Letters*, 95(12):121108, 2009.

[72] Michael Hochberg, Tom Baehr-Jones, Guangxi Wang, Michael Shearn, Katherine Harvard, Jingdong Luo, Baoquan Chen, Zhengwei Shi, Rhys Lawson, Phil Sullivan, Alex K Y Jen, Larry Dalton, and Axel Scherer. Terahertz all-optical modulation in a silicon-polymer hybrid system. *Nature materials*, 5(9):703–9, September 2006.

[73] Mark a Foster, Reza Salem, David F Geraghty, Amy C Turner-Foster, Michal Lipson, and Alexander L Gaeta. Silicon-chip-based ultrafast optical oscilloscope. *Nature*, 456(7218):81–4, November 2008.

[74] Jurgen Michel, Jifeng Liu, and Lionel C. Kimerling. High-performance Ge-on-Si photodetectors. *Nature Photonics*, 4(8):527–534, July 2010.

[75] Carl M. Bender and Stefan Boettcher. Real Spectra in Non-Hermitian Hamiltonians Having PT Symmetry. *Physical Review Letters*, 80(24):5243–5246, June 1998.

[76] Carl M Bender. Making sense of non-Hermitian Hamiltonians. *Reports on Progress in Physics*, 70(6):947–1018, June 2007.

[77] K. G. Makris, R. El-Ganainy, and D. N. Christodoulides. Beam Dynamics in PT Symmetric Optical Lattices. *Physical Review Letters*, 100(10):1–4, March 2008.

[78] R El-Ganainy, K G Makris, D N Christodoulides, and Ziad H Musslimani. Theory of coupled optical PT-symmetric structures. *Optics letters*, 32(17):2632–4, September 2007.

[79] Z. H. Musslimani. Optical Solitons in PT Periodic Potentials. *Physical Review Letters*, 100(3):1–4, January 2008.

[80] A. Guo, G. J. Salamo, M. Volatier-Ravat, V. Aimez, G. a. Siviloglou, and D. N. Christodoulides. Observation of PT-Symmetry Breaking in Complex Optical Potentials. *Physical Review Letters*, 103(9):093902(1–4), August 2009.

[81] Christian E. Rüter, Konstantinos G. Makris, Ramy El-Ganainy, Demetrios N. Christodoulides, Mordechai Segev, and Detlef Kip. Observation of paritytime symmetry in optics. *Nature Physics*, 6(3):192–195, January 2010.

[82] Hiroshi Muramatsu, Norio Chiba, Katsunori Homma, Kunio Nakajima, Tatsuaki Ataka, Satoko Ohta, Akihiro Kusumi, and Masamichi Fujihira. Near-field optical microscopy in liquids. *Applied Physics Letters*, 66(24):3245, 1995.

[83] CE Talley, GA Cooksey, and RC Dunn. High resolution fluorescence imaging with cantilevered near-field fiber optic probes. *Applied Physics Letters*, 69(December):3809–3811, 1996.

[84] M Koopman, a Cambi, B I de Bakker, B Joosten, C G Figdor, N F van Hulst, and M F Garcia-Parajo. Near-field scanning optical microscopy in liquid for high resolution single molecule detection on dendritic cells. *FEBS letters*, 573(1-3):6–10, August 2004.

[85] Wonsoo Ji, Daechan Kim, Hyun Jun Kim, Se-geun Park, El-hang Lee, and Seung Gol Lee. NSOM-based characterization method applicable to optical channel waveguide with a solid-state cladding. *IEEE Photonics Technology Letters*, 17(4):846–848, April 2005.

[86] G M Hale and M R Querry. Optical Constants of Water in the 200-nm to 200-micrometer Wavelength Region. *Applied optics*, 12(3):555–63, March 1973.

[87] Vilson R. Almeida, Roberto R. Panepucci, and Michal Lipson. Nanotaper for compact mode conversion. *Optics Letters*, 28(15):1302–4, August 2003.

[88] M L M Balistreri, J P Korterik, L Kuipers, and N F Van Hulst. Phase mapping of optical fields in integrated optical waveguide structures. *Journal of Lightwave Technology*, 19(8):1169–1176, 2001.

[89] J. M. Blackledge. *Digital Image Processing: Mathematical and Computational Methods*. Horwood Publishing, Chichester, UK, 2005.

[90] Richard Hamming. *Digital Filters*. Prentice-Hall, Englewood Cliffs, N.J., 1977.

[91] J.J. Burke, G.I. Stegeman, and T. Tamir. Surface-polariton-like waves guided by thin, lossy metal films. *Physical Review B*, 33(8):5186–5201, 1986.

[92] Dror Sarid. Long-range surface-plasma waves on very thin metal films. *Physical Review Letters*, 47(26):1927–1930, 1981.

[93] Pierre Berini. Plasmon polariton modes guided by a metal film of finite width. *Optics Letters*, 24(15):1011–1013, 1999.

[94] Pierre Berini. Long-range surface plasmon-polariton waveguides in silica. *Journal of Applied Physics*, 102(5):053105, 2007.

[95] Ildar Salakhutdinov, Jagdish S. Thakur, and Kristjan Leosson. Characterization of long-range surface plasmon-polariton in stripe waveguides using scanning near-field optical microscopy. *Journal of Applied Physics*, 102(12):123110, 2007.

[96] E D Palik. *Handbook of Optical Constants of Solids*, volume 1 of *Academic Press handbook series*. Academic Press, 1985.

[97] VN Konopsky, KE Kouyanov, and NN Novikova. Investigations of the interference of surface plasmons on rough silver surface by scanning plasmon near-field microscope. *Ultramicroscopy*, 88:127–138, 2001.

[98] H L Offerhaus, B van den Bergen, M Escalante, F B Segerink, J P Korterik, and N F van Hulst. Creating focused plasmons by noncollinear phasematching on functional gratings. *Nano letters*, 5(11):2144–8, November 2005.